Spring 5-2017

Bioinspired Design of Wetting and Anti-Wetting Surfaces via Thiol-ene Photopolymerization

Li Xiong
University of Southern Mississippi

BIOINSPIRED DESIGN OF WETTING AND ANTI-WETTING SURFACES

VIA THIOL-ENE PHOTOPOLYMERIZATION

by

Li Xiong

A Dissertation
Submitted to the Graduate School
and the School of Polymers and High Performance Materials
at The University of Southern Mississippi
in Partial Fulfillment of the Requirements
for the Degree of Doctor of Philosophy

Approved:

_____
Dr. Derek L. Patton, Committee Chair
Associate Professor, Polymers and High Performance Materials

_____
Dr. Sergei I. Nazarenko, Committee Member
Professor, Polymers and High Performance Materials

_____
Dr. Sarah E. Morgan, Committee Member
Professor, Polymers and High Performance Materials

_____
Dr. Jeffrey S. Wiggins, Committee Member
Associate Professor, Polymers and High Performance Materials

_____
Dr. Joseph R. Lott, Committee Member
Assistant Professor, Polymers and High Performance Materials

_____
Dr. Jeffrey S. Wiggins
Director, School of Polymers and High Performance Materials

_____
Dr. Karen S. Coats
Dean of the Graduate School

May 2017

Published by the Graduate School

ABSTRACT

BIOINSPIRED DESIGN OF WETTING AND ANTI-WETTING SURFACES VIA THIOL-ENE PHOTOPHOLYMERIZATION

by Li Xiong

May 2017

Surface wettability is known to have a profound influence in both academic study and industrial application of materials. Superhydrophobic surfaces, with a static contact angle higher than 150° and a contact angle hysteresis lower than 10°, have received continued attention for their broad applications, such as self-cleaning, antifogging and frosting, and drag reduction. The continuous development of materials and approaches that used to create superhydrophobic surfaces has led to further exploration of coatings with other desirable properties such as superamphiphobicity, mechanical robustness and thermal stability.

In this work, coatings with super wetting and super anti-wetting properties were designed and fabricated by tailoring the chemical composition and the morphology of the surface in an effort to expand the application and to improve the mechanical property of the coatings.

In the first study, a superamphiphobic coating was prepared by spray deposition and followed up UV-polymerization of a hybrid organic-inorganic thiol-ene precursor. The combination of dual-scale roughness and low surface energy materials led to surfaces with strong water/ oil repellency and self-cleaning properties.

In the second study, a superhydrophilic and superoleophobic membrane for oil/water separation applications was developed. The textured membrane morphology

enhanced the hydrophilic and oleophobic properties of the surface. The efficiency of the superhydrophilic/superoleophobic membrane on oil/water separation was demonstrated by emulsion and dye contained emulsion separation studies.

In the third study, a superhydrophobic surface was prepared with porogen leaching approach in an effort to reduce the loading level of NPs. The microphase separation and porogen leaching process resulted in microscale roughness. NPs migration from bulk to interphase led to the formation of nanoscale roughness. The combination of micro- and nano-scale feature provides the surface with superhydrophobicity with 50 wt.% reduced NPs loading level.

ACKNOWLEDGMENTS

I would like to express my sincere appreciation to my graduate research advisor, Dr. Derek L. Patton, for his constant guidance and support during the course of my graduate study at the University of Southern Mississippi.

I would also like to thank my committee members, Dr. Sergei I. Nazarenko, Dr. Sarah E. Morgan, Dr. Jeffrey S. Wiggins, and Dr. Joseph R. Lott for their time and constructive suggestions for this dissertation. I also wish to express appreciation to Dr. Jessica Douglas for all of her invaluable assistance with the SEM, and TEM throughout my research. I appreciate all the staff within the School of Polymers and High Performance Materials for their assistance.

I would also like to thank the past and present Patton Research Group members, Dr. Ryan Hensarling, Dr. Bradley Sparks, Dr. Austin Baraneck, Dr. Janannee Narayanan, Dr. Emily Hoff, Dr. Brian Donovan, Dr. Wei Guo, Yidan Guan (GA), Douglas Amato (GA), Dahlia Amato (GA), Cassandra Reese (GA), and Michelle Vekasy for their friendship and assistance in all aspects of scientific and professional development.

I would like to thank the National Science Foundation for funding some of my graduate research. Finally, I would like to acknowledge my parents, my husband and my daughter-to-be for their love and support throughout my life.

DEDICATION

To my parents Lianfang Xiong and Zhentao Liu, my truly loved husband Wei Guo and my dear daughter-to-be!

TABLE OF CONTENTS

indicates that less thiol is consumed in the step-growth process resulting in unreacted thiol monomers. To obtain polymer coatings with minimum monomer

LIST OF TABLES

LIST OF ILLUSTRATIONS

LIST OF SCHEMES

LIST OF ABBREVIATIONS

CA	Contact Angle
CAH	Contact Angle Hysteresis
CNT	Carbon Nanotube
CPS	Count per Second
CVD	Chemical Vapor Deposition
DCA	Dynamic Contact Angle
DI	Deionized
DLS	Dynamic Light Scattering
DMPA	2,2-Dimethoxy-2-phenylacetophenone
DRIE	Deep Reactive Ion Etching
EDS	Energy Dispersive Spectroscopy
EMI	2-Ethyl-4-methyl-imidazole
FE-SEM	Field-Emission Scanning Electron Microscopy
FTIR	Fourier Transform Infrared Spectroscopy
F_6*PETMP*	1H,1H-perfluoroheptyl pentaerythritol tetra(3-mercaptopropionate)
F_9*PETMP*	1H,1H-perfluoro-n-decyl pentaerythritol tetra(3-mercaptopropionate)
F-PETMP	Fluorinated pentaerythritol tetra(3-mercaptopropionate)
GDMP	Glycol dimercaptoacetate
HMPA	Hexahydro-4-methylphthalic anhydride

LIPS	Lubricating Infused Porous Surface
MW	Molecular Weight
NP	Nanoparticle
OCA	Oil Contact Angle
OSA	Oil Sliding Angle
PAM	Polyacrylamide
PDMS	Poly(dimethylsiloxane)
PECVD	Plasma Enhanced Chemical Vapor Deposition
PEG	Polyethylene glycol
PETMP	Pentaerythritol tetra(3-mercaptopropionate)
PMMA	Poly(methyl methacrylate)
PS	Poly(styrene)
PtBA	Poly(tert-butyl acrylate)
PTFE	Polytetrafluoroethylen
SCA	Static Contact Angle
SDS	Sodium Dodecyl Sulphate
SEM	Scanning Electron Microscopy
SFE	Surface Free Energy
TEM	Transmission Electron Microscopy
THF	Tetrahydrofuran
TMS	Trimethysilyl
TMTVSi	2,4,6,8-tetramethyl-2,4,6,8-tetravinylcyclotetrasiloxane

TTT	1,3,5-triallyl-1,3,5-triazine-2,4,6 (1H, 3H, 5H) trione
UV	Ultraviolet
UV/VIS	Ultraviolet-Visible Spectrophotometry
WCA	Water Contact Angle
WSA	Water Sliding Angle
XPS	X-ray Photoelectron Spectroscopy
^{1}H-NMR	Proton Nuclear Magnetic Resonance
3D	Three Dimentional

CHAPTER I - INTRODUCTION

1.1 Superhydrophobic Surfaces

Superhydrophobic surfaces exhibiting an apparent water contact angle of greater than 150° and low contact angle hysteresis[1] have attracted a tremendous amount of attention due to potential applications in self-cleaning coatings,[2-4] drag reduction,[5-7] corrosion resistance,[8-10] anti-icing[11-13] and high-performance textiles.[14, 15] It is well established that the superhydrophobic wetting state can be attributed to both chemical composition and geometric parameters (i.e. roughness) of the solid interface.[16] Specifically, the superhydrophobic wetting state is typically manifested on surfaces exhibiting a combination of low surface energy and an appropriately designed hierarchically structured surface comprised of dual-scale textures (typically nanometer scale features superimposed on underlying micrometer scale features).[17] In general, the dual-scale surface roughness serves to either increase or decrease the contact area of the solid-liquid interface resulting in a so-called apparent contact angle. Either the liquid completely conforms to the surface roughness to increase the solid-liquid contact area – an adhesive wetting behavior described as the Wenzel wetting state,[18] or the liquid bridges between surface roughness protrusions creating a composite solid-liquid-air interface – a wetting behavior denoted as the Cassie-Baxter wetting state. The composite interface associated with the Cassie-Baxter wetting state typically leads to high contact angles, low roll-off angles, and correspondingly low contact angle hysteresis.[2, 19, 20]

1.1.1 Chemical Composition and Surface Morphology.

Surface wetting refers to the interactions between a liquid and a solid at the liquid-solid interface formed by the physical contact between the two phases. At the

most fundamental level, the nature of these interactions occur on the atomic or molecular scale and represent a dynamic energy balance between intermolecular, electrostatic, polar, and gravitational contributions. As a result of these combined energy contributions, a liquid droplet will adopt a geometric configuration that minimizes the total energy of the solid-liquid interface. The relevant energy parameter for this situation, which encompasses all of the aforementioned energetic contributions to surface wetting, is the surface free energy (SFE), defined as the reversible work required to create a unit of new surface area. This parameter has units of (energy/area), or equivalently, (force/length), which are the conventional units for liquid surface tension. For a liquid, the SFE and surface tension are synonymous. In the case that the "new surface" created is interfacial surface area between the solid and liquid, the SFE is termed the solid-liquid interfacial energy. SFE determines the wetting property of the solid which described as contact angle θ (as shown in Scheme 1.1) between the solid and the liquid.

Contact angle (CA) measurements can be performed both statically and dynamically. Measuring the static contact angle (SCA) of a surface involves placing a droplet of water on the surface with no further manipulation. The resultant SCA is close to the equilibrium predicted by the Young's equation. As the name implies, dynamic contact angle (DCA) is the contact angle which occurs in the course of wetting (advancing contact angle) or dewetting (receding contact angle). The DCA are measured as the volume of droplet is being added (advancing CA), or being reduced (receding CA). The advancing CA is a measure of how energetically favorable it is for a surface to wet, whereas receding contact angles is a measure of how favorable for a surface to de-wet.

The difference between advancing and receding contact angle is referred to as contact angle hysteresis (CAH).

1.1.2 Wetting on Flat Surface.

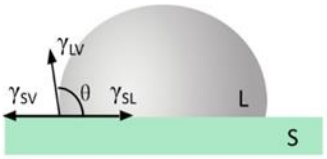

Scheme 1.1 Schematic of wetting on flat surface.

The relationship between SFE and CA, θ, of a smooth, flat and chemically homogeneous surface is determined by Young's equation,

$$\cos\theta = \frac{\gamma_{SV} - \gamma_{SL}}{\gamma_{LV}} \quad \text{Equation (1)}$$

where γ is the interfacial surface free energies between the solid-vapor (γ_{SV}), solid-liquid (γ_{SL}), or liquid-vapor (γ_{LV}) phases (Scheme 1.1). The Young's angle, θ, in the equation is referred to as the CA of a surface which is determined by the equilibrium of the surface energies of these three interfaces. The Young's angle can be seen as an indicator of SFE of a given flat solid surface. Most often, contact angles are measured using water as the liquid phase. By definition, surface materials with CAs > 90° in contact with water are referred to as hydrophobic (e.g. PTFE, PDMS), whereas materials with water CAs < 90° are referred to as hydrophilic (e.g. most plastics, metals). Large contact angle (hydrophobic) implies that γ_{SL} is large, whereas small contact angles (hydrophilic) imply γ_{SL} is small.

1.1.3 Roughness and Superhydrophobicity.

The Young's equation, which relates the intrinsic contact angle θ to SFE, is based on the assumption that the surface is ideally flat, smooth and chemically homogeneous. Surfaces in real world, however, are not ideal flat, smooth and homogeneous. Specifically, contact angles of surfaces with rough morphology cannot be fully explained by the Young's equation.

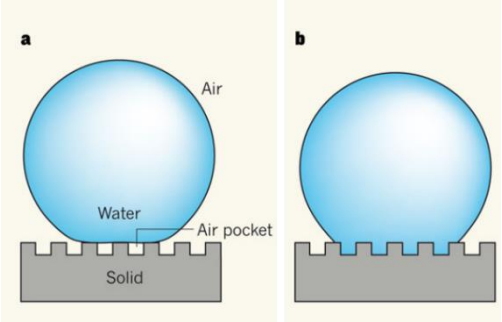

Scheme 1.2 Schematic of a sessile drop on an array of pillars in the (a) Cassie-Baxter model and (b)Wenzel model

To address the issue of rough surfaces, the Wenzel[18] model and Cassie-Baxter[21] model have been developed. The Wenzel model, which assumes that water will penetrate into the roughness features and make full contact with the rough surface, states the following:

$$\cos\theta_{rough} = r \cdot \cos\theta_{flat} \quad \text{Equation (2)}$$

where θ_{flat} is the Young's angle on a flat surface, r is a roughness factor or roughness coefficient, and θ_{rough} is the measured contact angle (i.e. apparent contact angle) on a rough surface (Wenzel angle). The roughness factor is the ratio between (i) the surface area a droplet contacts on the rough surface and (ii) the projected area of the contact area by the droplet. A roughness factor of 1 implies the surface is smooth, where a roughness

factor greater than 1 implies that the surface is rough. The Wenzel model states that both hydrophilicity ($\theta_{flat} < 90°$) and hydrophobicity ($\theta_{flat} > 90°$) are enhanced with increased roughness as the water droplet is now able to contact more of a material surface within the same droplet projected area. The model also predicts an increase in contact angle hysteresis; the increased roughness of the surface results in further droplet-material contact and pinning of the droplet during de-wetting process.

At very high roughness values (r = 1.7), the increase in contact angle hysteresis (CAH) predicted by the Wenzel model drops dramatically with hydrophobic surfaces. Hydrophobic surfaces with very high roughness values (r = 1.7), instead of exhibit large contact angle hysteresis (CAH) as predicted by the Wenzel model, show drastically decreased CAH values.

The CAH deviation from the Wenzel model is caused by air trapped within the grooves between liquid and the rough substrate which is contrary to the Wenzel model's assumption. The CAH deviation from the Wenzel model is because that the Wenzel model assumption that water will penetrate into surface grooves and achieve full contact of the rough surface no longer stands for hydrophobic surfaces with very roughness features. For hydrophobic rough surfaces, air or vapor will be trapped within the surface grooves in between solid substrate and the water droplet thus decreasing the actual contact area.

To describe this phenomenon, the Cassie-Baxter model extends the Wenzel model to describe the wetting of a surface where two phases (solid and vapor) are present under the applied droplet. A diagram of the difference between these two states of wetting is seen in Scheme 1.2a-b. The Cassie-Baxter model states the following:

$$\cos\theta' = f_1 \cos\theta_1 + f_2 \cos\theta_2 \quad \text{Equation (3)}$$

Where f_1 and f_2 are the surface fractions of phase 1 (liquid on solid) and phase 2 (liquid on vapor), θ_1 and θ_2 are the Young's contact angle for these two phases, and θ' is the measured contact angle on the material surface. The Cassie-Baxter model can be seen as a weighted average between the two phases, where f_1 and f_2 attribute a certain fraction of the surface area the droplet is contacting at the composite surface of solid and vapor. The relationship is simplified for a superhydrophobic surface when air (θ=180°) is the second phase under the applied droplet:

$$\cos\theta' = f\cos\theta - (1 - f) \quad \text{Equation (4)}$$

where the Cassie angle is now a function of the fraction of solid (*f*) at the droplet interface and Young's angle of the solid (Scheme 1.2a). Combined, the Wenzel model and Cassie-Baxter model provide a framework for understanding the complicated interplay between the three phase boundaries at a rough material surface. It is often unclear for a given surface whether the Wenzel or Cassie-Baxter state is favored, as well as when the transition between the two states occurs with modification to surface roughness and/or surface energy. Theoretical work aiming to identify appropriate boundary conditions between states, and remains an active area of research. However, when examining the Cassie-Baxter equation, it is clear that both surface chemistry and surface roughness are the primary factors at play when determining the behavior of water, and droplets thereof, on a material surface.

As mentioned earlier, the well-established definition of superhydrophobic surfaces describes those surfaces with apparent contact angles above 150°, where the 'apparent' designation refers to a measurement taken on a rough material surface. The

definition can be further refined to confine the designation of superhydrophobicity to surfaces which have contact angle hysteresis (CAH) less than10° and demonstrate small amounts of 'droplet pinning', as hysteresis is an important consideration for applications including self-cleaning and low-drag surfaces. While these designations are valuable benchmarks, they are also arbitrary as no special air layer stability is conferred at these values. Empirical studies by Tuteja et al.[22] and Quere et al.[17] are good examples where boundaries of the stable Cassie-Baxter state for a specific superhydrophobic system have been explored and identified and has ultimately better merit for designating superhydrophobicity. Empirical results and theoretical studies have shown that the air layer at a material surface can be metastable or stable with a dependence on the intrinsic material surface energy, fill fraction, aspect ratio/geometry, and reentrant curvature.[23-25]

1.1.4 Superhydrophobic Surfaces in Nature.

The development of superhydrophobic coating is inspired from an array of surfaces that possess anti-wetting, anti-icing and self-cleaning properties in nature.[26] A well-known example is lotus leaf which has a water contact angle of 165° and a roll-off angle of only 2°. The superhydrophobicity of lotus leaf is advantageous to photosynthesis and transpiration in aquatic environment in that it prevents water and dust from covering of the leaves.[27-29]

The correlation between water repellency and surface morphology is first reported by Barthlott and Neinhuis.[30] It is believed that the superhydrophobicity of lotus leaves is mainly due to two reasons, a layer of hydrophobic epicuticular wax crystalloids on the surface and microscopic roughness. Later on, Jiang research group reported the morphological study of lotus leaf using SEM and they observed evenly distributed

papillae of 5 to 9 μm on the surface and on top of every papillae are branch-like hairy nanostructures with average diameters of 124.3 ± 3.2 nm.[31] They firstly pointed out that the combination of this micro- and nano- scale hierarchical structures and low surface energy epicuticular wax yields the superhydrophobicity and self-cleaning property.

Another superhydrophobicity example in nature is the rice leaf which, different from the lotus leaf, exhibit anisotropic dewetting property. The papillae of the rice leaf are aligned in the direction parallels to the vein while randomly distributed in the perpendicular direction of the vein. As a result, water droplets tend to move freely along the vein direction but not along the perpendicular direction. The special morphology resulted smaller roll off angle (3~5°) along the vein direction as compared to the direction that is perpendicular to the vein (9~15°).[32] The similar anisotropic dewetting property is observed on butterfly wings where one-dimensional oriented periodic overlapping micro-squamas covered by lamella-stacking nano-stripes.[33]

Other than aquatic plants, gerridae, commonly known as water strider, is another example of superhydrophobicity in nature. Its capability of 'walking' on the surface of water is based on special microstructures on the legs which has a water contact angle of 167°.[34]

1.1.5 Artificial Fabrication of Superhydrophobic Coatings.

Inspired from nature biological surfaces, numerous physical and chemical approaches have been reported to design and fabricate hierarchically structured surfaces from low surface energy materials in pursuit of the desirable Cassie-Baxter wetting state including templating,[35-41] lithography,[42-45] , phase separation,[46-48] electrospinning,[49-51] chemical vapor deposition,[39, 52, 53] chemical etching,[54-57] sol-gel techniques,[3, 58-60] spray

deposition[61-64] and among many others. In general, these methods can be categorized as top-down which creates rough surface with intrinsic hydrophobic materials and bottom-up approaches which generate roughness surface first then coat the surface with low surface energy layer. Some aforementioned techniques require multiple processing steps, expensive building blocks and/or equipments, and exhibit limitations in terms of substrate size and materials.

1.1.5.1 Templating.

Templating is a simple approach to fabricate superhydrophobic surfaces with hierarchical roughness from low surface energy materials. It utilizes natural or artificial surfaces as the template and replicates the morphology using a base material. PDMS is a commonly used base material due to its durability, processability and intrinsically hydrophobicity. After cure the base material, the original template is removed and formed a negative template which can be used to make more replicas. Initially, rough surfaces from nature are used directly as templates.[41] Jiang et al. reported that rose petals exhibit a superhydrophobic state with high adhesion force and they further revealed that the 'rose petal effect' is caused by hierarchical micropapillae and nanofolds. Then they fabricated biomimic polymer films with well-defined nanoembossed structures by duplicating petal's surface. The obtained polymer surface indicates that the high adhesion superhydrophobic film is in Cassie impregnating wetting state.[35] Other than using nature materials as mold, templating method has been used with other techniques to fabricate surfaces with textured structure. Su et al.[36] fabricated a superhydrophobic surface with excellent abrasion resistance based on polyurethane elastomer via templating. In the first step, Su and coworkers created a metal mold with hierarchical

structure using chemical etching then replicated the morphology of the mold using polyurethane elastomer. Similarly, Xu et al.[38] used a simple and inexpensive lamination templating approach to fabricate abrasion resist superhydrophobic polymer surfaces. Templating is a straightforward technique for fabricating surfaces with hierarchical roughness but its application in terms of surface engineering over very large area is limited by the template size itself and the choice of base materials.

1.1.5.2 Lithography.

Lithography (photo-, E-beam, X-ray, and soft lithography) are a family of surface engineering techniques that allows the creation of complex and well-controlled surface architecture at micro and/or sub-micro scales. Lithography has been employed in both top-down (create roughness features on hydrophobic materials) and bottom-up (using low surface energy compound to modify textured surfaces) approaches. Bhushan and Jung[43] fabricated micropatterned silicon surfaces with pillars of two different diameters and heights with varying pitch values using photolithography. Lithography can be used in combination with other techniques to fabricate superhydrophobic surfaces. Bhushan and Jung[65] used vapor phase deposition technique to deposit a hydrophobic monolayer of 1,1,-2,2,-tetrahydroperfluorodecyltrichlorosilane on top of structured surfaces created by lithography to obtain the hydrophobicity with a contact angle up to 170°. Choi et al.[44] fabricated perfectly ordered microstructures with an inverse-trapezoidal cross section with two consecutive PDMS replication processes and a three-dimensional diffuser lithography technique on a large-size template of the transparent PDMS elastomer surface. They further modified the surface with spin coating of a fluoropolymer layer to improve the hydrophobicity and transparency. The obtained surface showed a

superhydrophobicity and oleophobicity with robustness toward water droplet impingement and transparency. The advantage of lithography as a surface engineering technique is that it generates surfaces with accuracy and complex geometric designs; however, the high cost, long processing time and small processing size prevent it from being transplanted to large scale applications.

1.1.5.3 Phase Separation.

Phase separation is a useful method for fabrication rough and porous polymer films. It's commonly used to prepare polymer monoliths with macro- and microphase separation.[66-69] Zhao et al.[47, 48] introduced a simple approach for preparing a superhydrophobic copolymer surface by casting the micellar solution of polystyrene-block- polydimethylsiloxane (PS-b-PDMS) in humid air. The rough surface structure derives from vapor-induced phase separation, and the low surface tension results from the surface migration of the PDMS block. Both rough surface morphology and low surface tension provides the surface with superhydrophobicity. Han et al.[46] presented the formation of suphydrophobic surface from a poly(tert-butyl acrylate-block-polydimethylsiloxane (PtBA-b-PDMS-b-PtBA) micelle solution by controlling the solvent power of a selective solvent. The advantage of phase separation is it can generate micro-sized roughness feature without requiring complex facility, however, it requires suitable procedure to allow the phase separation to occur which cannot meet all of the situations.

1.1.5.4 Electrospinning.

Electrospinning is a commonly used method to produce fiber. It is a process to apply electric force between the spin nozzle and the collect plate to generate fibers with

diameters in sub-micro scales from polymer solutions or polymer melts. The morphology of the surface is highly depend on the viscosity of the polymer solution or melts. Jiang et al.[49] reported the preparation of microsphere/nanofiber composite film of PS by electrospinning method that exhibit similar properties of lotus leaf and afforded superhydrophobicity (CA = 160.4°). The morphologies of prepared surface were controlled by tuning the concentration of the polystyrene solution from only nanofibers randomly oriented to predominantly microspheres by decreasing the viscosity. The porous microspheres contribute to the superhydrophobicity by increasing surface roughness, while nanofibers interweave to form a 3D network that reinforces the composite film. Electrospinning can also be combined with other technique to extend the application. Tuteja et al.[51] produced superoleophobic surface for chemical shielding using the electrospinning of cross-linked poly(dimethylsiloxane) with fluorodecyl polyhedral oligomeric silsequioxane. The fabricated surface possess hierarchical scales of re-entrant texture with low surface energy chemical composition which endows the surface with extreme repellency towards all liquids including concentrated organic and inorganic acid, base and solvents as well as polymer solutions. Electrospinning has the advantages of low cost and high production rate but its wide application is limited by the choice of polymer solutions/melts and the prepared films are lack of mechanical durability

1.1.5.5 Chemical Vapor Deposition (CVD).

Chemical vapor deposition (CVD) is a chemical process often used for surface modification that involves exposure of a selected substrate to a vapor environment during which the vapor molecules deposit onto the surface. CVD generate very thin layer film

and is commonly used as surface chemistry modification method with other technique to fabricate hierarchical structured surface. Lau et al.[52] deposited the inherent vertically aligned carbon nanotube forest using a plasma enhanced chemical vapor deposition (PECVD) technique to create a superhydrophobic coating. Deng et al.[39] created superamphiphobic surface by forming a film of low surface energy fluorinated silane film via CVD technique on top of a surface with hierarchical roughness. The obtained film exhibited superamphiphobicity with water and hexadecane droplets bouncing on the surface and mechanical and thermal durability. Further, they reported the work of fabrication superhydrophobic surface from porous silica capsules with transparent, thermally stable and mechanically robust property.[53] The roughness feature was created by layer-by-layer method with PS particles followed with CVD technique to improve the superhydrophobicity and mechanical stability. Compared with the film which particles stick to the surface by van der Waals interaction only, the film after CVD shows good result towards the double tap test due to the chemically binding. The CVD technique has the advantage of flexibility and low cost, but the method only changes the chemical component of the surface.

1.1.5.6 Chemical Etching.

Chemical Etching, using acid or base chemicals to corrupt the metal or inorganic material allowing the crystal growth or material removal, is another way to create rough structured surfaces. Kondrashov et al.[56] presented the generation of mechanically robust hierarchical superhydrophobic surfaces composed with two-tier roughness using mask-free dry etching processes. First, they utilizing a cryogenic deep reactive ion etching (DRIE) process run in the overpassivation regime obtained the silicon microcones.

Second, they used an alternating etching and passivation cycles ('BOSCH process') to generate silicon nanograss roughness feature. The superhydrophobic structures were achieved with covering a layer of a fluorinated film with the evidence of having the advancing contact angle ranged between 170° and 180°, and roll-off angles of 10 μL drops. Peng et al.[57] generated a chemically stable and mechanically durable superamphiphobic aluminum surface by combine the simple chemical etching and boiling water immersion processes with microplateaus and nanoplatelets dual structures. The following fluorination treatment provides the aluminum surface with superamphiphobicity. Wong and coauthor[55] presented a work on fabrication of hierarchically structured silicon superhydrophobic surfaces formed by KOH etching and metal-assisted etching with superior abrasion resistance. The advantages of chemical etching are flexible and cheap, but the caused chemical contamination and less control on the morphology limited the application.

1.1.5.7 Sol-Gel.

Sol-gel is a process that is utilized for making metal oxides, especially the oxides of silicon and titanium. The process involves conversion of monomers into a colloidal solution (sol) that acts as the precursor for the generation of integrated network polymers or discrete particles.[60] Materials with low surface energy can be added into the colloidal solution to provide the created surface with hydrophobicity. Sol-gel process is often used with other process such as spin-coating, spray coating to provide the surface with textured pattern. Lakshimi et al.[59] reported the fabrication of superhydrophobic coatings with improved hardness using sol-gel process by embedding fumed silica nanoparticles in a partially condensed hybrid sol of methyltriethoxysilane (MTEOS) and colloidal silica.

They incorporated fumed silica particles of size 25-30 nm in the sol and utilized the spray coating method to spray the mixture onto glass substrate to induce the roughness. Liu et al.[3] created transparent and self-cleaning superhydrophobic coatings by the sol-gel process with long-chain fluoroalkylsilane. They dipped coated the precursor onto glass substrate. The dried coating surface exhibited a rough, wrinkled, hill-like morphology and provided the coating with superhydrophobicity.

1.1.5.8 Spray Deposition.

Spray deposition is a simple, one-step industrially viable process with a long history in coatings technology. It is an industrial implementation method which can be used in large-scale substrate, the apparatus is cheap, and there is not much limitation on the applied material. Given such advantages, it has been recently wildly applied for the preparation of superhydrophobic surface from the deposition of nanoparticle suspensions,[70, 71] polymer/nanoparticle blends,[72-74] sol-gel precursors,[75] and copolymers on substrates of various shapes and compositions.[76] Campos et al.[62] fabricated a set of coatings with wetting property ranging from hydrophobicity to superoleophobicity via spray deposition method with fluoroalkylsilane-treated precipitated silica aggregates. Hsu et al.[63] reported robust superhydrophobic epoxy coating via spray method using polyamine sispersed carbon nanotubes. Ge and coauthor[64] created transparent superamphiphobic surfaces from one-step spray coating of stringed silica nanoparticle/sol solutions.

1.2 Challenge and Opportunity

Nature has inspired many people and offered design principles for the creation of artificial multifunctional surfaces with multi-scale structures. Most of current works

focus on the reproduce of multiscale structures using different approaches. In the near future, more research needs to be applied to move superhydrophobic surfaces toward real-world applications. Daily applications of surfaces with special wettability (e.g superhydrophobicity) benefit from properties such as superoleophobicity, transparency and/or mechanical robustness. However, the requirement to achieving the aforementioned properties render the creation of such surfaces both a challenge and an opportunity.

1.2.1 Superamphiphobicity.

Superamphiphobic surfaces show high contact angles (>150°) and low sliding angles (<5°) in contact with both water and non-polar liquids, extending the advantages of superhydrophobic surfaces to oily/organic liquids.[77-80] Superamphiphobic surfaces are less prone to contamination, thus the application space is significantly broadened for such materials. Since no organic liquid shows a Young's contact angle above 90° with any planar solid surface, superamphiphobic surface fabricating it is not sufficient to simply roughen the surface of low surface energy materials, carefully manipulated surface structures are required(e.g. overhang architecture).[81-85]

1.2.2 Superhydrophobic Coating with Transparency.

Transparent superhydrophobic coatings have huge values in both aesthetics and practice applications such as mirrors, windshields and optical devices.[86-88] Most superhydrophobic surfaces are either opaque or translucent. The hierarchical structures on the opaque superhydrophobic surfaces range from a few nanometers to a few hundred nanometers – thus scattering off visible lights (350-750 nm). In order to prepare transparent superhydrophobic coatings, roughness features smaller than 100 nm are

needed. The real challenge is how to prepare superhdrophobic coating with roughness scale under 100 nm using simple and cost effective approach.

1.2.3 Superhydrophobic Coating with Mechanical Durability.

Superhydrophic surfaces with robust mechanical property and durability has been one of the most important and challenging field of study.[89-91] As previously described by the Cassie-Baxter model, the superhydrophobicity of a given surface relies on the roughness features in micro and sub-micro scales that reduce actual water contact area by trapping 'air pockets' in between the surface and the water droplets. The micro/sub-micro structures, owing to its scale, are fragile and can be easily worn off by abrasion, scratching and/or environmental exposures. Once the delicate roughness features are gone so is the superhydrophobicity.

The work of this dissertation is focused on these challenges, especially the superamphiphobicity and the improvement of mechanical durability to promote the application in real-world.

1.3 Thiol-Ene Photopolymerization

Photopolymerization is a process in which light energy is used to initiate chain-producing reactions converting reactive monomers to macromolecules. Photopolymerization has received growing attentions in both industry and academia due to many advantages over thermal polymerization, including solvent-free systems, decreased energy consumption and allowing room temperature polymerizations. For a long time, photopolymerizations based on acrylate and methacrylate systems have long been used for commercial applications in medical care (e.g. dental materials), 3D printing, adhesives and coating fabrications. However, the drawbacks of acrylate/

methacrylate-based systems including oxygen sensitivity,[92-94] high shrinkage[95, 96] and heterogeneity within the formed network[97-99] limit their further applications.

Thiol–ene photopolymerization,[100-103] as an alternative, directly addresses the drawbacks of the traditional acrylate/methacrylate photopolymerization systems exhibiting several properties such as low shrinkage, and low sensitivity toward water and oxygen. Furthermore, thiol-ene photopolymerization reaction is known for rapid formation of highly uniform polymer networks with narrow glass transitions and tailorable mechanical properties.[104-107] Given such advantages, thiol-ene chemistry is commonly used for the formation of crosslinked networks from bulk materials[108, 109] to photo-cured thin films,[110, 111] photo-patterned lithography,[112, 113] and photo-cured hydrogels[114-116] applications.

Extensive studies have revealed that the thiol–ene reaction proceeds as a radical step-growth mechanism with initiation, propagation and termination steps as represented in Scheme 1.[101-103] At first, the reaction is initiated to generate radicals through hydrogen abstraction or cleave type photoinitiators. The generated radical abstract hydrogen from the thiol formed a thiyl radical. The resulted thiyl radical then reversibly adds across any accessible C-C double-bond yielding an intermediate carbon-centered radical followed by chain-transfer to a second thiol group to give the final thiol–ene addition product. The mechanism continuously regenerates the thiyl radical, allowing the polymerization to be propagated incessantly in an alternate sequence with equal amount of thiol–ene reactants are exhausted. Termination reactions are usually involved the radical-radical (re)combination.

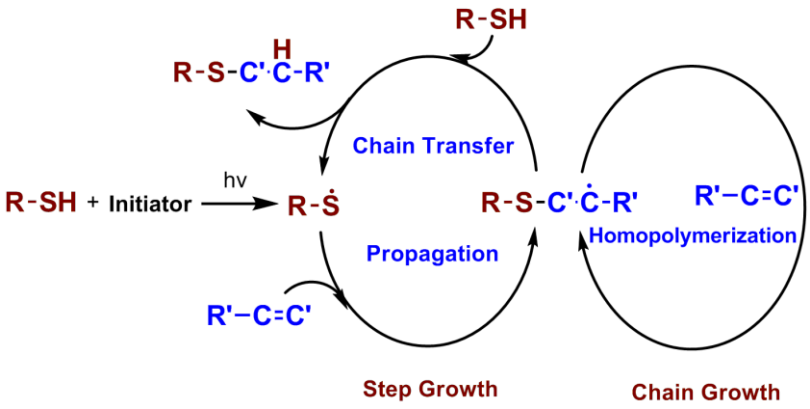

Scheme 1.3 Thiol-ene reaction mechanism.

Chain growth is also an important mechanism that occurred in many thiol-ene reactions. A carbon-centered radical generated during the step growth mechanism can react with an ene group and yields another carbon centered radical via an addition reaction. The combined step growth and chain growth mechanism is called binary thiol-acrylate mechanism because this normally occurred in thiol acrylate/methacrylate systems. The mechanism of the reaction depends on the reactivity of alkene compounds. Alkenes with low reactivity such as norbornenes, allyl ethers, and vinyl ethers,[117] favor the step growth mechanism while alkenes with high reactivity such as acrylate, and methacrylate[118, 119] favor the binary thiol-acrylate mechanism.

Compared to traditional addition reactions of acrylates/methacrylates, the presence of thiols greatly decreased the oxygen inhibition effect of the polymerization, allowing acrylates/methacrylates to react without in an inert atmosphere. Furthermore, the added thiol moiety which goes through step-growth in the reaction forms small molecular weight species before the gelation resulted in the delayed gel point conversion and reduced shrinkage of the polymer network.[119-121] Despite these advantages, the participated chain growth cycle leads to the residue of thiol functional group results in the

decreased conversion which affects the property of the polymer.[118, 122] In this dissertation, both thiol-ene and thiol-acrylate photopolymerization are involved.

1.4 Summary and Research Overview

Bioinspired inspired superhydrophobic coatings have attracted a tremendous amount of research interests due to the potential application in both academia and industry. Extensively studies have been revealed that the superhydrophobic wetting property can be attributed to both chemical composition and geometric parameters (i.e. roughness) of the solid interface which govern the artificial fabrication approaches. The specific application of superhydrophobic coatings in real world requires the coating possess other desirable properties, such as superoleophobicity and mechanical durability using low cost and simple approach.

This dissertation is focused on the design and fabrication of wetting and anti-wetting surfaces via thiol-ene photopolymerization with addressed aforementioned properties.

In Chapter II, a simple strategy for fabrication of superamphiphobic coatings based on photopolymerization of hybrid thiol-ene resins was presented. Spray deposition and UV cure of thiol-ene resins containing hydrophobic silica nanoparticles and fluorinated thiols provides multi-scale topography and low-energy surface that endows the surface with superamphiphobicity and repellency towards several low surface tension liquids. Droplet impact and sandpaper abrasion tests indicate the coatings respectively possess a robust anti-wetting behavior and good mechanical durability.

In Chapter III, We report a simple, rapid, and one-pot approach to fabricate superhydrophilic/superoleophobic surface by hydrophilic and oleophobic thiol-acrylate

chemical compositions involved with inorganic nano-particle and spray deposition method created surface roughness. A functional compound with long fluorine carbon chain was introduced into the system via covalent bond. The wetting study showed extreme oil repellency and water affinity suggestion a likely use in oil/waster separation treatment. The nature of this type of material allows the pass of bottom water layer and rejects the top oil layer which can also minimize the oil fouling issue. The performances of this superhydrophilic/superoleophobic coating on oil/water emulsion and dye contained emulsion separation were studied and compared with the separation efficiency of superhydrophilic/superoleophilic coating. The results showed the extra fluorine compound provide the membrane with high oil and dye rejection ratios indicating the potential application in wastewater treatment.

In Chapter IV, we demonstrated a novel strategy to fabricate coatings of multiscale roughness with 50% less NPs content to achieve superhydrophobicity by employing spray deposition and porogen leaching. The effect of porogen concentration and molecular weight on the surface morphology and wetting property was studied. The fabricated surface exhibited reversibility between lubricant infused slippery hydrophobic and air pocket trapped superhydrophobic surface.

1.5 References

1. Wang, S.; Jiang, L., Definition of Superhydrophobic States. *Advanced Materials* **2007,** *19*, 3423-3424.
2. Bhushan, B.; Jung, Y. C., Natural and biomimetic artificial surfaces for superhydrophobicity, self-cleaning, low adhesion, and drag reduction. *Progress in Materials Science* **2011,** *56*, 1-108.
3. Liu, S.; Liu, X.; Latthe, S. S.; Gao, L.; An, S.; Yoon, S. S.; Liu, B.; Xing, R., Self-cleaning transparent superhydrophobic coatings through simple sol–gel processing of fluoroalkylsilane. *Applied Surface Science* **2015,** *351*, 897-903.
4. Matin, A.; Merah, N.; Ibrahim, A., Superhydrophobic and self-cleaning surfaces prepared from a commercial silane using a single-step drop-coating method. *Progress in Organic Coatings* **2016,** *99*, 322-329.
5. Daniello, R. J.; Waterhouse, N. E.; Rothstein, J. P., Drag reduction in turbulent flows over superhydrophobic surfaces. *Physics of Fluids* **2009,** *21*, 085103.
6. Lyu, S.; Nguyen, D. C.; Kim, D.; Hwang, W.; Yoon, B., Experimental drag reduction study of super-hydrophobic surface with dual-scale structures. *Applied Surface Science* **2013,** *286*, 206-211.
7. Zhang, S.; Ouyang, X.; Li, J.; Gao, S.; Han, S.; Liu, L.; Wei, H., Underwater Drag-Reducing Effect of Superhydrophobic Submarine Model. *Langmuir* **2015,** *31*, 587-593.
8. Liu, T.; Yin, Y.; Chen, S.; Chang, X.; Cheng, S., Super-hydrophobic surfaces improve corrosion resistance of copper in seawater. *Electrochimica Acta* **2007,** *52*, 3709-3713.
9. Ishizaki, T.; Masuda, Y.; Sakamoto, M., Corrosion Resistance and Durability of Superhydrophobic Surface Formed on Magnesium Alloy Coated with Nanostructured Cerium Oxide Film and Fluoroalkylsilane Molecules in Corrosive NaCl Aqueous Solution. *Langmuir* **2011,** *27*, 4780-4788.
10. Mohamed, A. M. A.; Abdullah, A. M.; Younan, N. A., Corrosion behavior of superhydrophobic surfaces: A review. *Arabian Journal of Chemistry* **2015,** *8*, 749-765.
11. Jafari, R.; Menini, R.; Farzaneh, M., Superhydrophobic and icephobic surfaces prepared by RF-sputtered polytetrafluoroethylene coatings. *Applied Surface Science* **2010,** *257*, 1540-1543.
12. Guo, P.; Zheng, Y.; Wen, M.; Song, C.; Lin, Y.; Jiang, L., Icephobic/anti-icing properties of micro/nanostructured surfaces. *Adv Mater* **2012,** *24*, 2642-8.
13. Liu, J.; Janjua, Z.; Roe, M.; Xu, F.; Turnbull, B.; Choi, K.-S.; Hou, X., Super-Hydrophobic/Icephobic Coatings Based on Silica Nanoparticles Modified by Self-Assembled Monolayers. *Nanomaterials* **2016,** *6*, 232.
14. Li, X.-M.; Reinhoudt, D.; Crego-Calama, M., What do we need for a superhydrophobic surface? A review on the recent progress in the preparation of superhydrophobic surfaces. *Chemical Society Reviews* **2007,** *36*, 1350-1368.
15. Zhang, X.; Shi, F.; Niu, J.; Jiang, Y.; Wang, Z., Superhydrophobic surfaces: from structural control to functional application. *Journal of Materials Chemistry* **2008,** *18*, 621-633.
16. Onda, T.; Shibuichi, S.; Satoh, N.; Tsujii, K., Super-Water-Repellent Fractal Surfaces. *Langmuir* **1996,** *12*, 2125-2127.
17. Lafuma, A.; Quere, D., Superhydrophobic states. *Nat Mater* **2003,** *2*, 457-60.
18. Wenzel, R. N., RESISTANCE OF SOLID SURFACES TO WETTING BY WATER. *Industrial & Engineering Chemistry* **1936,** *28*, 988-994.
19. Bhushan, B.; Jung, Y. C.; Koch, K., Micro-, nano- and hierarchical structures for superhydrophobicity, self-cleaning and low adhesion. *Philos Trans A Math Phys Eng Sci* **2009,** *367*, 1631-72.

20. Liu, K.; Tian, Y.; Jiang, L., Bio-inspired superoleophobic and smart materials: Design, fabrication, and application. *Progress in Materials Science* **2013,** *58*, 503-564.
21. Cassie, A. B. D.; Baxter, S., Wettability of porous surfaces. *Transactions of the Faraday Society* **1944,** *40*, 546-551.
22. Tuteja, A.; Choi, W.; Ma, M.; Mabry, J. M.; Mazzella, S. A.; Rutledge, G. C.; McKinley, G. H.; Cohen, R. E., Designing Superoleophobic Surfaces. *Science* **2007,** *318*, 1618.
23. Yao, X.; Song, Y.; Jiang, L., Applications of bio-inspired special wettable surfaces. *Adv Mater* **2011,** *23*, 719-34.
24. Subhash Latthe, S.; Basavraj Gurav, A.; Shridhar Maruti, C.; Shrikant Vhatkar, R., Recent Progress in Preparation of Superhydrophobic Surfaces: A Review. *Journal of Surface Engineered Materials and Advanced Technology* **2012,** *02*, 76-94.
25. Celia, E.; Darmanin, T.; Taffin de Givenchy, E.; Amigoni, S.; Guittard, F., Recent advances in designing superhydrophobic surfaces. *J Colloid Interface Sci* **2013,** *402*, 1-18.
26. Sun, T.; Feng, L.; Gao, X.; Jiang, L., Bioinspired Surfaces with Special Wettability. *Accounts of Chemical Research* **2005,** *38*, 644-652.
27. Marmur, A., The Lotus Effect: Superhydrophobicity and Metastability. *Langmuir* **2004,** *20*, 3517-3519.
28. Patankar, N. A., Mimicking the Lotus Effect: Influence of Double Roughness Structures and Slender Pillars. *Langmuir* **2004,** *20*, 8209-8213.
29. Sun, M.; Luo, C.; Xu, L.; Ji, H.; Ouyang, Q.; Yu, D.; Chen, Y., Artificial Lotus Leaf by Nanocasting. *Langmuir* **2005,** *21*, 8978-8981.
30. Barthlott, W.; Neinhuis, C., Purity of the sacred lotus, or escape from contamination in biological surfaces. *Planta* **1997,** *202*, 1-8.
31. Feng, L.; Li, S.; Li, Y.; Li, H.; Zhang, L.; Zhai, J.; Song, Y.; Liu, B.; Jiang, L.; Zhu, D., Super-Hydrophobic Surfaces: From Natural to Artificial. *Advanced Materials* **2002,** *14*, 1857-1860.
32. Feng, X. J.; Jiang, L., Design and Creation of Superwetting/Antiwetting Surfaces. *Advanced Materials* **2006,** *18*, 3063-3078.
33. Zheng, Y.; Gao, X.; Jiang, L., Directional adhesion of superhydrophobic butterfly wings. *Soft Matter* **2007,** *3*, 178-182.
34. Gao, X.; Jiang, L., Biophysics: Water-repellent legs of water striders. *Nature* **2004,** *432*, 36-36.
35. F., L.; Y., Z.; J., X.; Y., Z.; N., W.; F., X.; L., J., Petal Efeect: A Superhydrophobic State with High Adhesive Force. *Langmuir* **2008,** *24*, 6.
36. Su, C.; Xu, Y.; Gong, F.; Wang, F.; Li, C., The abrasion resistance of a superhydrophobic surface comprised of polyurethane elastomer. *Soft Matter* **2010,** *6*, 6068.
37. Zhao, W.; Wang, L.; Xue, Q., Fabrication of Low and High Adhesion Hydrophobic Au Surfaces with Micro/Nano-Biomimetic Structures. *The Journal of Physical Chemistry C* **2010,** *114*, 11509-11514.
38. Xu, Q. F.; Mondal, B.; Lyons, A. M., Fabricating superhydrophobic polymer surfaces with excellent abrasion resistance by a simple lamination templating method. *ACS Appl Mater Interfaces* **2011,** *3*, 3508-14.
39. Deng, X.; Mammen, L.; Butt, H. J.; Vollmer, D., Candle soot as a template for a transparent robust superamphiphobic coating. *Science* **2012,** *335*, 67-70.
40. Choi, Y.; Brugarolas, T.; Kang, S. M.; Park, B. J.; Kim, B. S.; Lee, C. S.; Lee, D., Beauty of lotus is more than skin deep: highly buoyant superhydrophobic films. *ACS Appl Mater Interfaces* **2014,** *6*, 7009-13.
41. Latthe, S. S.; Terashima, C.; Nakata, K.; Fujishima, A., Superhydrophobic surfaces developed by mimicking hierarchical surface morphology of lotus leaf. *Molecules* **2014,** *19*, 4256-83.

42. Martines, E.; Seunarine, K.; Morgan, H.; Gadegaard, N.; Wilkinson, C. D. W.; Riehle, M. O., Superhydrophobicity and Superhydrophilicity of Regular Nanopatterns. *Nano Letters* **2005,** *5*, 2097-2103.
43. Bhushan, B.; Chae Jung, Y., Wetting study of patterned surfaces for superhydrophobicity. *Ultramicroscopy* **2007,** *107*, 1033-41.
44. Im, M.; Im, H.; Lee, J.-H.; Yoon, J.-B.; Choi, Y.-K., A robust superhydrophobic and superoleophobic surface with inverse-trapezoidal microstructures on a large transparent flexible substrate. *Soft Matter* **2010,** *6*, 1401.
45. Zhao, H.; Law, K. Y., Directional self-cleaning superoleophobic surface. *Langmuir* **2012,** *28*, 11812-8.
46. Han, J. T.; Xu, X. R.; Cho, K. W., Diverse Access to Artificial Superhydrophobic Surfaces Using Block Copolymers. *Langmuir* **2005,** *21*, 4.
47. Zhao, N.; Xie, Q.; L., W.; Wang, S.; Zhang, X.; Xu, J., Superhydrophobic Surface from Vapor-Induced Phase Separation of Copolymer Micellar Solution. *Macromolecules* **2005,** *38*, 4.
48. Zhao, N.; Zhang, X.; Zhang, X.; Xu, J., Simultaneous tuning of chemical composition and topography of copolymer surfaces: micelles as building blocks. *Chemphyschem* **2007,** *8*, 1108-14.
49. Jiang, L.; Zhao, Y.; Zhai, J., A lotus-leaf-like superhydrophobic surface: a porous microsphere/nanofiber composite film prepared by electrohydrodynamics. *Angew Chem Int Ed Engl* **2004,** *43*, 4338-41.
50. Wu, J.; Wang, N.; Wang, L.; Dong, H.; Zhao, Y.; Jiang, L., Electrospun porous structure fibrous film with high oil adsorption capacity. *ACS Appl Mater Interfaces* **2012,** *4*, 3207-12.
51. Pan, S.; Kota, A. K.; Mabry, J. M.; Tuteja, A., Superomniphobic surfaces for effective chemical shielding. *J Am Chem Soc* **2013,** *135*, 578-81.
52. Lau., K. K. S.; José, B.; Teo., K. B. K.; Chhowalla, Superhydrophobic Carbon Nanotube Forests. *Nano Letters* **2003,** *3*, 5.
53. Deng, X.; Mammen, L.; Zhao, Y.; Lellig, P.; Mullen, K.; Li, C.; Butt, H. J.; Vollmer, D., Transparent, thermally stable and mechanically robust superhydrophobic surfaces made from porous silica capsules. *Adv Mater* **2011,** *23*, 2962-5.
54. Shibuichi, S.; Onda, T.; Satoh, N.; Tsujii, K., Super Water-Repellent Surfaces Resulting from Fractal Structure. *The Journal of Physical Chemistry* **1996,** *100*, 19512-19517.
55. Xiu, Y.; Liu, Y.; Hess, D. W.; Wong, C. P., Mechanically robust superhydrophobicity on hierarchically structured Si surfaces. *Nanotechnology* **2010,** *21*, 155705.
56. Kondrashov, V.; Ruhe, J., Microcones and nanograss: toward mechanically robust superhydrophobic surfaces. *Langmuir* **2014,** *30*, 4342-50.
57. Peng, S.; Yang, X.; Tian, D.; Deng, W., Chemically stable and mechanically durable superamphiphobic aluminum surface with a micro/nanoscale binary structure. *ACS Appl Mater Interfaces* **2014,** *6*, 15188-97.
58. Liu, Y.; Chen, X.; Xin, J. H., Super-hydrophobic surfaces from a simple coating method: a bionic nanoengineering approach. *Nanotechnology* **2006,** *17*, 3259-3263.
59. Lakshmi, R. V.; Bharathidasan, T.; Basu, B. J., Superhydrophobic sol–gel nanocomposite coatings with enhanced hardness. *Applied Surface Science* **2011,** *257*, 10421-10426.
60. Hanaor, D. A. H.; Chironi, I.; Karatchevtseva, I.; Triani, G.; Sorrell, C. C., Single and mixed phase TiO2powders prepared by excess hydrolysis of titanium alkoxide. *Advances in Applied Ceramics* **2013,** *111*, 149-158.
61. Jung, Y. C.; Bhushan, B., Mechanically Durable Carbon Nanotube−Composite Hierarchical Structures with Superhydrophobicity, Self-Cleaning, and Low-Drag. *ACS Nano* **2009,** *3*, 4155-4163.

62. Campos, R.; Guenthner, A. J.; Meuler, A. J.; Tuteja, A.; Cohen, R. E.; McKinley, G. H.; Haddad, T. S.; Mabry, J. M., Superoleophobic surfaces through control of sprayed-on stochastic topography. *Langmuir* **2012,** *28*, 9834-41.
63. Hsu, C. P.; Chang, L. Y.; Chiu, C. W.; Lee, P. T.; Lin, J. J., Facile fabrication of robust superhydrophobic epoxy film with polyamine dispersed carbon nanotubes. *ACS Appl Mater Interfaces* **2013,** *5*, 538-45.
64. Ge, D.; Yang, L.; Zhang, Y.; Rahmawan, Y.; Yang, S., Transparent and Superamphiphobic Surfaces from One-Step Spray Coating of Stringed Silica Nanoparticle/Sol Solutions. *Particle & Particle Systems Characterization* **2014,** *31*, 763-770.
65. Bhushan, B.; Chae Jung, Y., Wetting study of patterned surfaces for superhydrophobicity. *Ultramicroscopy* **2007,** *107*, 1033-1041.
66. Dubinsky, S.; Petukhova, A.; Gourevich, I.; Kumacheva, E., A study of polymerization-induced phase separation as a route to produce porous polymer-metal materials. *Macromol Rapid Commun* **2010,** *31*, 1635-40.
67. Dubinsky, S.; Petukhova, A.; Gourevich, I.; Kumacheva, E., Hybrid porous material produced by polymerization-induced phase separation. *Chem Commun (Camb)* **2010,** *46*, 2578-80.
68. Myungeun Seo, M. A. H., Reticulated Nanoporous Polymers by Controlled Polymerization-Induced Microphase Separation. *Science* **2012,** *336*, 3.
69. Saba, S. A.; Mousavi, M. P.; Buhlmann, P.; Hillmyer, M. A., Hierarchically Porous Polymer Monoliths by Combining Controlled Macro- and Microphase Separation. *J Am Chem Soc* **2015,** *137*, 8896-9.
70. Ogihara, H.; Okagaki, J.; Saji, T., Facile Fabrication of Colored Superhydrophobic Coatings by Spraying a Pigment Nanoparticle Suspension. *Langmuir* **2011,** *27*, 9069-9072.
71. Ogihara, H.; Xie, J.; Okagaki, J.; Saji, T., Simple Method for Preparing Superhydrophobic Paper: Spray-Deposited Hydrophobic Silica Nanoparticle Coatings Exhibit High Water-Repellency and Transparency. *Langmuir* **2012,** *28*, 4605-4608.
72. Srinivasan, S.; Chhatre, S. S.; Mabry, J. M.; Cohen, R. E.; McKinley, G. H., Solution spraying of poly(methyl methacrylate) blends to fabricate microtextured, superoleophobic surfaces. *Polymer* **2011,** *52*, 3209-3218.
73. Wang, X.; Hu, H.; Ye, Q.; Gao, T.; Zhou, F.; Xue, Q., Superamphiphobic coatings with coralline-like structure enabled by one-step spray of polyurethane/carbon nanotube composites. *Journal of Materials Chemistry* **2012,** *22*, 9624-9631.
74. Sparks, B. J.; Hoff, E. F. T.; Xiong, L.; Goetz, J. T.; Patton, D. L., Superhydrophobic Hybrid Inorganic–Organic Thiol-ene Surfaces Fabricated via Spray-Deposition and Photopolymerization. *ACS Applied Materials & Interfaces* **2013,** *5*, 1811-1817.
75. Shang, Q.; Zhou, Y.; Xiao, G., A simple method for the fabrication of silica-based superhydrophobic surfaces. *Journal of Coatings Technology and Research* **2014,** *11*, 509-515.
76. Li, H.; Zhao, X.; Chu, G.; Zhang, S.; Yuan, X., One-step fabrication of a superhydrophobic polymer surface from an acrylic copolymer containing POSS by spraying. *RSC Advances* **2014,** *4*, 62694-62697.
77. Tuteja, A.; Choi, W.; Ma, M.; Mabry, J. M.; Mazzella, S. A.; Rutledge, G. C.; McKinley, G. H.; Cohen, R. E., Designing superoleophobic surfaces. *Science* **2007,** *318*, 1618-22.
78. Tuteja, A.; Choi, W.; Mabry, J. M.; McKinley, G. H.; Cohen, R. E., Robust omniphobic surfaces. *Proc Natl Acad Sci U S A* **2008,** *105*, 18200-5.
79. Tuteja, A.; Choi, W.; McKinley, G. H.; Cohen, R. E.; Rubner, M. F., Design Parameters for Superhydrophobicity and Superoleophobicity. *MRS Bulletin* **2008,** *33*, 752-758.
80. Xue, Z.; Liu, M.; Jiang, L., Recent developments in polymeric superoleophobic surfaces. *Journal of Polymer Science Part B: Polymer Physics* **2012,** *50*, 1209-1224.

81. Xie, Q.; Xu, J.; Feng, L.; Jiang, L.; Tang, W.; Luo, X.; Han, C. C., Facile Creation of a Super-Amphiphobic Coating Surface with Bionic Microstructure. *Advanced Materials* **2004,** *16*, 302-305.
82. Darmanin, T.; Guittard, F., One-pot method for build-up nanoporous super oil-repellent films. *J Colloid Interface Sci* **2009,** *335*, 146-9.
83. Wang, X.; Liu, X.; Zhou, F.; Liu, W., Self-healing superamphiphobicity. *Chem Commun (Camb)* **2011,** *47*, 2324-6.
84. Kota, A. K.; Li, Y.; Mabry, J. M.; Tuteja, A., Hierarchically structured superoleophobic surfaces with ultralow contact angle hysteresis. *Adv Mater* **2012,** *24*, 5838-43.
85. Zhu, X.; Zhang, Z.; Xu, X.; Men, X.; Yang, J.; Zhou, X.; Xue, Q., Facile fabrication of a superamphiphobic surface on the copper substrate. *J Colloid Interface Sci* **2012,** *367*, 443-9.
86. Xu, L.; Karunakaran, R. G.; Guo, J.; Yang, S., Transparent, Superhydrophobic Surfaces from One-Step Spin Coating of Hydrophobic Nanoparticles. *ACS Applied Materials & Interfaces* **2012,** *4*, 1118-1125.
87. Lee, S. G.; Ham, D. S.; Lee, D. Y.; Bong, H.; Cho, K., Transparent Superhydrophobic/Translucent Superamphiphobic Coatings Based on Silica–Fluoropolymer Hybrid Nanoparticles. *Langmuir* **2013,** *29*, 15051-15057.
88. Mates, J. E.; Ibrahim, R.; Vera, A.; Guggenheim, S.; Qin, J.; Calewarts, D.; Waldroup, D. E.; Megaridis, C. M., Environmentally-safe and transparent superhydrophobic coatings. *Green Chemistry* **2016,** *18*, 2185-2192.
89. Verho, T.; Bower, C.; Andrew, P.; Franssila, S.; Ikkala, O.; Ras, R. H., Mechanically durable superhydrophobic surfaces. *Adv Mater* **2011,** *23*, 673-8.
90. Sarkar, A.; Kietzig, A. M., Design of a robust superhydrophobic surface: thermodynamic and kinetic analysis. *Soft Matter* **2015,** *11*, 1998-2007.
91. X., T.; T., V.; R., R., Moving superhydrophobic surfaces toward real-world applications. *Science* **2016,** *352*, 142-143.
92. Roper, T. M.; Lee, T. Y.; Guymon, C. A.; Hoyle, C. E., In Situ Characterization of Photopolymerizable Systems Using a Thin-Film Calorimeter. *Macromolecules* **2005,** *38*, 10109-10116.
93. Gou, L.; Opheim, B.; Coretsopoulos, C. N.; Scranton, A. B., CONSUMPTION OF THE MOLECULAR OXYGEN IN POLYMERIZATION SYSTEMS USING PHOTOSENSITIZED OXIDATION OF DIMETHYLANTHRACENE. *Chemical Engineering Communications* **2006,** *193*, 620-627.
94. Bowman, C. N.; Kloxin, C. J., Toward an enhanced understanding and implementation of photopolymerization reactions. *AIChE Journal* **2008,** *54*, 2775-2795.
95. Bowman, C. N.; Peppas, N. A., Coupling of kinetics and volume relaxation during polymerizations of multiacrylates and multimethacrylates. *Macromolecules* **1991,** *24*, 1914-1920.
96. Lu, H.; Stansbury, J. W.; Bowman, C. N., Towards the elucidation of shrinkage stress development and relaxation in dental composites. *Dental Materials* **2004,** *20*, 979-986.
97. Simon, G. P.; Allen, P. E. M.; Bennett, D. J.; Williams, D. R. G.; Williams, E. H., Nature of residual unsaturation during cure of dimethacrylates examined by CPPEMAS carbon-13 NMR and simulation using a kinetic gelation model. *Macromolecules* **1989,** *22*, 3555-3561.
98. Kannurpatti, A. R.; Anderson, K. J.; Anseth, J. W.; Bowman, C. N., Use of "living" radical polymerizations to study the structural evolution and properties of highly crosslinked polymer networks. *Journal of Polymer Science Part B: Polymer Physics* **1997,** *35*, 2297-2307.
99. Kannurpatti, A. R.; Anseth, J. W.; Bowman, C. N., A study of the evolution of mechanical properties and structural heterogeneity of polymer networks formed by photopolymerizations of multifunctional (meth)acrylates. *Polymer* **1998,** *39*, 2507-2513.
100. Kolb, H. C.; Finn, M. G.; Sharpless, K. B., Click Chemistry: Diverse Chemical Function from a Few Good Reactions. *Angewandte Chemie International Edition* **2001,** *40*, 2004-2021.

101. Hoyle, C. E.; Lee, T. Y.; Roper, T., Thiol–enes: Chemistry of the past with promise for the future. *Journal of Polymer Science Part A: Polymer Chemistry* **2004,** *42*, 5301-5338.
102. Hoyle, C. E.; Bowman, C. N., Thiol-ene click chemistry. *Angew Chem Int Ed Engl* **2010,** *49*, 1540-73.
103. Kade, M. J.; Burke, D. J.; Hawker, C. J., The power of thiol-ene chemistry. *Journal of Polymer Science Part A: Polymer Chemistry* **2010,** *48*, 743-750.
104. Kozhushkov, S. I.; Brandl, M.; de Meijere, A., Surprisingly Facile Addition of Thiols to the Double Bonds of Bicyclopropylidene and Other Methylenecyclopropanes. *European Journal of Organic Chemistry* **1998,** *1998*, 1535-1542.
105. Roper, T. M.; Guymon, C. A.; Jönsson, E. S.; Hoyle, C. E., Influence of the alkene structure on the mechanism and kinetics of thiol-alkene photopolymerizations with real-time infrared spectroscopy. *Journal of Polymer Science Part A: Polymer Chemistry* **2004,** *42*, 6283-6298.
106. Northrop, B. H.; Coffey, R. N., Thiol-ene click chemistry: computational and kinetic analysis of the influence of alkene functionality. *J Am Chem Soc* **2012,** *134*, 13804-17.
107. Nguyen, L.-T. T.; Gokmen, M. T.; Du Prez, F. E., Kinetic comparison of 13 homogeneous thiol–X reactions. *Polymer Chemistry* **2013,** *4*, 5527.
108. Cramer, N. B.; Couch, C. L.; Schreck, K. M.; Boulden, J. E.; Wydra, R.; Stansbury, J. W.; Bowman, C. N., Properties of methacrylate-thiol-ene formulations as dental restorative materials. *Dent Mater* **2010,** *26*, 799-806.
109. Wilderbeek, H. T. A.; Goossens, J. G. P.; Bastiaansen, C. W. M.; Broer, D. J., Photoinitiated Bulk Polymerization of Liquid Crystalline Thiolene Monomers. *Macromolecules* **2002,** *35*, 8962-8968.
110. Wang, C.; Lee, W.-Y.; Nakajima, R.; Mei, J.; Kim, D. H.; Bao, Z., Thiol–ene Cross-Linked Polymer Gate Dielectrics for Low-Voltage Organic Thin-Film Transistors. *Chemistry of Materials* **2013,** *25*, 4806-4812.
111. Bae, J.; Yang, Y., Thiol-ene/hyperbranched polymer hybrid thin films: Cure behavior and gas barrier properties. *Journal of Non-Crystalline Solids* **2011,** *357*, 3103-3107.
112. Lyon, G. B.; Cox, L. M.; Goodrich, J. T.; Baranek, A. D.; Ding, Y.; Bowman, C. N., Remoldable Thiol–Ene Vitrimers for Photopatterning and Nanoimprint Lithography. *Macromolecules* **2016,** *49*, 8905-8913.
113. Dübner, M.; Gevrek, T. N.; Sanyal, A.; Spencer, N. D.; Padeste, C., Fabrication of Thiol–Ene "Clickable" Copolymer-Brush Nanostructures on Polymeric Substrates via Extreme Ultraviolet Interference Lithography. *ACS Applied Materials & Interfaces* **2015,** *7*, 11337-11345.
114. Du, H.; Zha, G.; Gao, L.; Wang, H.; Li, X.; Shen, Z.; Zhu, W., Fully biodegradable antibacterial hydrogels via thiol-ene "click" chemistry. *Polymer Chemistry* **2014,** *5*, 4002-4008.
115. Sawicki, L. A.; Kloxin, A. M., Design of thiol-ene photoclick hydrogels using facile techniques for cell culture applications. *Biomaterials Science* **2014,** *2*, 1612-1626.
116. Kharkar, P. M.; Rehmann, M. S.; Skeens, K. M.; Maverakis, E.; Kloxin, A. M., Thiol–ene Click Hydrogels for Therapeutic Delivery. *ACS Biomaterials Science & Engineering* **2016,** *2*, 165-179.
117. Cramer, N. B.; Reddy, S. K.; O'Brien, A. K.; Bowman, C. N., Thiol−Ene Photopolymerization Mechanism and Rate Limiting Step Changes for Various Vinyl Functional Group Chemistries. *Macromolecules* **2003,** *36*, 7964-7969.
118. Cramer, N. B.; Bowman, C. N., Kinetics of thiol-ene and thiol-acrylate photopolymerizations with real-time fourier transform infrared. *Journal of Polymer Science Part A: Polymer Chemistry* **2001,** *39*, 3311-3319.
119. O'Brien, A. K.; Cramer, N. B.; Bowman, C. N., Oxygen inhibition in thiol–acrylate photopolymerizations. *Journal of Polymer Science Part A: Polymer Chemistry* **2006,** *44*, 2007-2014.

120. Roper, T. M.; Kwee, T.; Lee, T. Y.; Guymon, C. A.; Hoyle, C. E., Photopolymerization of pigmented thiol–ene systems. *Polymer* **2004,** *45*, 2921-2929.
121. Dickey, M. D.; Collister, E.; Raines, A.; Tsiartas, P.; Holcombe, T.; Sreenivasan, S. V.; Bonnecaze, R. T.; Willson, C. G., Photocurable Pillar Arrays Formed via Electrohydrodynamic Instabilities. *Chemistry of Materials* **2006,** *18*, 2043-2049.
122. Cramer, N. B.; Couch, C. L.; Schreck, K. M.; Carioscia, J. A.; Boulden, J. E.; Stansbury, J. W.; Bowman, C. N., Investigation of thiol-ene and thiol-ene-methacrylate-based resins as dental restorative materials. *Dent Mater* **2010,** *26*, 21-8.

CHAPTER II - SPRAY-DEPOSITION AND PHOTOPOLYMERIZATION OF ORGANIC-INORGANIC THIOL-ENE RESINS FOR FABRICATION OF SUPERAMPHIPHOBIC SURFACES

2.1 Introduction

Tailoring of solid-liquid interfacial interactions, such as wettability, is a subject of paramount importance in materials research and offers broad-reaching implications for a variety of everyday and technological applications.[1] Nature offers many awe-inspiring examples of engineered interfaces designed to minimize solid-liquid interfacial interactions resulting in the anti-wetting behavior illustrated by observing water drops on the surface of the Lotus leaf[2] or on the skin of the European Giant Springtail.[3, 4] These natural surfaces are fascinating examples of superhydrophobic wetting – wherein the surface exhibits an apparent water contact angle greater than 150°, contact angle hysteresis less than 10°, and low roll-off angles. It is now well-established that the superhydrophobic wetting state can be attributed to both chemical composition (typically low surface energy constituents) and geometric parameters (typically hierarchical roughness) of the solid interface. The hierarchical roughness serves to either increase or decrease the contact area of the solid-liquid interface resulting in a so-called apparent contact angle. The liquid either completely conforms to the surface roughness to increase the solid-liquid contact area – an adhesive wetting behavior described as the Wenzel[5] wetting state, or the liquid bridges between surface roughness protrusions creating a composite solid-liquid-air interface – a wetting behavior denoted as the Cassie-Baxter[6] wetting state. Biomimetic design of artificial interfaces targeting the Cassie-Baxter wetting state has led to a better understanding of the underlying wetting mechanisms and

to the exploitation of this anti-wetting phenomenon for a variety of applications including water-resistant textiles, anti-fouling/anti-corrosion/anti-fogging coatings, and oil-water separations.[7-10]

While nature offers many design protocols for superhydrophobic surfaces, the path to superamphiphobicity – surfaces that are anti-wetting (water and oil contact angles >150°; contact angle hysteresis < 10°) in contact with both high and low surface tension liquids – is less defined. Relatively few examples of naturally superamphiphobic materials have been reported with the exception of bacterial (*Bacillus subtilis*) biofilm colonies reported by Aizenberg et al.[11] and springtails (*Orthonychiurus stachianus* and *Tetrodontophora bielanensis*) reported by Werner et al.[4, 12] Engineering superamphiphobic surfaces is more challenging due to the low surface tension of most organic liquids (i.e. hexadecane, λ_{lv} = 27.6 mN/m), which leads to contact angles less than 90° even on inherently hydrophobic, and "oil-resistant" surfaces (i.e. $\theta_{hexadecance}$ = 40° for PTFE).[13] Thus, in addition to the hierarchically rough surface with low surface energy required for superhydrophobicity, superamphiphobicity additionally requires a re-entrant, convex, or overhanging surface curvature to prevent low surface tension liquids from penetrating the surface protrusions and displacing the trapped air cushion, as first described by Tuteja and coworkers.[14, 15] Since the seminal work of Tuteja, numerous approaches have been reported for the fabrication of superoleophobic or superamphiphobic surfaces, including lithography,[14, 16-18] sacrificial templating,[19, 20] replication,[21, 22] electrospinning,[23-25] particle casting,[26] sintering,[27] vapor deposition,[28, 29] chemical etching,[30] sol-gel/aerogels,[31-33] and spray deposition techniques.[34-42] This list is certainly not comprehensive, thus the reader is referred to several recent reviews on

superoleophobic and superamphiphobic materials for more detailed information.[43-46] With the exception of the lithographic approaches, most of the fabrication techniques mentioned rely on the random, fractal nature of the surface protrusions to generate the overhanging surface curvature necessary to support the Cassie wetting state for low surface tension fluids. The spray deposition techniques, in particular, provide a simple and industrially viable approach for the fabrication of coatings with fractal-like surface morphologies over large surface areas. Steele et al.[34] demonstrated one of the earliest examples of spray-deposited superamphiphobic surfaces by atomizing a blend of ZnO nanoparticles with a waterborne perfluoroacrylate polymer emulsion. The nanocomposite coatings reported by Steele displayed high oil contact angles (154°) and low hysteresis (6°). In similar approaches, Srinivasan et al.[36] and Campos et al.[39] spray deposited 1H,1H,2H,2H-heptadecafluorodecyl polyhedral oligomeric silsesquioxane/PMMA and fluoroalkylated-silica/fluoropolymer composite thin films, respectively, with both systems exhibiting good superamphiphobic properties. More recently, Ge et al.[40] reported the spray deposition of 1H, 1H, 2H, 2H-perfluorooctyl functionalized silica with a poly(vinylidene fluoride-hexafluoro-propylene) binder, and demonstrated superamphiphobicity and anti-corrosion properties of the coating on copper substrates. These examples of spray-deposited superamphiphobic coatings clearly illustrate the simplicity in the fabrication approach, but rely only on coalescence of the polymer binder and nanoparticle fillers for film stabilization – an approach that likely leads to subpar thermal and mechanical durability of the delicate surface structure (such data was not reported in the examples cited). Although unexplored specifically in spray-deposited superamphiphobic coatings, crosslinking the polymeric binder has been shown

to improve mechanical durability of superamphiphobic coatings fabricated using other deposition techniques (i.e. spin coating).[47] In previous work, we demonstrated spray-deposition and photopolymerization of hybrid inorganic-organic thiol-ene resins as a simple route to generate superhydrophobic coatings.[48] The spray process provided a hierarchically-structured surface that could be stabilized by crosslinking the resin via thiol-ene photopolymerization. The simplicity of the fabrication process enabled the production of superhydrophobic coatings on a variety of substrates; however, these coatings were highly oleophilic due to the incorporation of siloxane monomer constituents in the coating formulation.[48]

In the present work, we expand the simple approach of spray-deposition and photopolymerization of hybrid inorganic-organic thiol-ene resins to target coatings with superamphiphobic wetting properties. Superamphiphobicity is achieved by introducing a fluorinated multifunctional thiol into the thiol-ene formulation to significantly lower the surface tension of the resin. It is expected that the fluorinated thiol constituents will segregate to the surface of the coating upon spray deposition and that these molecules will be immobilized, or locked into place at the surface of the coating upon photopolymerization. The fluorinated multifunctional thiol is obtained from the product of a thiol-Michael reaction between pentaerythritol tetra(3-mercaptopropionate) (PETMP) and a fluorinated acrylate containing either six or nine fluorinated carbons. The thiol-ene resins are formulated in an organic solvent using 1,3,5-triallyl-1,3,5-triazine-2,4,6 (1H, 3H, 5H) trione as a multifunctional alkene, trimethylsilyl-modified silica nanoparticles for nanoscale roughness, and a combination of the fluorinated and non-fluorinated PETMP as low surface tension components. Spray deposition and

photopolymerization of this formulation results in a hierarchically-structured morphology where the morphology, and ultimately the wetting properties, are dependent on the nanoparticle loading level and the concentration of fluorinated PETMP. In addition to evaluation and discussion of wetting properties using water and hexadecane as probes, the chemical, thermal, and mechanical durability of the composite coatings are discussed.

2.2 Experimental Section

2.2.1 Materials.

All reagents were obtained at the highest purity available and used without further purification unless otherwise specified. 1,3,5-triallyl-1,3,5-triazine-2,4,6 (1H, 3H, 5H) trione (TTT), 2,2-dimethoxy-2-phenylacetophenone (DMPA), and tetrahydrofuran (THF) were obtained from Sigma-Aldrich. Pentaerythritol tetra(3-mercaptopropionate) (PETMP) was obtained from Bruno Bock. Aerosil R972, a trimethylsilyl $-Si(CH_3)_3$ surface functionalization fumed silica with an average primary particle size of 16 nm, was kindly donated as product samples by Evonik Industries. 1H,1H-perfluoro-n-decyl acrylate and 1H,1H-perfluoroheptyl acrylate were purchased from Exfluor Research Corporation. Fluorinated multifunctional thiols were synthesized using a thiol-Michael reaction between PETMP and perfluorinated acrylates following a synthetic procedure established by Shin and coworkers[49] and extended to perfluorinated materials by Goetz et al.[50]

2.2.2 Characterization.

Static and dynamic water contact angle measurements were performed using a Rame-Hart 200-00 Std.-Tilting B. goniometer. Static contact angles were measured using 6 μL water droplets. Dynamic contact angles were obtained by taking 10 measurements/s

for 15 s of an advancing or receding water droplet using a syringe pump to dispense and withdraw water from the droplet on the surface at 0.15 mL/min. The roll-off angle of a 6 μL drop was measured using the tilting feature of the goniometer. Image J Drop Analysis software was used to analyze the droplets and determine static and dynamic contact angle values. Surface free energy of the samples without roughness was obtained using a Rame-Hart tensiometer according to the Fowkes two component model.[51] High-speed video was recorded using a Phantom, version 5.1 (Vision Research, Inc., Wayne, NJ). Scanning electron microscopy (SEM) images were obtained using an FEI Quanta 200 SEM at 25 kV under high vacuum conditions. High-resolution field emission SEM (FE-SEM) images were obtained with a Zeiss Sigma VP FEG-SEM at 10 kV in high vacuum mode. XPS measurements were performed using a Kratos Axis Ultra Spectrometer (Kratos Analytical, Manchester, UK) with a monochromatic Al K X-ray source (1486.6 eV) operating at 150 W under 1.0 × 10-9 Torr. Measurements were performed in hybrid mode using electrostatic and magnetic lenses, and the pass energy of the analyzer was set at 40 eV for high-resolution spectra and 160 eV for survey scans, with energy resolutions of 0.1 eV and 0.5 eV, respectively. Generally, total acquisition times of 180 s and 440 s were used to obtain high resolution and survey spectra, respectively. For a 0° take off angle (angle between sample surface normal and the electron optical axis of the spectrometer), the maximum information depth of the measurements was approximately 8-10 nm.[52] All XPS spectra were recorded using the Kratos Vision II software; data files were translated to VAMAS format and processed using the CasaXPS software package (v. 2.3.12). Binding energies were calibrated with respect to C1s at 284.8 eV. Following application of a Shirley background subtraction, atomic percentages were calculated from

the elemental peak areas present in the survey spectra using the relative sensitivity factors provided by Kratos. High-resolution spectra were fitted using mixtures of Gaussian/Lorentzian peaks after a Shirley background subtraction. The fitting parameters included peak position, full width at half maximum, intensity, and the Guassian fraction. Abrasion resistance of the films was evaluated using a reciprocating abrasion test similar to methods reported in literature.[53] Drop impact testing was carried out according to literature methods. A schematic of the abrasion test and the drop impact test (Figure A1) can be found in the Supporting Information.

2.2.3 Film Preparation.

Thiol-ene resins were prepared by weighing out the desired ratio of fluorinated and non-fluorinated thiol (i.e. F_9PETMP/PETMP), alkene (TTT), and photoinitiator (DMPA) into a glass jar, maintaining a 1:1 stoichiometric ratio of thiol to alkene. The mass ratio of F9PETMP/ PETMP was varied at 0:100, 10:90, 20:80, and 30:70. A specified amount of hydrophobic silica nanoparticles (Aerosil R972 = 0, 10, 20, 30 wt.% relative to resin) was added to the resin mixture and subsequently dispersed in THF (15:1 w/w solvent/resin) by ultrasonication for 30 – 60 min. Glass slides and aluminum Q-panels were used as model substrates. An airbrush with a nozzle diameter of 0.635 mm (Paasch H#3 obtained from McMaster Carr) was connected to a compressed nitrogen source (25 psi) and used to spray coat the thiol-ene resin onto the substrates at a distance of 15 cm and a rate of 2 mL/min. The coated substrate was allowed to sit for 1 min and subsequently cured under a UV flood lamp (16 mW/cm2) for 5 min.

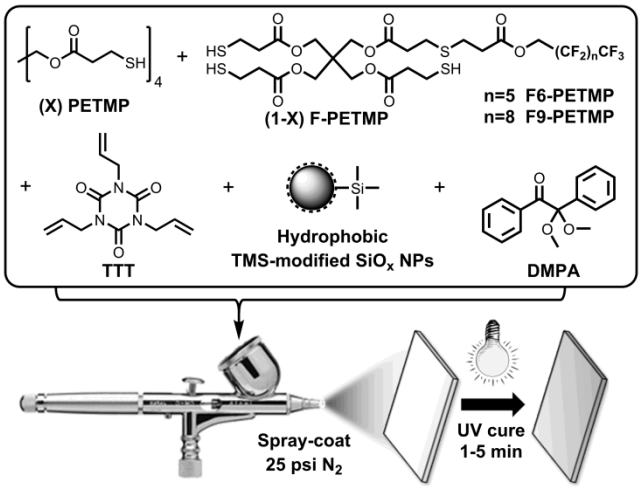

Scheme 2.1 Schematic of the spray deposition and photopolymerization process using hybrid inorganic−organic thiol-ene resins laden with hydrophobic silica nanoparticles.

2.3 Results and Discussion

2.3.1 Resin Formulation and Film Fabrication.

As shown in Scheme 2.1, thiol-ene photopolymer resins were formulated with a photoinitiator (DMPA), a trifunctional alkene (TTT), a mixture of multifunctional thiols (PETMP and F-PETMP), and hydrophobic trimethysilyl-modified silica nanoparticles. TMS-SiO_2 was incorporated at 10%, 20%, and 30% by weight relative to the total weight of the thiol-ene resin. Two perfluorinated chain lengths were investigated as modifiers for PETMP, including 1H,1H-perfluoroheptyl (six fluorinated carbons – F_6PETMP) and 1H,1H-perfluoro-n-decyl (nine fluorinated carbons – F_9PETMP). The fluorinated multifunctional F-PETMP thiols were incorporated to significantly lower the surface energy of the thiol-ene resin – with the 1H,1H-perfluoroheptyl version of interest due to the reduced environmental persistence of perfluorinated materials with shorter chain lengths. F_6PETMP and F_9PETMP were incorporated at 10 wt% and 30 wt% relative to the total weight of the thiol components (i.e. PETMP + F-PETMP), while maintaining a

1:1 molar ratio between total thiol and alkene functional groups. Attempts to use pure F_6PETMP or F_9PETMP as the thiol constituent in the formulation, as well as concentrations of F_6PETMP or F_9PETMP higher than 30 wt% resulted in deteriorated film forming properties. To help simplify the notation for each system, we will represent the various formulations as F_nPETMP(x)/SiO_2(y), where n represents either 6 or 9 fluorinated carbons, and x and y represent the wt% of F_n-PETMP and wt% of TMS-SiO_2, respectively.

To formulate the resins, the TMS-SiO_2 nanoparticles were diluted into THF and dispersed using probe ultrasonication. The remaining resin components were then dissolved into the nanoparticle dispersion, mixed thoroughly, and spray-coated onto glass and aluminum substrates using a simple airbrush device. The spray-coating process atomizes the resin solution into a random distribution of micrometer and submicrometer-sized droplets and directs these droplets towards the substrate with air flow. Adjustment of the spray-coating parameters (i.e. nozzle to substrate distance, sweep speed, nozzle size, air pressure, etc.) enables the deposition of films ranging from a "dry-sprayed" layer to a fully wet layer, where rapid volatilization of the organic solvent from the microparticles prior to or upon deposition results in the formation of a porous, microstructured morphology. The importance of spray-coating parameters on the wetting and wear behavior of superhydrophobic surfaces was recently reported by Yeong et al.[54] In the current work, deposition of films under "dry-spray" conditions resulted in chalky textures, thus such conditions were avoided due to the fragile nature of the resulting morphologies (i.e. surfaces were easily damaged upon handling). The combination of TMS-modified SiO_2 nanoparticles with the microparticles from the spray process endow

the surface with the desired hierarchical, or multi-scale morphology necessary to achieve extreme anti-wetting properties of the coatings. After allowing the solvent to evaporate from the deposited film for 1 min, the films were cured under a UV light in ambient atmosphere via thiol-ene photopolymerization. The photopolymerization process served to crosslink the thiol-ene polymer matrix and stabilize the multi-scale morphology of the film. Upon optimization of the spray-coating process, the parameters associated with the spray deposition were kept constant as described in the experimental section. It is worth noting that the entire film fabrication process (from formulation to photopolymerization) can be completed in under 100 minutes, where the rate limiting step is the ultrasonic dispersion of nanoparticles.

2.3.2 Surface Morphology and Chemical Composition.

To achieve superamphiphobic wetting, surfaces must exhibit both a low interfacial energy and a re-entrant (or overhanging) surface morphology. The surface morphology of the spray-coated and photocured thiol-ene films was investigated using SEM. Figure 2.1a-c and 2.1d-f show a series of low magnification SEM images for F_9PETMP(10) and F_9PETMP(30) containing 10%, 20%, and 30% by weight TMS-SiO_2, respectively. Initial observations indicate that the concentration of F_9PETMP (10% versus 30%) plays a minimal role in altering the film morphology, while morphology is significantly dependent on the TMS-SiO_2 nanoparticle concentration. At 10% TMS-SiO_2 loading, the surface of the films exhibit a course morphology with low porosity on the micrometer scale (Figure 2.1a and 2.1d). This course morphology is likely attributed to the aggregation and coalescence of micrometer-sized droplets formed during the spray deposition process. As the TMS-SiO_2 content is increased, the surface morphology of

films containing 20% (Figure 2.1b and 2e) and 30% (Figure 2.1c and 2f) TMS-SiO_2 transition to a raspberry-like microstructure with high porosity resulting from the random agglomeration and deposition of spherical droplets during spray process. High magnification FE-SEM images of the F_9PETMP(30)/SiO_2(30) film, shown in Figure 2.2a-c, confirm the presence of an agglomerated sphere-like morphology, and further reveal the hierarchical nature of the surface roughness. Figures 2.2b and 3c clearly show the porous structure with sub-100 nm TMS-SiO_2 nanoparticle aggregates superimposed over the

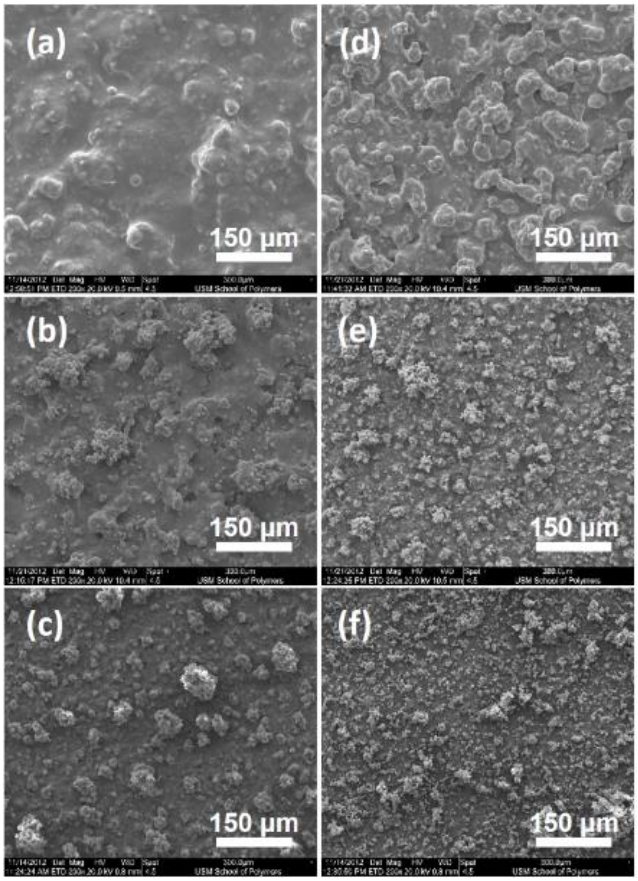

Figure 2.1 SEM micrographs of F_9PETMP(10) and F_9PETMP(30) with various amount nanoparticles.

(a), (d) 10%, (b), (e) 20%, (c), (f) 30% nanoparticles.

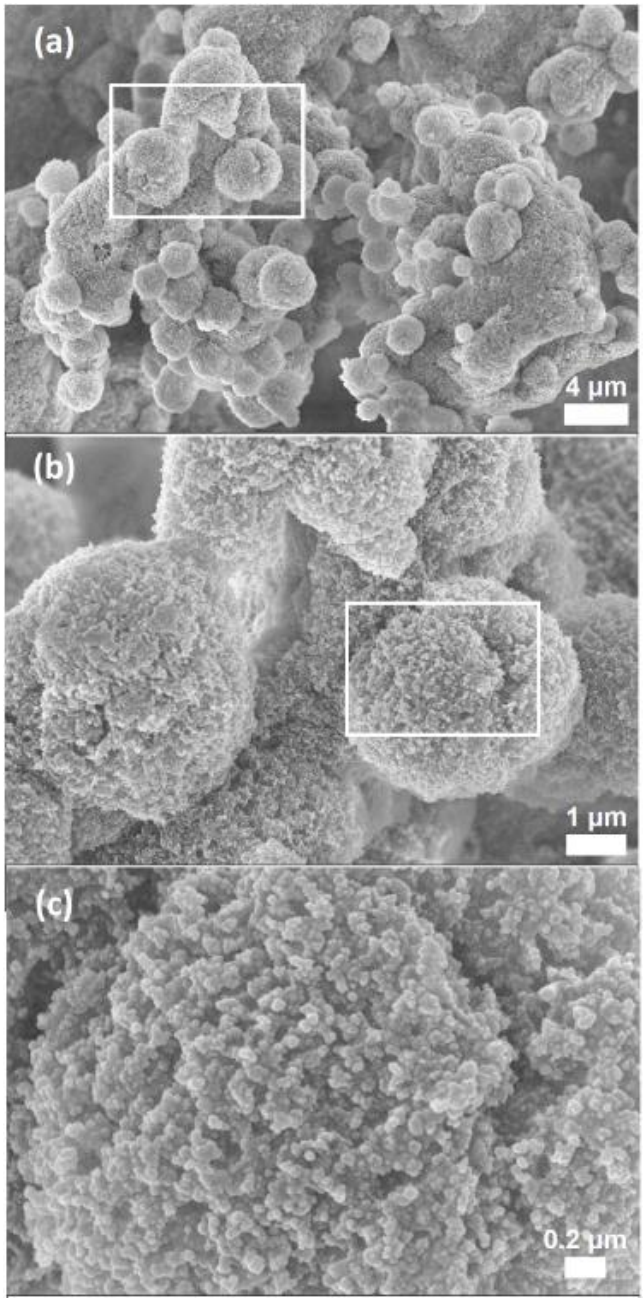

Figure 2.2 High resolution FE-SEM micrographs of F_9PETMP(30)/SiO_2(30).

(a) 2800X, (b) 10000X, and (c) 32000X magnification.

surface of the larger sphere-like microparticles. More importantly, the hierarchical structures create protrusions with overhanging geometries essential for superamphiphobicity.

The observed wetting behavior (discussed *vide infra*) can be related to the chemical composition of the interface for the photocured surfaces. The low surface energy components within our formulation, i.e. F_6PETMP or F_9PETMP, experience a thermodynamic driving force to move toward the solid-air interface in order to minimize the solid-vapor interfacial free energy of the coatings.[55, 56] The presence of solvent at the beginning of the spray deposition process ensures mobility of F-PETMP, which should facilitate surface segregation. X-ray photoelectron spectroscopy was employed to probe the local chemical composition of the surface and the degree of surface segregation of the photocured coating (~8-10 nm probe depth).[52]

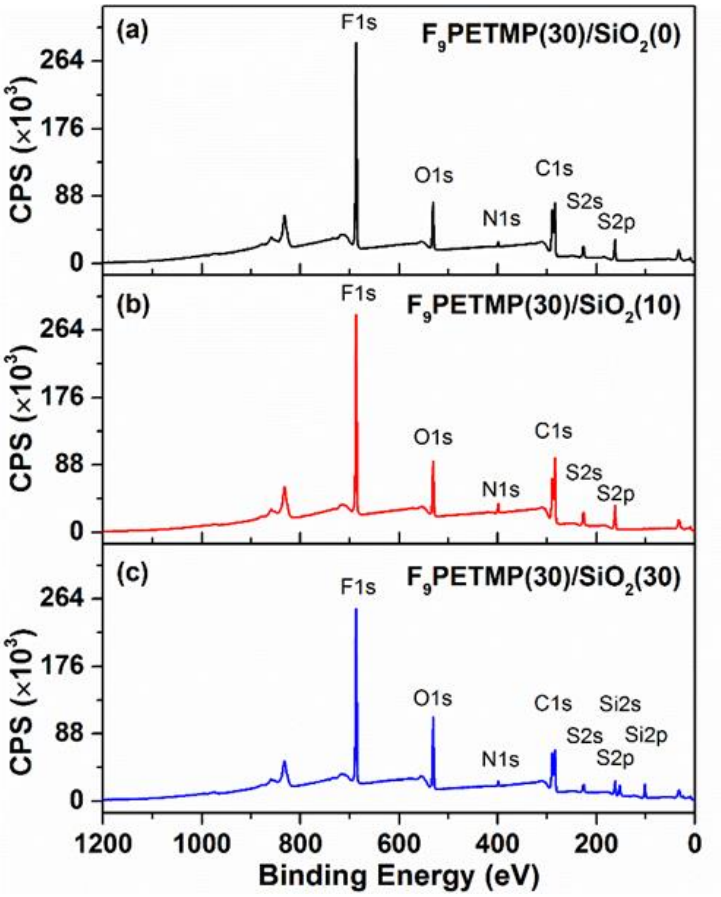

Figure 2.3 XPS survey spectra.

(a) F_9PETMP(30)/SiO_2(0), (b) F_9PETMP(30)/SiO_2(10), and (c) F_9PETMP(30)/SiO_2(30).

Figure 2.3a-c shows the survey spectra for F_9PETMP(30)/SiO_2(0), F_9PETMP(30)/SiO_2(10), and F_9PETMP(30)/SiO_2(30), respectively; whereas the survey spectra for the F_9PETMP(10) series can be found in the supporting information (Figure A2). The spectra for the F_9PETMP(30)/SiO_2(0) and F_9PETMP(30)/SiO_2(10) samples exhibit peaks at 162.8 eV, 284.8 eV, 399.8 eV, 531.8 eV, and 687.8 eV corresponding to the binding energies for the S2p, C1s, N1s, O1s, and F1s, respectively. It is interesting to note that peaks attributable (i.e. Si2p, Si2s) to the TMS-modified SiO_2 nanoparticles are not observed in the survey spectrum for the F_9PETMP(30)/SiO_2(10) sample; however, the Si2p and Si2s peaks at 102.8 eV and 153.9 eV are clearly present in the survey spectrum for the F_9PETMP(30)/SiO_2(30). This observation suggests that the TMS-SiO_2 nanoparticles are predominately covered by thiol-ene resin at low nanoparticle loading levels, and are at least partially exposed at the interface at higher loading levels. Additionally, atomic compositions obtained by XPS were used to quantify the surface segregation of F-PETMP by comparing experimentally observed atomic ratios – specifically the F/C ratio – with atomic ratios calculated from the bulk resin composition. The F/C ratios calculated from the bulk compositions for F_9PETMP(10)/SiO_2(0) and F_9PETMP(30)/SiO_2(0) are 0.028 and 0.091, respectively, as shown in Table 2.1.

Table 2.1

Surface composition of Sprayed F-PETMP-PETMP-TTT Hybrid Inorganic-organic Thiol-ene Films

Sample	F/C Calculated[a]	F/C Observed (XPS)
F_9PETMP(10)/SiO_2(0)	0.028	0.419 ± 0.015
F_9PETMP(10)/SiO_2(10)	--	0.499 ± 0.016
F_9PETMP(10)/SiO_2(30)	--	0.559 ± 0.019
F_9PETMP(30)/SiO_2(0)	0.091	0.521 ± 0.016
F_9PETMP(30)/SiO_2(10)	--	0.479 ± 0.015
F_9PETMP(30)/SiO_2(30)	--	0.579 ± 0.013

[a] F/C ratio calculated according to the bulk composition and stoichiometry of the resin. The same calculation was not possible in the presence of trimethylsilyl-modified silica nanoparticles.

The enhanced F/C ratios obtained from the survey spectra for the F_9PETMP(10)/SiO_2(0) (F/C = 0.419 ± 0.015) and F_9PETMP(30)/SiO_2(0) (F/C = 0.521 ± 0.016) samples confirm the surface enrichment of the low surface energy F_9PETMP component. Generally, slightly higher F/C values were observed with 10 wt% and 30 wt% nanoparticles included in the formulation, which may be attributed to greater mobility of the resin components upon deposition due to the higher solvent content necessary to spray the nanoparticle-laden formulations. However, accounting for the amount of carbon present on the TMS-modified nanoparticles made calculating the comparative bulk atomic composition difficult with TMS-SiO_2 in the formulation, thus, bulk values were not determined for sample containing nanoparticles. Considering both the large surface roughness in our samples and the large difference in kinetic energy between the F1s and C1s photoelectrons that results in a significantly smaller sampling depth for fluorine than carbon, we use the F/C ratios only to show the tendency of F-PETMP to segregate towards the film-air interface.

High-resolution XPS was also employed to provide additional insight into the chemical composition of the film interface. Figures 2.4a-d respectively show the high resolution C1s spectra obtained from the F_9PETMP(10)/SiO_2(0), F_9PETMP(30)/SiO_2(0), F_9PETMP(10)/SiO_2(30), and F_9PETMP(30)/SiO_2(30) surfaces. The spectra were deconvoluted into six component peaks with binding energies characteristic of the molecular units comprising the polymer network, including –C–C/C–H (284.8 eV), –C–N/–C–S (285.7 eV), –C–O/–CH_2CF_2– (286.5 eV), –O–C=O/–O=C–N–C=O (ester/cyclic urea, 288.6 eV), –CF_2 (290.9 eV), and –CF_3 (293.1 eV). F_9PETMP(10)/SiO_2(30) and F_9PETMP(30)/SiO_2(30) surfaces required an additional peak at 283.4 eV corresponding to the C-Si group arising from the presence of TMS-SiO_2 nanoparticles at the interface. Peak fits were summed together when significant overlap of the binding energies for specific molecular structures prevented unequivocal deconvolution (i.e. –C–N/–C–S, –C–O/–CH_2CF_2– and –O–C=O/–O=C–N–C=O). Assignments of these components agree well with those reported for materials with similar molecular constituents.[57] The CF_2/CF_3 peak area ratio varied from 7.52 – 7.58 for surfaces without TMS-SiO_2 nanoparticles to 7.23 – 7.35 for surfaces containing 30 wt. % TMS-SiO_2. In all cases, the CF_2/CF_3 ratio closely resembled the expected ratio of 8 (i.e. –CH_2–$(CF_2)_8$-CF_3), which along with the previously discussed XPS survey data confirms the interface is rich with perfluoro-n-decyl chains. While chain orientation cannot be directly inferred from these XPS experiments, the presence of CF_3 groups is important and is known to play a prominent role in lowering the surface free energy of the films (discussed *vide infra*).[58, 59]

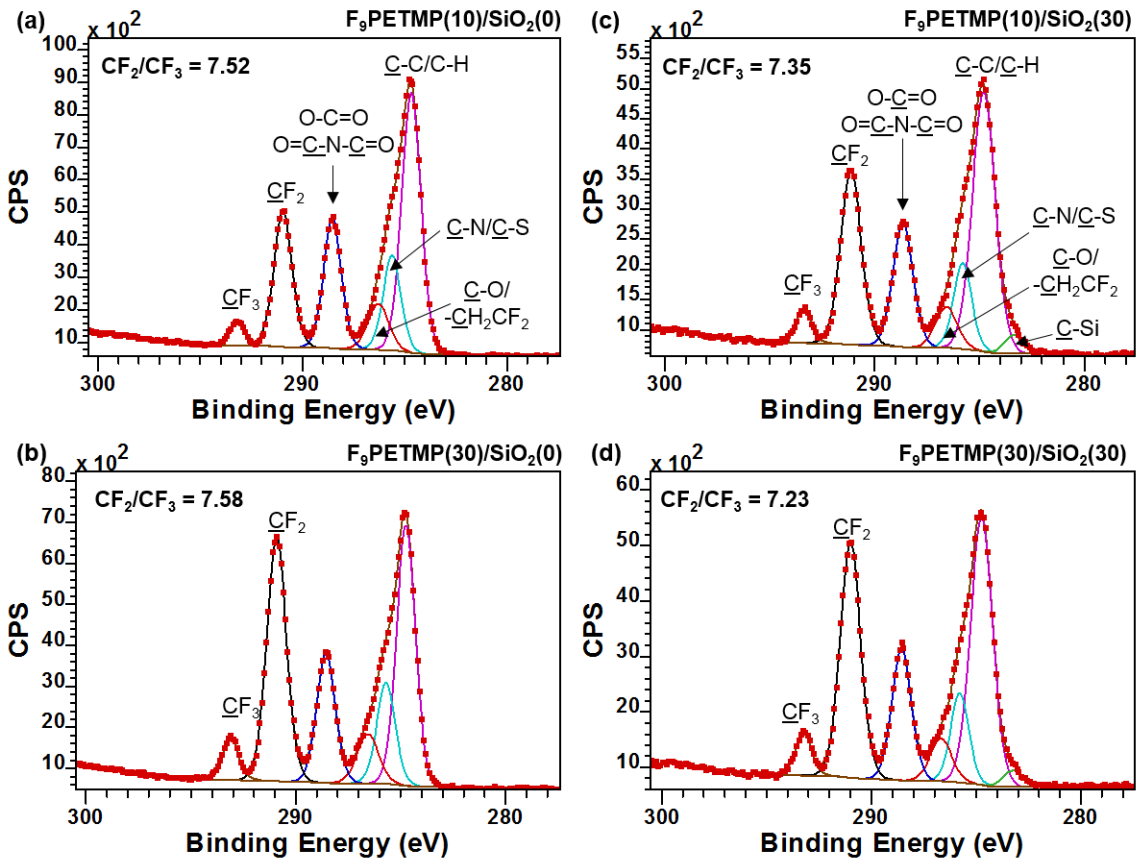

Figure 2.4 High resolution C1s spectra

(a) F_9PETMP(10)/SiO_2(0), (b) F_9PETMP(30)/SiO_2(0), (c) F_9PETMP(10)/SiO_2(30), and (d) F_9PETMP(30)/SiO_2(30) surfaces.

2.3.3 Wetting Behavior.

The wetting properties of the fabricated films were evaluated by measuring the static contact angle (CA), dynamic contact angle, contact angle hysteresis, and roll off angle using both high and low surface tension liquids, including water (γ_{LV} = 72.3 mN/m) and n-hexadecane (γ_{LV} = 27.6 mN/m). Table 2.2 summarizes the wetting behavior of the flat (non-textured) thiol-ene films containing 10% and 30% of either F_6PETMP or F_9PETMP, but without the addition of TMS-SiO_2 nanoparticles. As shown, the static water CA (WCA) increased from 73° for the non-fluorinated PETMP(100)/SiO_2(0) film to 95° and 99° upon incorporation of 10 and 30 wt% F_6PETMP, respectively. Likewise,

the non-fluorinated PETMP-TTT film was completely wetted by hexadecane, but exhibited an oil (hexadecane) contact angle (OCA) of 71° and 73°, respectively, with the addition of 10 and 30 wt% F_6PETMP. As expected, incorporation of F_9PETMP into the resin resulted in films with greater hydrophobicity (WCA, 118°) and oleophobicity (OCA, 81°) due to the longer fluorinated chain length – but showed a minimal dependence on the F_9PETMP concentration. This concentration independent wetting behavior is likely attributed to the saturation of the film interface with 1H,1H-perfluoro-n-decyl functional groups, as XPS showed large enhancements in the F/C ratio for both 10 and 30 wt% F_9PETMP. From these contact angle measurements, the calculated surface energy decreased from 17.6 mN/m for films containing 10 wt% F_6PETMP to 9.6 mN/m for films containing 10 or 30 wt% F_9PETMP. The wetting properties and surface energy values reported herein for films containing F_6PETMP and F_9PETMP are characteristic of films containing $–CF_3$ groups at the interface (as previously shown by XPS), and compare well with values reported in the literature for other thin films comprising similar perfluoro-n-alkyl acrylate derivatives.[55, 59, 60]

Table 2.2

Wetting Properties of smooth F-PETMP-PETMP-TTT films without TMS-SiO2 nanoparticles

Sample	θ_{water} (°)	θ_{oil} (°)[a]	Surface Energy (mN/m)[b]
PETMP(100)/SiO_2(0)	72.6 ± 0.9	0	-
F_6PETMP(10)/SiO_2(0)	95.4 ± 1.5	71.3 ± 1.1	17.6 ± 0.65
F_6PETMP(30)/SiO_2(0)	99.3 ± 1.2	73.3 ± 3.2	15.7 ± 0.72
F_9PETMP(10)/SiO_2(0)	118.1 ± 0.8	81.5 ± 0.6	9.61 ± 0.16
F_9PETMP(30)/SiO_2(0)	118.8 ± 0.3	81.3 ± 0.1	9.60 ± 0.03

[a] hexadecane; [b] calculated according to the Fowkes two component model

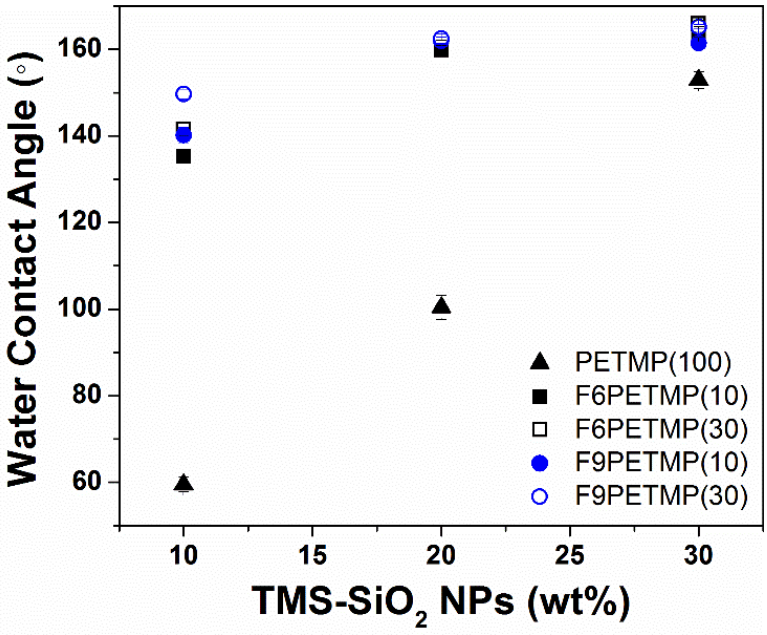

Figure 2.5 Variation of the static water contact angle as a function of TMS-SiO_2 nanoparticle loading level.

Sample formulated with (▲) PETMP(100), (■) F_6PETMP(10), (□) F_6PETMP(30), (●) F_9PETMP(10), and (○) F_9PETMP(30).

With an understanding of the wetting properties associated with F_nPETMP thiol-ene resins in non-textured films, we next investigated the wetting behavior of these resins containing TMS-SiO_2 nanoparticles. Figure 2.5 shows the relationship between the static WCA and TMS-SiO_2 nanoparticle loading level for both F_6PETMP and F_9PETMP resin systems following spray deposition and photopolymerization. For films containing 10% TMS-SiO_2, the static WCA increased based on the fluorinated chain length (F_6 vs. F_9) and concentration, with 10 wt% F_6PETMP exhibiting the lowest WCA of 135° and 30 wt% F_9PETMP exhibiting the highest WCA of 150°. Films containing 10% TMS-SiO_2 exhibited a Wenzel-type wetting behavior evident from the strong pinning of the water droplet during receding contact angle measurements and adhesion of the droplet during roll-off measurements. Films containing 20% and 30% TMS-SiO_2 all exhibit WCAs in the superhydrophobic regime (160° - 165°) with minimal dependence on the fluorinated

PETMP chain length or concentration, as shown in Figure 2.4. These same films, as summarized in Table 2.3, also show relatively low contact angle hysteresis values (< 7°) and extremely low roll-off angles (< 8°) characteristic of a Cassie-Baxter wetting state. The F_9PETMP(30)/SiO_2(30) film provided the highest superhydrophobic wetting performance with a water contact angle of 165°, 1.2° contact angle hysteresis, and a 1° roll-off angle.

Table 2.3

Water Contact Angle Data for Sprayed F-PETMP-PETMP-TTT Hybrid Inorganic-organic Thiol-ene Thin Films

SiO_2 (wt%)	θ_{Adv} (°)	θ_{Static} (°)	θ_{Rec} (°)	θ_{Hys} (°)	θ_{Roll} (°)
PETMP(100)/SiO_2(y)					
10%	67.7 ± 1.6	59.5 ± 1.7	-		-
20%	108.2 ± 2.2	100.4 ± 2.8	-	-	-
30%	154.8 ± 1.3	152.9 ± 1.9	150.3 ± 2.4	4.5	8 ± 2
F_6PETMP(10)/SiO_2(y)					
10%	144.7 ± 0.8	135.3 ± 0.5	-	-	-
20%	163.9 ± 0.9	159.9 ± 0.9	156.7 ± 0.8	7.2	8 ± 1
30%	164.69 ± 0.4	163.5 ± 0.6	159.3 ± 2.4	5.39	2 ± 1
F_6PETMP(30)/SiO_2(y)					
10%	149.6 ± 0.9	141.5 ± 1.6	-	-	-
20%	164.4 ± 0.29	161.5 ± 0.59	159.0 ± 0.8	5.4	6 ± 1
30%	167.3±0.3	165.9 ± 0.7	162.4 ± 0.5	4.9	1 ± 1
F_9PETMP(10)/SiO_2(y)					
10%	151.7±1.2	140.2 ± 1.8	-	-	-
20%	162.9 ± 0.6	162.0 ± 0.8	159.3 ± 1.2	4.1	3 ± 1
30%	162.3 ± 1.4	161.4 ± 1.3	160.7 ± 0.7	1.6	1 ± 1
F_9PETMP(30)/SiO_2(y)					
10%	154.5 ± 1.7	149.7 ± 1.1	-	-	-
20%	163.0 ± 1.0	162.5 ± 1.1	160.1 ± 0.8	2.9	2 ± 1
30%	166.0 ± 1.0	165.2 ± 0.5	164.8 ± 0.8	1.2	1 ± 1

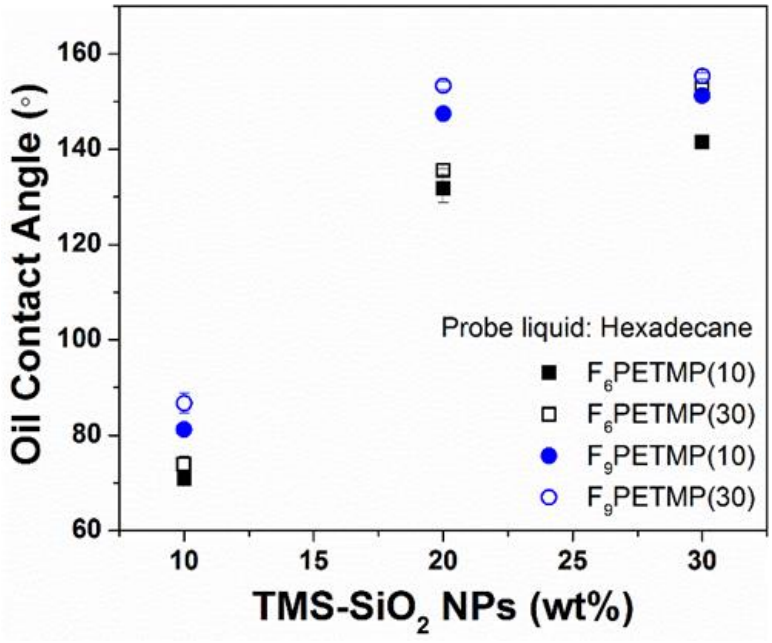

Figure 2.6 Variation of the static oil contact angle as a function of TMS-SiO_2 nanoparticle loading level

Samples formulated with F_6PETMP(10) (■), F_6PETMP(30) (□), F_9PETMP(10) (●), and F_9PETMP(30) (○).

The oleophobic properties of the thiol-ene films, summarized in Table 2.4, were evaluated using hexadecane (surface tension 27.6 mN/m) as a probe liquid. Figure 2.6 shows the relationship between the static OCA and the TMS-SiO_2 nanoparticle loading level for each of the F_6PETMP and F_9PETMP resin systems. As shown, all films containing 10% TMS-SiO_2 remain oleophilic (oil CA < 90°) regardless of the fluorinated chain length or concentration of the F-PETMP. The oleophilic nature of these surfaces can be attributed to the course roughness observed by SEM, and therefore lack of the hierarchical surface morphology (see SEM images in Fig. 2a and 2d) necessary to increase the contact angle with low surface tension liquids. At 20% TMS-SiO_2, we observed a sharp increase in the OCA for each film composition; however, only the F_9PETMP(30)/SiO_2(20) sample achieved the mark of superoleophobicity (oil CA 153°) albeit with a large hysteresis value (15°). Increasing the TMS-SiO_2 nanoparticle

concentration to 30% enables the observation of superoleophobicity for a broader range of fluorinated chain lengths and concentrations including the F_6PETMP(30)/SiO_2(30), F_9PETMP(20)/SiO_2(30), and F_9PETMP(30)/SiO_2(30) film compositions. These three film compositions also exhibit relatively low hysteresis and roll-off angles with hexadecane, with F_9PETMP(30)/SiO_2(30) showing the highest superoleophobicity (OCA 155°, θ_{Hys} 9.5°, and θ_{Roll} 4°). Referring back to Figure 2.2, we can relate the hierarchically-structured agglomerates of sphere-like particles to the "re-entrant" curvature or "overhanging" structure often cited in the literature as a critical requirement for superoleophobicity.[14, 44] The combination of 30% TMS-SiO_2 and spray-coating process provides this type of overhanging, random structure, while sufficient fluorinated F_nPETMP concentrations provide a low surface energy material at the film interface. The observed trends in oleophobic wetting properties of our thiol-ene films highlight the more stringent interplay between intrinsic surface energy and surface structure necessary to achieve anti-wetting with low surface tension liquids.

Table 2.4

Oil Contact Angle Data for Sprayed F-PETMP-PETMP-TTT Hybrid Inorganic-organic Thiol-ene Thin Films

SiO_2 (wt%)	θ_{Adv} (°)	θ_{Static} (°)	θ_{Rec} (°)	θ_{Hys} (°)	θ_{Roll} (°)
PETMP(100)/SiO_2(y)					
10%	-	0	-		-
20%	-	0	-	-	-
30%	-	0	-	-	-
F_6PETMP(10)/SiO_2(y)					
10%	79.4 ± 2.0	70.93 ± 0.8	-	-	-
20%	146.9 ± 0.7	131.74 ± 2.92	89.7 ± 0.8	57.2	-
30%	151.0 ± 1.1	141.48±1.33	121.3 ± 2.4	29.7	-
F_6PETMP(30)/SiO_2(y)					
10%	80.6 ± 1.9	73.88 ± 1.6	-	-	-
20%	141.9 ± 0.9	135.39 ± 0.5	96.0 ± 0.8	45.9	-
30%	155.6 ± 1.4	153.07 ± 0.67	141.9 ± 0.9	13.7	7 ± 1
F_9PETMP(10)/SiO_2(y)					
10%	84.2 ± 0.9	81.2 ± 0.7	41.7 ± 1.8	42.5	-
20%	156.9 ± 0.6	147.4 ± 0.8	141.8 ± 0.7	15.1	-
30%	156.7 ± 1.1	151.2 ± 1.3	143.3 ± 1.7	13.4	-
F_9PETMP(30)/SiO_2(y)					
10%	87.8 ± 0.7	86.7 ± 2.1	42.1 ± 1.9	45.7	-
20%	159.1 ± 0.7	153.3 ± 0.9	144.1 ± 0.8	15	7.5 ± 1
30%	159.6 ± 0.8	155.3 ± 0.7	150.1 ± 1.3	9.5	4 ± 0.5

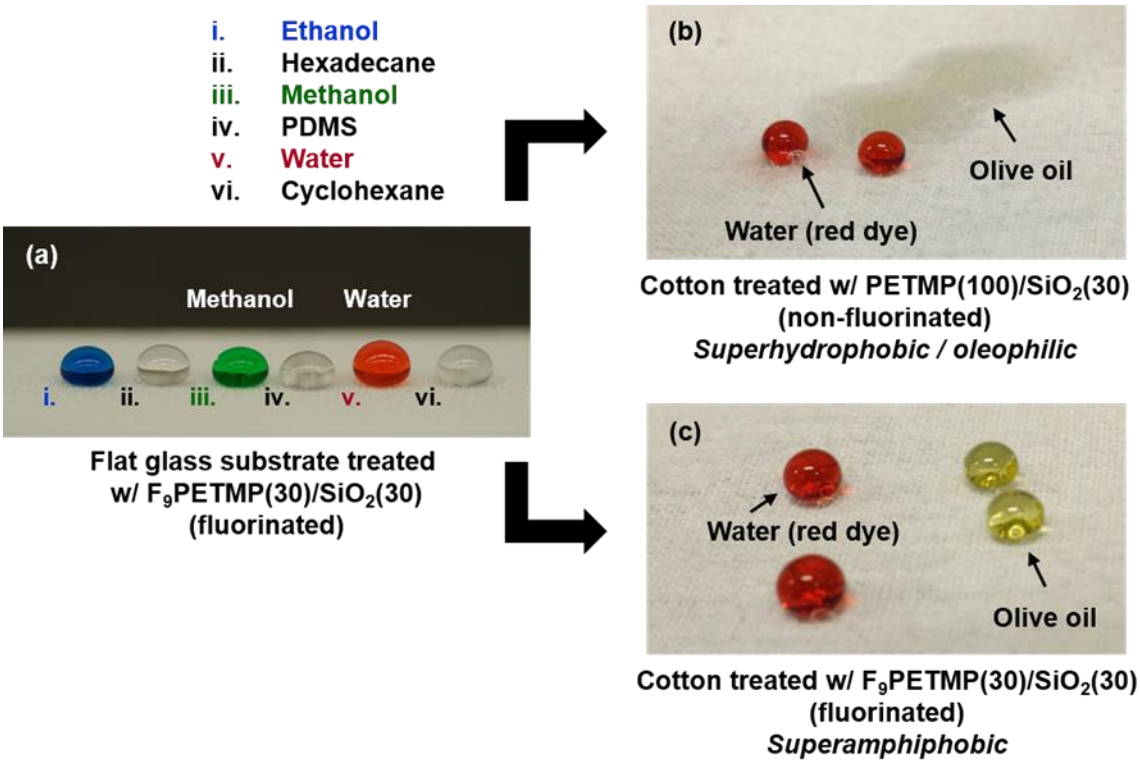

Figure 2.7 Photograph of different liquid droplets sitting on the surface.

(a) Photograph of (left-right) ethanol (γ_{LV} = 22.1 mN/m), hexadecane (γLV = 27.6 mN/m), methanol (γLV = 22.7 mN/m), PDMS (γLV = 19 mN/m), water (γLV = 72.3 mN/m), and cyclohexane (γLV = 24.9 mN/m) sitting on the surface of a F9PETMP(30)/SiO2(30) sample. Photograph of water and olive oil (32.0 mN/m) on a cotton textile treated with a (b) non-fluorinated PETMP(100)/SiO2(30) and (c) F9PETMP(30)/SiO2(30).

Figure 2.7a shows a photograph of several droplets sitting on the surface of a F_9PETMP(30)/SiO_2(30) sample, including ethanol (γ_{LV} = 22.1 mN/m), hexadecane (γ_{LV} = 27.6 mN/m), methanol (γ_{LV} = 22.7 mN/m), PDMS (γ_{LV} = 19 mN/m), water (γ_{LV} = 72.3 mN/m), and cyclohexane (γ_{LV} = 24.9 mN/m). For each liquid, the F_9PETMP(30)/SiO_2(30) surface showed a robust anti-wetting interaction. The dynamic anti-wetting behavior of the F_9PETMP(30)/SiO_2(30) coating with hexadecane and water dropped onto the surface can be viewed in videos provided in the Supporting Information. Figures 2.7b and 2.7c show samples of cotton textile treated with

PETMP(100)/SiO_2(30) (i.e. non-fluorinated) and F_9PETMP(30)/SiO_2(30), respectively. The non-fluorinated PETMP(100)/SiO_2(30) textile shows superhydrophobic wetting as evidenced by the red-dyed water droplet sitting on the surface, but exhibits an oleophilic wetting in contact with olive oil (γ_{LV} = 32.0 mN/m). Conversely, the cotton textile treated with F_9PETMP(30)/SiO_2(30) exhibits superamphiphobicity towards water and olive oil illustrating the important role F_9PETMP plays in the formulation.

2.3.4 Mechanical, Chemical, and Thermals Durability.

Widespread implementation of anti-wetting coatings in everyday applications (i.e. sporting equipment) and in advanced technological applications is arguably limited by issues associated with coating durability. The porous and fractal-like morphologies that give rise to unique wetting phenomena also give rise to mechanical fragility of the surface in response to abrasion. A number of excellent approaches have been reported that target improvements in mechanical damage and deformation (i.e. abrasion, peeling, stretching, etc.),[42, 61-65] temperature stability,[66] and solvent resistance[67] of superhydrophobic surfaces, with fewer examples of mechanically robust superamphiphobic surfaces.[15, 19, 24, 32, 33, 47] Maintaining an anti-wetting state with low surface tension liquids following mechanical abrasion is challenging due to the more stringent requirements for overhanging surface morphology in the superamphiphobic regime. In the current work, the mechanical robustness of the fabricated films was evaluated using a simple, lab-built reciprocating abrasion test. The film to be abraded was placed face up in contact with 2000 grit sandpaper. A loading pressure of 254 N/m^2 was applied and the loaded sandpaper was dragged across the sample in a reciprocating motion at a constant speed of 3.8 mm/s. The changes in water and oil contact angle as a

function of the number of abrasion cycles (up to 350 cycles) for F_9PETMP(30)/SiO_2(30) films are shown in Figure 2.8a. As shown, the WCA decreases slightly with increasing number of abrasion cycles, but remains above 150°, and therefore superhydrophobic,

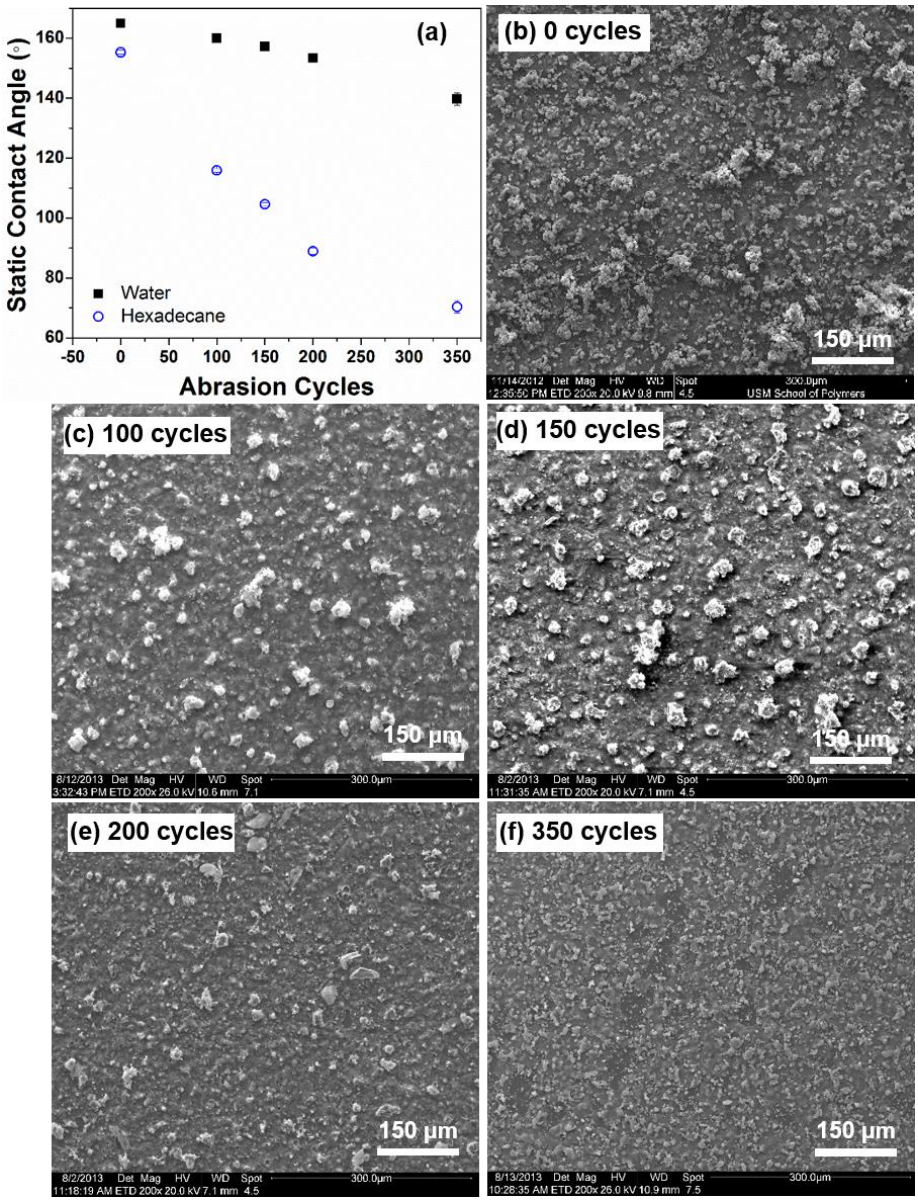

Figure 2.8 (a) Static water and oil contact angles and SEM images for F_9PETMP(30)/SiO_2(30) as a function of abrasion cycle.

(a) Static water and oil (hexadecane) contact angles for F_9PETMP(30)/SiO_2(30) as a function of abrasion cycle. SEM images of the F_9PETMP(30)/SiO_2(30) surface following (b) 0, (c) 100, (d) 150, (e) 200, and (f) 350 abrasion cycles.

after 200 abrasion cycles. The roll off angle increased from 1±1° before abrasion to 14±2° after 200 abrasion cycles, indicating the retention of good anti-wetting properties toward water. After 350 abrasion cycles, the WCA dropped below 150° and the resulting surface exhibited an adhesive wetting behavior (i.e. the water droplet adhered to the surface even at 180° tilt). The OCA using hexadecane, on the contrary, decreased precipitously with increasing number of abrasion cycles. After 100 abrasion cycles, the OCA decreased from 155° to 116° and further decreased to 70° after 350 cycles. SEM analysis was used to provide greater insight into changes in surface morphology of the abraded surfaces, and consequently the observed changes in wetting properties. Figures 2.8b-f show representative SEM images of the F_9PETMP(30)/SiO_2(30) films following 0, 100, 150, 200, and 350 abrasion cycles. The SEM images indicate that the initial damage to the surface occurs by removal of the fine, raspberry-like microstructure present in the as-fabricated film (Figure 2.8f) revealing a more course microstructure with large agglomerates after 100-150 abrasion cycles. 200 abrasion cycles results in the removal of most of the large agglomerates. Nonetheless, the abraded surface with 200 abrasion cycles retains sufficient hierarchical structure by exposing nanoparticles beneath the defects (see SEM images, Figure A3) and is still capable of supporting a superhydrophobic wetting state. At 350 abrasion cycles, large defects are observed in the thiol-ene resin that possibly expose the substrate surface resulting in a WCA below 150° and an adhesive wetting behavior as previously described. Maintaining a superoleophobic wetting state upon multiple abrasion cycles is more challenging due to the low surface tension of the hexadecane probe liquid and a more critical dependence on the re-entrant curvature of the surface morphology. In the present work, we postulate that

the rapid decrease in the OCA upon abrasion can be attributed to damage to the hierarchical, corpuscular morphology and the removal of the surface-enriched fluorinated region of the thiol-ene resin – two factors that work synergistically to yield the oil wetting behavior observed in Figure 2.8a.

The durability of the thiol-ene superamphiphobic surfaces towards long-term impact of water droplets was evaluated by water droplet impact measurements – an evaluation that can mimic exposure to raindrop impacts commonly encountered in outdoor coatings applications. Penetration of the hierarchical protrusions on the superamphiphobic films is expected during the drop-impact event, and the occurrence increases with drop height due to the high instantaneous pressure exerted on the surface.[68] Thus, resistance to drop penetration can provide a measure of robustness for superhydrophobic and superamphiphobic surface. The drop impact measurement was conducted according to a previously reported method.[19] The details of the setup are described in the experimental section and illustrated in Figure A1. Water drops were repeatedly impinged on the surface of the films from a height of 2.5 cm and 20 cm. For drops released from h = 2.5 cm (impact velocity of 0.7 m/s), the F_9PETMP(30)/SiO_2(30) films did show any sign of water drop penetration even after extended testing (we stopped counting after 7600 impact events) which indicates a robust superhydrophobic wetting state. For drops released from h = 20 cm (impact velocity of 1.98 m/s), drop penetration and adhesion to film was observed after 4160 drop impact events, coating superhydrophobic properties degrade.

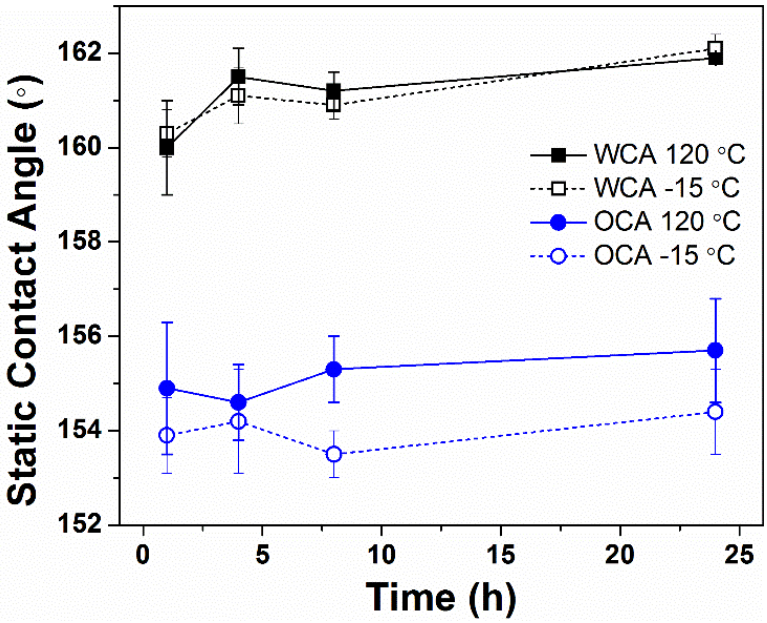

Figure 2.9 Static water and oil contact angles versus exposure time at -15 °C and 120 °C for the F_9PETMP(30)/SiO_2(30) surface.

The stability of the crosslinked thiol-ene coatings and of the associated superamphiphobic wetting behavior was further assessed by exposure of the samples to a variety of environmental conditions, including variations in temperature and pH. F_9PETMP(30)/SiO_2(30) samples were exposed to 120 °C in an air circulation oven to evaluate the elevated temperature stability of the films. As shown in Figure 2.9, the static water and oil (hexadecane) contact angles were fairly constant over a 24 h exposure period at 120 °C illustrating the thermal stability of the microstructure – stability that can be attributed to the highly crosslinked thiol-ene polymer matrix resulting from photopolymerization. Likewise, the F_9PETMP(30)/SiO_2(30) samples were exposed to subfreezing temperatures (-15 °C), and again, the static water and oil contact angles showed minimal changes over a 24 h exposure period. The chemical stability of the F_9PETMP(30)/SiO_2(30) films was evaluated by complete submersion of the samples into ambient temperature aq. H_2SO_4 (pH 2) and aq. KOH (pH 12) solutions for 24 h. As

shown in Figure 2.10, the static water contact angles remained above 160° after 24 h in acid or base, while the oil contact angles remained above 155° under the same conditions.

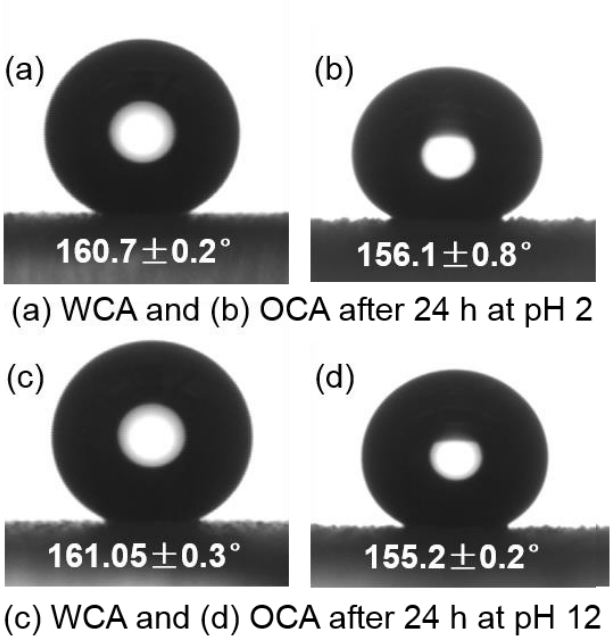

Figure 2.10 Static water and oil contact angles after chemical exposure.

(a) Static water and (b) oil contact angles for F_9PETMP(30)/SiO_2(30) after immersion in aqueous H_2SO_4 (pH 2) for 24 h. (c) Static water and (d) oil contact angles for F_9PETMP(30)/SiO_2(30) after immersion in aqueous KOH (pH 12) for 24 h.

2.4 Conclusions

In this paper, we have demonstrated a simple, fast, and scalable approach to fabricate superamphiphobic coatings via spray-deposition and UV photopolymerization of hydrophobic nanoparticle-laden thiol-ene resins containing a fluorinated multifunctional thiol. Atomization of the nanoparticle-containing resin resulted in the deposition of films with a highly porous, corpuscular morphology exhibiting both micro- and nanometer-scale roughness. Surface segregation of the fluorinated thiol provided an interface with sufficiently low surface energy that, when combined with the hierarchically-rough morphology, resulted in coatings with water and oil contact angles

above 150° and contact angle hysteresis values below 10° for the best performing formulations. The facile nature of the spray deposition and photopolymerization process enables the preparation of superamphiphobic coatings on a variety of substrates, including textiles, in a rapid and scalable manner. Photopolymerization of the thiol-ene matrix provided superamphiphobic coatings with robust anti-wetting behavior following exposure to acidic (pH 2) and basic (pH 12) solutions, and after extended exposure to subfreezing (-15 °C) and elevated temperatures (120 °C). The F_9PETMP(30)/SiO_2(30) coatings displayed a robust response in terms of maintaining superhydrophobicity following multiple mechanical abrasion cycles; however, the superoleophobic wetting properties degraded rather quickly following mechanical damage to the surface. The mechanical durability of the delicate surface structure necessary to maintain superamphiphobicity continues to be a challenge and a potential barrier for broader implementation of anti-wetting technologies. Current and ongoing efforts in our lab continue to address these challenges using simple and scalable fabrication approaches.

2.5 References

1. Butt, H.-J.; Graf, K.; Kappl, *Physics and Chemistry of Interfaces*. 2nd ed.; Wiley-VCH Verlag GmbH & Co.: Weinheim, 2006.
2. Barthlott, W.; Neinhuis, C., Purity of the sacred lotus, or escape from contamination in biological surfaces. *Planta* **1997,** *202*, 1-8.
3. Hensel, R.; Helbig, R.; Aland, S.; Voigt, A.; Neinhuis, C.; Werner, C., Tunable nano-replication to explore the omniphobic characteristics of springtail skin. *NPG Asia Mater.* **2013,** *5*, e37.
4. Helbig, R.; Nickerl, J.; Neinhuis, C.; Werner, C., Smart skin patterns protect springtails. *PLoS ONE* **2011,** *6*, e25105.
5. Wenzel, R. N., Resistance of solid surfaces to wetting by water. *Ind. Eng. Chem.* **1936,** *28*, 988-994.
6. Cassie, A. B. D.; Baxter, S., Wettability of porous surfaces. *Trans. Faraday Soc.* **1944,** *40*, 546-551.
7. Feng, X.; Jiang, L., Design and creation of superwetting/antiwetting surfaces. *Adv. Mater.* **2006,** *18*, 3063-3078.
8. Li, X.-M.; Reinhoudt, D.; Crego-Calama, M., What do we need for a superhydrophobic surface? A review on the recent progress in the preparation of superhydrophobic surfaces. *Chem. Soc. Rev.* **2007,** *36*, 1350-1368.
9. Roach, P.; Shirtcliffe, N. J.; Newton, M. I., Progress in superhydrophobic surface development. *Soft Matter* **2008,** *4*, 224-240.
10. Sun, T. L.; Feng, L.; Gao, X. F.; Jiang, L., Bioinspired surfaces with special wettability. *Acc. Chem. Res.* **2005,** *38*, 644-652.
11. Epstein, A. K.; Pokroy, B.; Seminara, A.; Aizenberg, J., Bacterial biofilm shows persistent resistance to liquid wetting and gas penetration. *Proc. Natl. Acad. Sci.* **2010**.
12. Hensel, R.; Helbig, R.; Aland, S.; Braun, H.-G.; Voigt, A.; Neinhuis, C.; Werner, C., Wetting Resistance at Its Topographical Limit: The Benefit of Mushroom and Serif T Structures. *Langmuir* **2013,** *29*, 1100-1112.
13. Bellanger, H.; Darmanin, T.; Taffin de Givenchy, E.; Guittard, F., Chemical and Physical Pathways for the Preparation of Superoleophobic Surfaces and Related Wetting Theories. *Chem. Rev.* **2014,** *114*, 2694-2716.
14. Tuteja, A.; Choi, W.; Ma, M.; Mabry, J. M.; Mazzella, S. A.; Rutledge, G. C.; McKinley, G. H.; Cohen, R. E., Designing Superoleophobic Surfaces. *Science* **2007,** *318*, 1618-1622.
15. Tuteja, A.; Choi, W.; Mabry, J. M.; McKinley, G. H.; Cohen, R. E., Robust omniphobic surfaces. *Proc. Natl. Acad. Sci.* **2008,** *105*, 18200-18205.
16. Ahuja, A.; Taylor, J. A.; Lifton, V.; Sidorenko, A. A.; Salamon, T. R.; Lobaton, E. J.; Kolodner, P.; Krupenkin, T. N., Nanonails: A Simple Geometrical Approach to Electrically Tunable Superlyophobic Surfaces. *Langmuir* **2007,** *24*, 9-14.
17. Almeida, R.; Kwon, J. W., Virtual Walls Based on Oil-Repellent Surfaces for Low-Surface-Tension Liquids. *Langmuir* **2013,** *29*, 994-998.
18. Zhao, H.; Law, K.-Y.; Sambhy, V., Fabrication, Surface Properties, and Origin of Superoleophobicity for a Model Textured Surface. *Langmuir* **2011,** *27*, 5927-5935.
19. Deng, X.; Mammen, L.; Butt, H.-J.; Vollmer, D., Candle Soot as a Template for a Transparent Robust Superamphiphobic Coating. *Science* **2012,** *335*, 67-70.
20. Paven, M.; Papadopoulos, P.; Mammen, L.; Deng, X.; Sachdev, H.; Vollmer, D.; Butt, H.-J., Optimization of superamphiphobic layers based on candle soot. *Pure Appl. Chem.* **2014,** *86*, 87-96.

21. Liu, X.; Wu, W.; Wang, X.; Luo, Z.; Liang, Y.; Zhou, F., A replication strategy for complex micro/nanostructures with superhydrophobicity and superoleophobicity and high contrast adhesion. *Soft Matter* **2009,** *5*, 3097-3105.
22. Ghosh, N.; Bajoria, A.; Vaidya, A. A., Surface Chemical Modification of Poly(dimethylsiloxane)-Based Biomimetic Materials: Oil-Repellent Surfaces. *ACS Appl. Mater. Interfaces* **2009,** *1*, 2636-2644.
23. Ganesh, V. A.; Dinachali, S. S.; Raut, H. K.; Walsh, T. M.; Nair, A. S.; Ramakrishna, S., Electrospun SiO2 nanofibers as a template to fabricate a robust and transparent superamphiphobic coating. *RSC Adv.* **2013,** *3*, 3819-3824.
24. Ganesh, V. A.; Dinachali, S. S.; Nair, A. S.; Ramakrishna, S., Robust Superamphiphobic Film from Electrospun TiO2 Nanostructures. *ACS Appl. Mater. Interfaces* **2013,** *5*, 1527-1532.
25. Wang, J.; Raza, A.; Si, Y.; Cui, L.; Ge, J.; Ding, B.; Yu, J., Synthesis of superamphiphobic breathable membranes utilizing SiO2 nanoparticles decorated fluorinated polyurethane nanofibers. *Nanoscale* **2012,** *4*, 7549-7556.
26. Jiang, W.; Grozea, C. M.; Shi, Z.; Liu, G., Fluorinated Raspberry-like Polymer Particles for Superamphiphobic Coatings. *ACS Appl. Mater. Interfaces* **2014,** *6*, 2629-2638.
27. He, Z.; Ma, M.; Lan, X.; Chen, F.; Wang, K.; Deng, H.; Zhang, Q.; Fu, Q., Fabrication of a transparent superamphiphobic coating with improved stability. *Soft Matter* **2011,** *7*, 6435-6443.
28. Wang, H.; Xue, Y.; Lin, T., One-step vapour phase formation of patternable, electrically conductive, superamphiphobic coatings on fibrous materials. *Soft Matter* **2011,** *7*, 8158-8161.
29. Wang, H.; Zhou, H.; Gestos, A.; Fang, J.; Niu, H.; Ding, J.; Lin, T., Robust, electro-conductive, self-healing superamphiphobic fabric prepared by one-step vapour-phase polymerisation of poly(3,4-ethylenedioxythiophene) in the presence of fluorinated decyl polyhedral oligomeric silsesquioxane and fluorinated alkyl silane. *Soft Matter* **2013,** *9*, 277-282.
30. Yang, J.; Zhang, Z.; Xu, X.; Men, X.; Zhu, X.; Zhou, X., Superoleophobic textured aluminum surfaces. *New J. Chem.* **2011,** *35*, 2422-2426.
31. Valipour Motlagh, N.; Birjandi, F. C.; Sargolzaei, J.; Shahtahmassebi, N., Durable, superhydrophobic, superoleophobic and corrosion resistant coating on the stainless steel surface using a scalable method. *Appl. Surf. Sci.* **2013,** *283*, 636-647.
32. Jin, H.; Tian, X.; Ikkala, O.; Ras, R. H. A., Preservation of Superhydrophobic and Superoleophobic Properties upon Wear Damage. *ACS Appl. Mater. Interfaces* **2013,** *5*, 485-488.
33. Zhou, H.; Wang, H.; Niu, H.; Gestos, A.; Lin, T., Robust, Self-Healing Superamphiphobic Fabrics Prepared by Two-Step Coating of Fluoro-Containing Polymer, Fluoroalkyl Silane, and Modified Silica Nanoparticles. *Adv. Func. Mater.* **2013,** *23*, 1664-1670.
34. Steele, A.; Bayer, I.; Loth, E., Inherently Superoleophobic Nanocomposite Coatings by Spray Atomization. *Nano Letters* **2008,** *9*, 501-505.
35. Das, A.; Schutzius, T. M.; Bayer, I. S.; Megaridis, C. M., Superoleophobic and conductive carbon nanofiber/fluoropolymer composite films. *Carbon* **2012,** *50*, 1346-1354.
36. Srinivasan, S.; Chhatre, S. S.; Mabry, J. M.; Cohen, R. E.; McKinley, G. H., Solution spraying of poly(methyl methacrylate) blends to fabricate microtextured, superoleophobic surfaces. *Polymer* **2011,** *52*, 3209-3218.
37. Yang, J.; Zhang, Z.; Men, X.; Xu, X.; Zhu, X., A simple approach to fabricate superoleophobic coatings. *New J. Chem.* **2011,** *35*, 576-580.

38. Wang, X.; Hu, H.; Ye, Q.; Gao, T.; Zhou, F.; Xue, Q., Superamphiphobic coatings with coralline-like structure enabled by one-step spray of polyurethane/carbon nanotube composites. *J. Mater. Chem.* **2012,** *22*, 9624-9631.
39. Campos, R.; Guenthner, A. J.; Meuler, A. J.; Tuteja, A.; Cohen, R. E.; McKinley, G. H.; Haddad, T. S.; Mabry, J. M., Superoleophobic Surfaces through Control of Sprayed-on Stochastic Topography. *Langmuir* **2012,** *28*, 9834-9841.
40. Ge, B.; Zhang, Z.; Men, X.; Zhu, X.; Zhou, X., Sprayed superamphiphobic coatings on copper substrate with enhanced corrosive resistance. *Appl. Surf. Sci.* **2014,** *293*, 271-274.
41. Muthiah, P.; Bhushan, B.; Yun, K.; Kondo, H., Dual-layered-coated mechanically-durable superomniphobic surfaces with anti-smudge properties. *J. Coll. Interf. Sci.* **2013,** *409*, 227-236.
42. Tiwari, M. K.; Bayer, I. S.; Jursich, G. M.; Schutzius, T. M.; Megaridis, C. M., Highly Liquid-Repellent, Large-Area, Nanostructured Poly(vinylidene fluoride)/Poly(ethyl 2-cyanoacrylate) Composite Coatings: Particle Filler Effects. *ACS Appl. Mater. Interfaces* **2010,** *2*, 1114-1119.
43. Xue, Z.; Liu, M.; Jiang, L., Recent developments in polymeric superoleophobic surfaces. *J. Polym. Sci. Part B: Polym. Phys.* **2012,** *50*, 1209-1224.
44. Butt, H.-J.; Semprebon, C.; Papadopoulos, P.; Vollmer, D.; Brinkmann, M.; Ciccotti, M., Design principles for superamphiphobic surfaces. *Soft Matter* **2013,** *9*, 418-428.
45. Liu, K.; Tian, Y.; Jiang, L., Bio-inspired superoleophobic and smart materials: Design, fabrication, and application. *Prog. Mater. Sci.* **2013,** *58*, 503-564.
46. Chu, Z.; Seeger, S., Superamphiphobic surfaces. *Chem. Soc. Rev.* **2014,** *43*, 2784-2798.
47. Xiong, D.; Liu, G.; Scott Duncan, E. J., Robust amphiphobic coatings from bi-functional silica particles on flat substrates. *Polymer* **2013,** *54*, 3008-3016.
48. Sparks, B. J.; Hoff, E. F. T.; Xiong, L.; Goetz, J. T.; Patton, D. L., Superhydrophobic Hybrid Inorganic–Organic Thiol-ene Surfaces Fabricated via Spray-Deposition and Photopolymerization. *ACS Appl. Mater. Interfaces* **2013,** *5*, 1811-1817.
49. Shin, J.; Nazarenko, S.; Hoyle, C. E., Effects of Chemical Modification of Thiol−Ene Networks on Enthalpy Relaxation. *Macromolecules* **2009,** *42*, 6549-6557.
50. Goetz, J.; Kwisnek, L.; Nazarenko, S., From Gas Barriers to High Gas Flux Membranes: UV-Cured Thiol-ene Networks for Transport Applications. *RadTech Report* **2012,** *27*, 27-32.
51. Fowkes, F. M., Attractive forces at interfaces. *Ind. Eng. Chem.* **1964,** *56*, 40-52.
52. Seah, M. P.; Dench, W. A., Quantitative electron spectroscopy of surfaces: A standard database for electron inelastic mean free paths in solids. In *Surf. Interface Anal.*1979; Vol. 1, pp 2-11.
53. Zhu, X.; Zhang, Z.; Yang, J.; Xu, X.; Men, X.; Zhou, X., Facile fabrication of a superhydrophobic fabric with mechanical stability and easy repairability. *J. Coll. Interf. Sci.* **2012,** *380*, 182-186.
54. Yeong, Y. H.; Davis, A.; Steele, A.; Loth, E.; Bayer, I. S., Spray deposition effects on superhydrophobicity and durability of nanocoatings. *Surf. Innovations* **2014,** *Ahead of Print 10.1680/si.13.00044*.
55. Mao, Y.; Gleason, K. K., Vapor-Deposited Fluorinated Glycidyl Copolymer Thin Films with Low Surface Energy and Improved Mechanical Properties. *Macromolecules* **2006,** *39*, 3895-3900.
56. Thomas, R. R.; Anton, D. R.; Graham, W. F.; Darmon, M. J.; Sauer, B. B.; Stika, K. M.; Swartzfager, D. G., Preparation and Surface Properties of Acrylic Polymers Containing Fluorinated Monomers. *Macromolecules* **1997,** *30*, 2883-2890.

57. Moulder, J. F.; Stickle, W. F.; Sobol, P. E.; Bomben, K. D., *Handbook of X-ray Photoelectron Spectroscopy*. Perkin-Elmer Corp., Physical Electronics: Eden Prairie, MN, 1995.
58. Bernett, M. K.; Zisman, W. A., Wetting properties of tetrafluoroethylene and hexafluoropropylene copolymers. *J. Phys. Chem.* **1960,** *64*, 1292-1294.
59. Tsibouklis, J.; Graham, P.; Eaton, P. J.; Smith, J. R.; Nevell, T. G.; Smart, J. D.; Ewen, R. J., Poly(perfluoroalkyl methacrylate) Film Structures: Surface Organization Phenomena, Surface Energy Determinations, and Force of Adhesion Measurements. *Macromolecules* **2000,** *33*, 8460-8465.
60. Kumar, V.; Pulpytel, J.; Rauscher, H.; Mannelli, I.; Rossi, F.; Arefi-Khonsari, F., Fluorocarbon Coatings Via Plasma Enhanced Chemical Vapor Deposition of 1H,1H,2H,2H-perfluorodecyl Acrylate - 2, Morphology, Wettability and Antifouling Characterization. *Plasma Process. Polym.* **2010,** *7*, 926-938.
61. Jung, Y. C.; Bhushan, B., Mechanically Durable Carbon Nanotubeâ˜Composite Hierarchical Structures with Superhydrophobicity, Self-Cleaning, and Low-Drag. *ACS Nano* **2009,** *3*, 4155-4163.
62. Su, C.; Xu, Y.; Gong, F.; Wang, F.; Li, C., The abrasion resistance of a superhydrophobic surface comprised of polyurethane elastomer. *Soft Matter* **2010,** *6*, 6068-6071.
63. Verho, T.; Bower, C.; Andrew, P.; Franssila, S.; Ikkala, O.; Ras, R. H. A., Mechanically Durable Superhydrophobic Surfaces. *Adv. Mater.* **2011,** *23*, 673-678.
64. Steele, A.; Bayer, I.; Loth, E., Adhesion strength and superhydrophobicity of polyurethane/organoclay nanocomposite coatings. *J. Appl. Polym. Sci.* **2012,** *125*, E445-E452.
65. Huovinen, E.; Takkunen, L.; Korpela, T.; Suvanto, M.; Pakkanen, T. T.; Pakkanen, T. A., Mechanically Robust Superhydrophobic Polymer Surfaces Based on Protective Micropillars. *Langmuir* **2014,** *30*, 1435-1443.
66. Raza, A.; Si, Y.; Wang, X.; Ren, T.; Ding, B.; Yu, J.; S. Al-Theyab, S., Novel fluorinated polybenzoxazine-silica films: chemical synthesis and superhydrophobicity. *RSC Adv.* **2012,** *2*, 12804-12811.
67. Bayer, I. S.; Fragouli, D.; Martorana, P. J.; Martiradonna, L.; Cingolani, R.; Athanassiou, A., Solvent resistant superhydrophobic films from self-emulsifying carnauba wax-alcohol emulsions. *Soft Matter* **2011,** *7*, 7939-7943.
68. Deng, X.; Schellenberger, F.; Papadopoulos, P.; Vollmer, D.; Butt, H.-J., Liquid Drops Impacting Superamphiphobic Coatings. *Langmuir* **2013,** *29*, 7847-7856.

2.6 Appendix - Spray-Deposition and Photopolymerization of Organic-Inorganic Thiol-Ene Resins for Fabrication of Superamphiphobic Surfaces

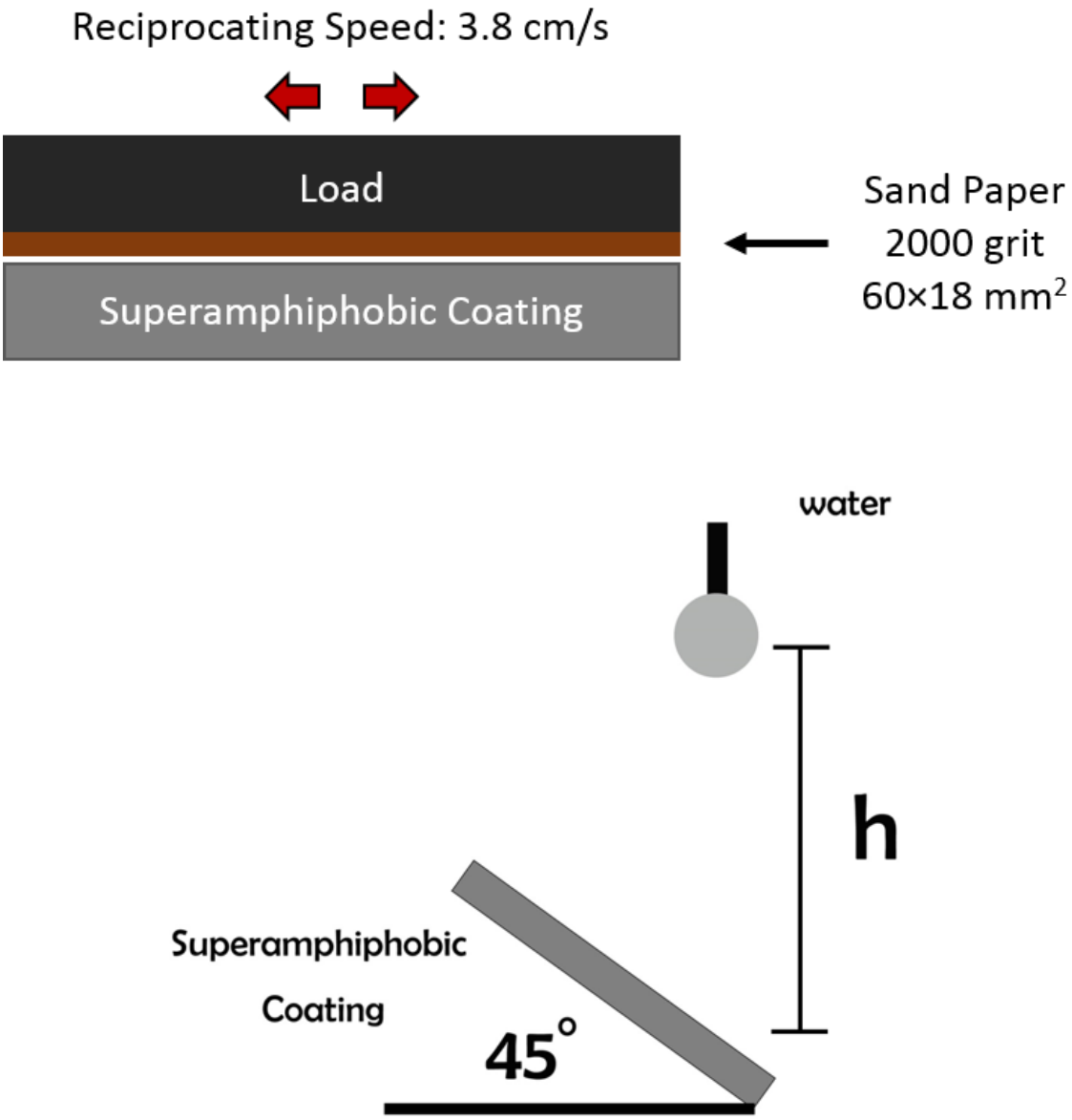

Figure A.1 Experimental setup for the (a) reciprocating abrasion test and the (b) drop impact test.

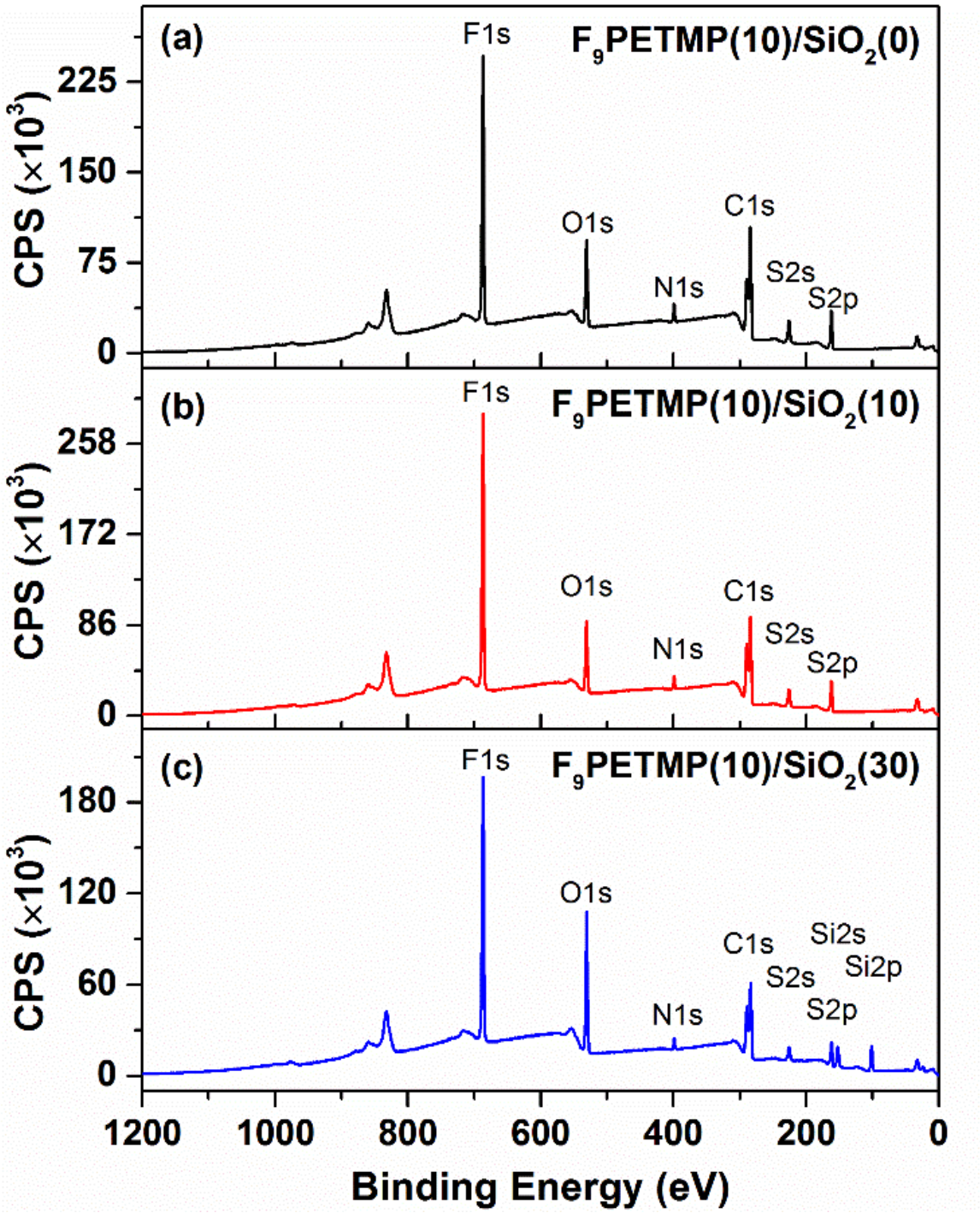

Figure A.2 XPS survey spectra fro (a) F_9PETMP(10)/SiO_2(0), (b) F_9PETMP(10)/SiO_2(10), and (c) F_9PETMP(10)/SiO_2(30).

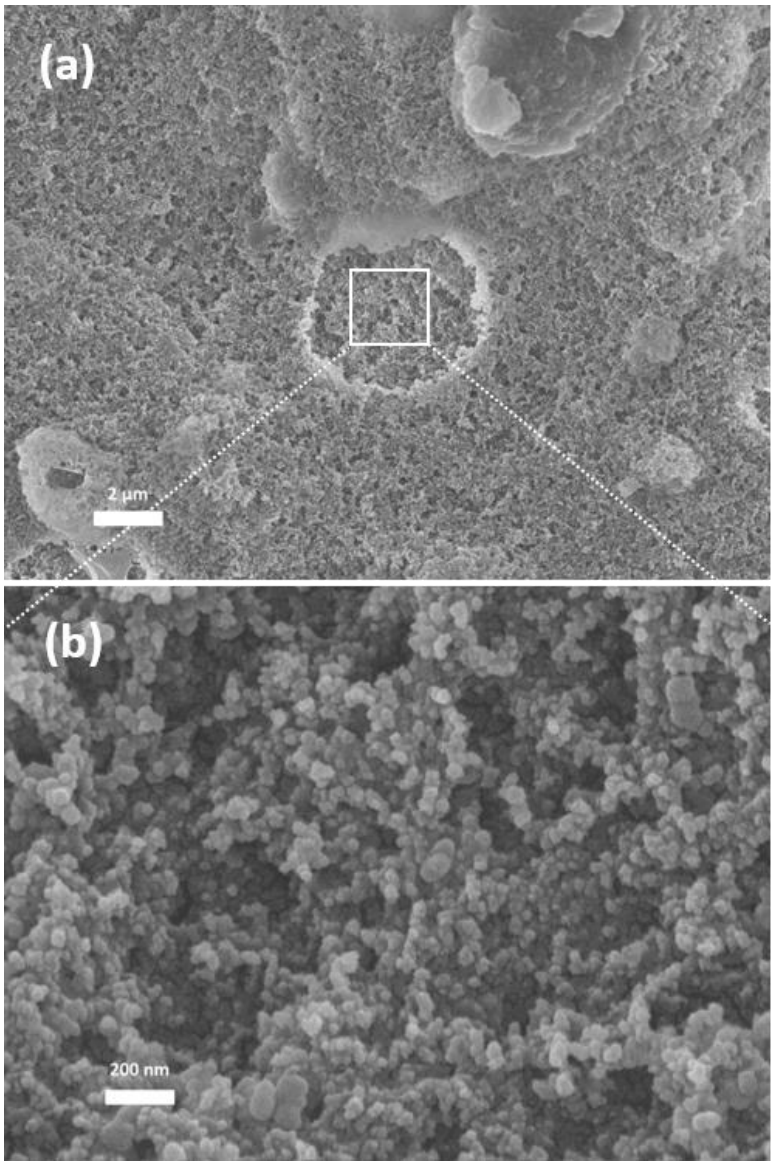

Figure A.3 SEM images of a F_9PETMP(30)/SiO_2(30) following 200 abrasion cycles.

(a) shows a crater remaining after removal of a large spherical agglomerate from the surface. (b) shows a high-resolution image inside the crater illustrating the presence of nanoparticles. The hierarchical structure throughout the thickness of the film imparts a mechanical robustness to the anti-wetting behavior and is particular beneficial in supporting superhydrophobicity following abrasive damage.

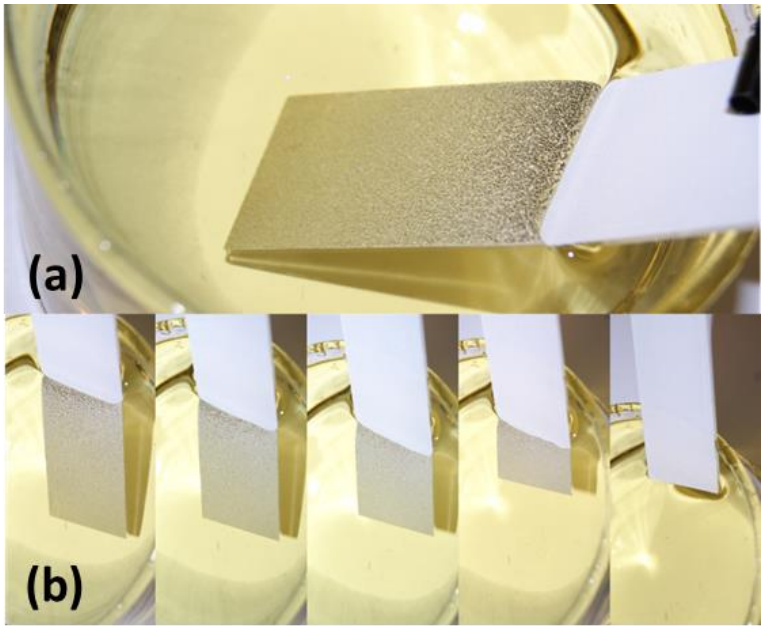

Figure A.4 Photograph of the superamphiphobic sample in cooking oil.

Photograph showing the mirror-like surface resulting from the submersion of the superamphiphobic sample into cooking oil and the subsequent removal showing an oil-free surface.

CHAPTER III – SUPERHYDROPHILIC / SUPEROLEOPHOBIC SURFACE VIA SPRAY DEPOSITION AND THIOL-ACRYLATE PHOTOPOLYMERIZATION FOR OIL/WATER SEPARATION

3.1 Introduction

Recently, environmental catastrophes, such as the Deepwater Horizon oil spill, have received significant attention because of the detrimental impact of the oil on the ocean and estuary ecosystems.[1-2] Following a major spill event, there are four primary methods employed for cleanup: (1) the oil is left to natural means of dispersion and evaporation; (2) the oil is isolated with booms and skimmer equipment is employed to collect the oil from the water surface, (3) the oil is sequestered with absorbents to prevent spreading, and (4) the oil is sequestered with dispersants/surfactants to enable biological organisms to break down the oil and accelerate the biodegradation process.[3-5] However, these methods all suffer from limitations including long timeline requirements, high energy consumption, low separation efficiency, and low economic feasibility. In addition to oil spills, the separation of oil from industrial wastewater continues to be a major challenge. Efficient and economically effective treatments for separation of oil from polluted wastewater, particularly mixtures containing surfactants with dispersed oil droplets, are highly desired.[6]

The development of membrane-based oil/water separation methodologies has given rise to many advantages over the traditional separation technologies, including high separation efficiency, low energy consumption, scalable productivity, good stability, and durability. Membranes tailored with special wettability have been widely reported in recent years in attempt to realize efficient oil/water separations. For example,

superhydrophobic/superoleophilic surfaces with extreme repellency toward water but strong affinity to oil offer the possibility to achieve highly efficient oil/water separations. The Jiang group first reported a superhydrophobic and superoleophilic hard coating mesh film prepared by a spray-and-dry method from a fluorine-containing material. The authors employed the mesh membrane for separation of non-emulsified diesel oil and water with high efficiency.[7] After their work, multiple physical and chemical strategies have been developed to fabricate superhydrophobic/superoleophilic materials for oil/water separation.[8-9] However, many limitations arise with the practical application of superhydrophobic/superoleophilic membranes. Due to the difference in density of water and oil, the mesh makes contact with the water layer and the superhydrophobic nature of the membrane blocks the filtration process; this design often requires specific engineering at the point of separation. Therefore, it is more feasible to design and fabricate membranes with superoleophobic/superhydrophilic coating. These water-loving and water-permeable membranes are advantageous over traditional superhydrophobic/superoleophilic materials for two reasons: (1) they enable water to pass freely, which effectively avoids or reduces the possibility of membrane fouling by a viscous oil; (2) they prevent the formation of the water barrier between the membrane and the oil phase. However, surfaces that repel oil also generally repel water due to the higher surface tension of water. Other research has focused on the fabrication of superhydrophilic/underwater superoleophobic coatings. The hydrophilic nature of these coatings can trap water molecules at the surface, exhibiting a high underwater oil contact angle and low contact angle hysteresis in aqueous environments.[6, 10] A significant contribution to the fabrication of superhydrophilic/ underwater superoleophobicc coating

was reported by Jiang *et al*. Inspired from fish scales, Jiang reported a fluorine-free underwater superoleophobic Polyacrylamide (PAM) film prepared by a template method to provide a rough underwater superoleophobic film that exhibited selectivity permeation to water and oil.[11] Later, the same group published work on superhydrophilic/underwater superoleophobic hydrogel-coated mesh membranes for separating an immiscible oil/water mixture.[12] A series of reports followed that described the fabrication of underwater superoleophobic materials and demonstrated the potential application of these materials in oil/water separation.[13-19] A breakthrough work on fabricating superhydrophilic/superoleophobic surfaces was reported by Yang and co-workers.[20] Yang first reported a superhydrophilic/superoleophobic nanocomposite coating prepared by spray deposition of SiO_2 nanoparticles, a fluorosurfactant, and a hydrophilic polymer mixture. Philip and coworkers[13, 21] used a spray-deposition layer-by-layer technique to spray a polyelectrolyte binder, SiO_2 nanoparticles, and a fluorosurfactant to achieve a superhydrophilic/superoleophobic coating. The approach used by Philip was to introduce a fluorosurfactant, which has a low surface energy tail and a high surface energy head, into the layer-by-layer composition. The hydrophilic head showed water affinity while the tail exhibited oil repellency. However, the fluorosurfactant was bound to the surface with only electrostatic interactions – an approach that is not chemically stable for long-term use. Apart from these pioneering examples, few reports have been published on superhydrophilic-superoleophobic membranes that target separation performance of oil/water emulsions.

In our previous work, superhydrophobic and superamphiphobic coatings were prepared via a spray deposition method using thiol-ene photopolymerization.[22-23] Herein,

we describe a simple strategy to fabricate superhydrophilic-superoleophobic surfaces by spray coating hydrophilic-oleophobic thiol-acrylate resins with nanoparticle suspensions. The prepared coating showed both superhydrophilicity and superoleophobicity where the water droplet easily spread out on the surface and oil droplet readily roll off without any penetration. The performance of these superhydrophilic-superoleophobic coating on oil/water emulsion and dye- containing emulsion separation was studied.

3.2 Experimental Section

3.2.1 Materials.

All reagents were obtained at the highest purity available and used without further purification unless otherwise specified. (2-carboxyethyl acrylate), poly(ethyl glycol) diacrylate 400, 2,2-dimethoxy-2-phenylacetophenone (DMPA) and acetone were obtained from Sigma-Aldrich, pentaerythritol, tetra(3-mercaptopropionate) (PETMP) was obtained from Bruno Bock, Fluorinated PETMP (F-PETMP) was synthesized according to literature.[24] Aerosil R380, hydrophilic fumed silica with hydroxyl surface functionalization and an average primary particle size of 16 nm was kindly provided by Evonik Industries.

3.2.2 Characterization.

Contact angle measurements were performed using a Rame-Hart 200-00 Std.-Tilting B. goniometer. Static contact angles were measured using 6 μL water droplets. ImageJ Drop Analysis was used to analyze the droplets. Scanning electron microscopy (SEM) images were obtained using a Zeiss Sigma VP FEG-SEM at 10 kV in high vacuum mode. Raman spectroscopy was conducted using an iRaman Plus. The thiol conversion was monitored by measuring the area of the thiol absorption peak at 2576

cm^{-1}. Conversions were calculated with the ratio of peak area to the peak area prior to polymerization. All reactions were performed under ambient conditions. Transmission electron micrographs (TEM) (Digital Imaging with Gatan Model 785 ES1000W Erlangshen CCD Camera) were taken with a Zeiss 900 TEM operating at 50 kV. UV/VIS spectra were obtained by using PerkinElmer Lambda 35 UV/VIS Spectrometer. Optical microscope images were obtained by using Olympus BX52 digital optical microscope system. Dynamic light scattering analysis was conducted by Microtrac Nanotrac Ultra. Confocal images were taken using Zeiss LSM 510 confocal laser scanning microscope with a 543 nm HeNe laser.

3.2.3 Film Preparation.

As shown in Scheme 3.1, the thiol-acrylate based hybrid resins were prepared by weighing out a tri-functional thiol (F-PETMP), hydrophilic alkene (2-carboxyethyl acrylate), cross-linker poly(ethyl glycol) diacrylate 400, and photoinitiator (DMPA) into a glass jar. A specified amount of hydrophilic hydroxyl-modified aerosol nanoparticles ($OH\text{-}SiO_2$) (Aerosil R380 = 30, 40, 50, 60 wt.% relative to resin) was added to the resin mixture. Fluorinated multifunctional thiol (F-PETMP) was added at 0, 20, 30, 40 and 50 wt.% relative to the total organic resin. For the formulations containing F-PETMP, the stoichiometric ratio of alkene to thiol was 13.7： 1, 8:1, 6.8:1 and 4.9:1 accordingly. The hybrid mixture was diluted in acetone (20:1 w/w solvent/resin) and then treated with bath ultrasonication (Fisher Scientific Ultrasonic Cleaner) for 30 min.

An airbrush with a nozzle diameter of 0.635 mm (Paasch H#3 obtained from McMaster Carr) was connected to a compressed nitrogen source (30 psi) and used to spray coat the resin onto substrates at a distance of 15 cm and with a rate of 2 mL/min.

Different substrates were sprayed, including glass slides, stainless steel mesh with 200 mesh size, cotton cloth and nylon filter membranes with either a 0.8 or 0.45 μm pore size. The coating was allowed to sit for 1 minute before curing under a UV flood lamp (16 mW/cm^2) for 5 min. In order to simplify the notation for each system, we will represent the various formulations as F-PETMP(x)/SiO_2(y), where x and y represents the weight percentage of F-PETMP and OH-SiO_2, respectively.

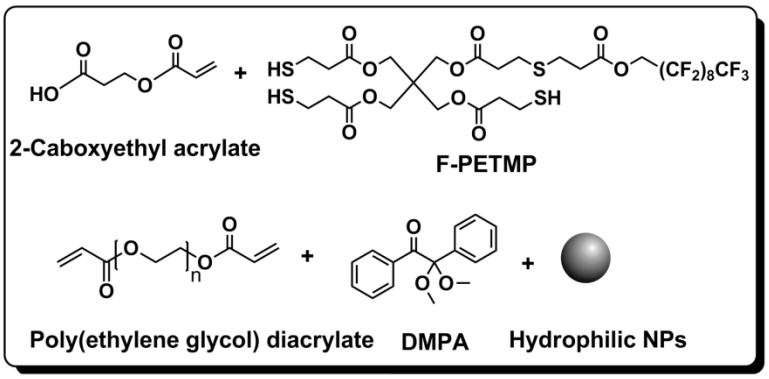

Scheme 3.1 Schematic of the spray deposition and photo-polymerization process using hybrid inorganic−organic thiol-acrylate resins laden with hydrophilic silica nanoparticles.

3.2.4 Oil/Water Mixtures.

A surfactant free oil/water mixture was prepared by mechanically mixing hexane and water together. An oil/water emulsion was prepared by sonicating water (500 g), toluene (5 g) and SDS (1.2 g) together until the solution formed a homogeneous single emulsion layer. A fluorescent dye oil/water emulsion was prepared by sonicating Nile red (10 mg), water (500 g), hexadecane (5g) and SDS (1.2 g) together until a homogeneous single layer formed.

3.3 Results and Discussion

3.3.1 Chemical Composition.

The coating comprising both hydrophilic and oleophobic constituents was synthesized using thiol-acrylate photopolymerization. The advantages of the thiol-acrylate photopolymerization includes fast reaction rates, high conversion, oxygen insensitivity, and low shrinkage of the polymer. The monomer 2-carboxyethyl acrylate and the cross-linker poly(ethylene glycol) diacrylate were selected as the acrylate resin to provide the coating with good hydrophilicity. The weight ratio of the two hydrophilic monomers was kept at 10: 1 to simplify the formulation, as well as to fabricate a coating with a moderate cross-linking density. To introduce oleophobicity to the film, 1H,1H-perfluoro-n-decyl functionalized PETMP (F-PETMP), was added into the acrylate resin system at 20 wt.%, 30 wt.%, 40 wt.% and 50 wt.% relative to the total acrylate organic resin. The low surface energy fluorinated carbon chain together with the high surface energy carboxyl groups provides the surface of the material with simultaneously oleophobicity and hydrophilicity, which can be appropriately balanced to provide the desired wetting properties.

As indicated by the formulation parameters, a non-stoichiometric thiol-acrylate polymerization was employed in this study due to the high reactivity of the acrylate group. The thiol-acrylate polymerization proceeds in a binary process involving two different mechanisms: step-growth and chain-growth. In ideal thiol-ene systems, the step-growth mechanism dominates the chain-growth homopolymerization because the alkene monomers commonly employed do not readily undergo homopolymerization. However, in thiol-acrylate systems, a competition exists between the step-growth mechanism of the

thiol-ene polymerization and the chain-growth due to the homopolymerization of the acrylate group. If stoichiometric conditions are employed, these conditions lead to a higher conversion of the acrylate functional group compared to the thiol functional group resulting in a certain amount of unreacted thiols in the polymer matrix. To achieve high conversion of both acrylate and thiol functional groups, we formulated the resins with excess acrylate. The molar ratios of the acrylate group to thiol group were calculated as 13.7:1 (20 wt.% F-PETMP), 8:1 (30 wt.% F-PETMP), 6.8:1 (40 wt.% F-PETMP) and 4.9:1 (50 wt.% F-PETMP).

First, Raman spectroscopy was used to monitor the thiol conversion in the pristine resin upon increasing the F-PETMP concentration from 20 wt.% to 50 wt.% (with no NPs added). Figure 3.1a shows the Raman spectra for thiol-acrylate resin before UV exposure at different F-PETMP content. The thiol and alkene peaks at 2569 cm^{-1} and 1634 cm^{-1}, respectively, are highlighted with gray boxes. Figure 3.1b shows the Raman spectra of the thiol-acrylate formulations after UV exposure. The acrylate group exhibited complete conversion in all of the formulations, as evidenced by the total disappearance of the characteristic peak at 1634 cm^{-1}, whereas the thiol group showed conversions that were dependent on the F-PETMP loading level in the formulation. The change in thiol group peak area was converted to percent conversion values and plotted against F-PETMP concentration, as illustrated in Figure 3.1c. As shown, thiol conversion decreased with increasing F-PETMP content due to the presence of acrylate homopolymerization. At 20 wt.% and 30 wt.% F-PETMP loading level, thiol conversion was ~96.6%, which indicates the thiol functional groups were mostly consumed in the step-growth process. When F-PETMP was increased to 50 wt.%, thiol conversion decreased to ~83.6%, which

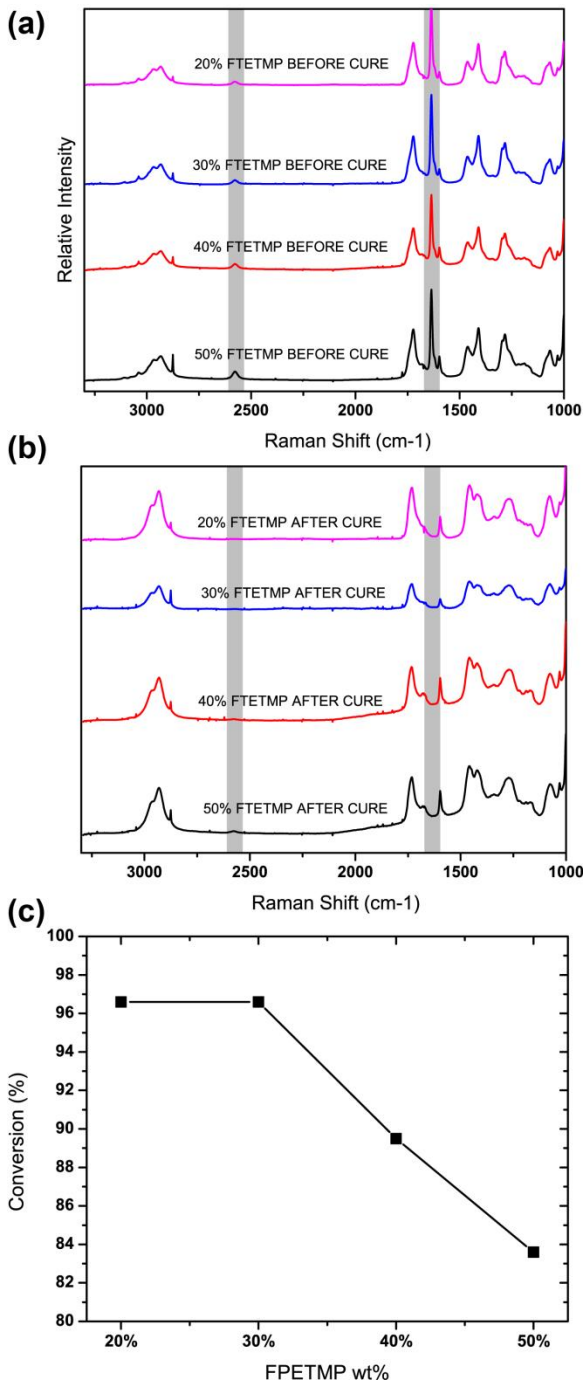

Figure 3.1 Raman spectra for the thiol-acrylate films with different F-PETMP content (a) before and (b) after UV exposure; (c) the calculated thiol conversion.

indicates that less thiol is consumed in the step-growth process resulting in unreacted thiol monomers. To obtain polymer coatings with minimum monomer residues, the

highest content of F-PETMP added into the resin system was 50 wt.% for the remaining worked described below.

3.3.2 Wetting Properties of Non-textured Surfaces.

With an understanding of the thiol-acrylate polymerization behavior, we fabricated non-textured films (e.g. without fumed silica) by spray-coating to study the wetting properties of the pristine polymer resin. The wetting properties of the films were evaluated with via static oil and water contact angle measurements. Hexadecane (γ = 27 mN/m) was used as the probe liquid for oil contact angle (OCA) and DI water (γ = 72.4 mN/m) was used for water contact angle (WCA). Figure 3.2 shows the wetting behavior of the non-textured photocured films containing 0 wt.% to 50 wt.% of F-PETMP. The non-fluorinated film was completely wetted by both hexadecane (OCA= 4.6 ± 0.9°) and water (WCA= 8.6 ± 0.8°) due to the hydrophilic nature of the acidic acrylate resin and the absence of a low surface energy component. After incorporating F-PETMP into the resin, the surface energy of the cured film was significantly decreased resulting in increased WCA and OCA values. As shown in Figure 3.2, the film containing 20 wt.% F-PETMP exhibited a hydrophilic WCA at 24.6 ± 0.6° indicating an overwhelming contribution from the polar carboxylic acid groups in the resin. However, further increasing the concentration of F-PETMP to 30 wt.% resulted in rapid WCA increase to 85.1±0.5° indicating a transition from hydrophilicity towards hydrophobicity. The WCA plateaued at 113.8±0.8° at 50 wt.% F-PETMP. In contrast, the OCA of the film rapidly increased to 75.5±0.7° with 20 wt.% F-PETMP, but only showed a small change in OCA with further additions of F-PETMP (30 – 50 wt.%) to the resin. This observation can be

attributed to the saturation of the 1H,1H-perfluoro-n-decylfunctional groups along the surface.[25]

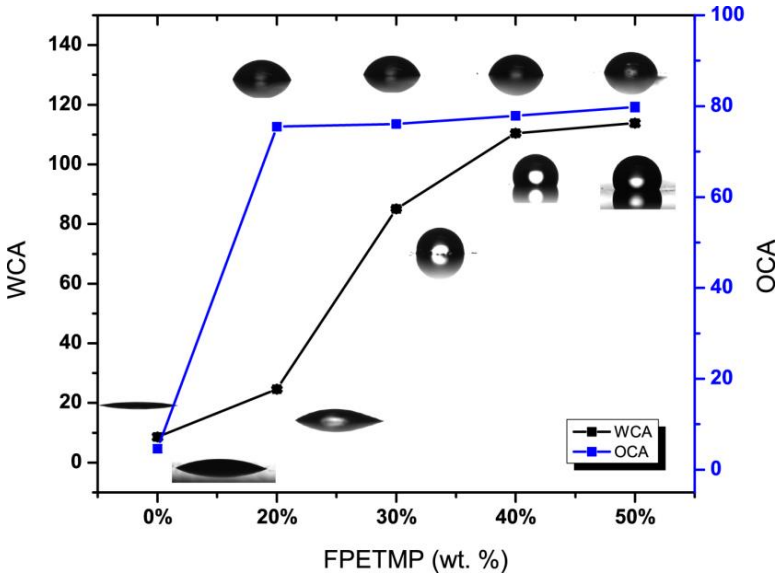

Figure 3.2 Variation of static water and oil contact angle as a function of F-PETMP content of non-textured films.

Water contact angle (the black line) and oil contact angle (the blue line) change with the variation of F-PETMP content of non-textured films. The inserted images are representative photographs of water and oil droplets (6 μL) on the non-textured surface.

3.3.3 Textured Surface.

Many previous studies have shown that wetting properties can be amplified by creating a highly textured surface morphology to enhance the liquid-solid interactions resulting in superhydrophilic and superoleophobic wetting behavior. To enhance both wetting and anti-wetting behavior, textured surfaces were incorporated with thiol-acrylate resin to amplify the liquid-solid interactions.

3.3.3.1 Surface Morphology and Chemical Composition of Textured Films.

A spray deposition method and inorganic OH-SiO_2 nanoparticles were used to endow the thiol-ene film with the hierarchical roughness that is essential for obtaining superhydrophilic/superoleophilic and superhydrophobic/superoleophobic properties.

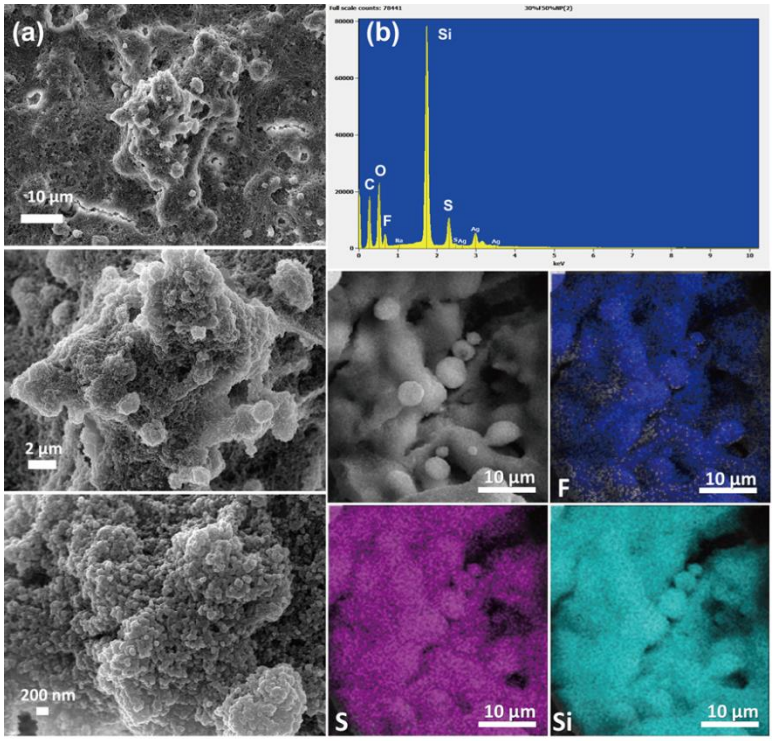

Figure 3.3 Surface morphology and chemical composition of F-PETMP(30)/SiO_2(50) textured films.

(a) High resolution SEM micrographes of F-PETMP(30)/SiO_2(50) at different magnification; (b) EDS spectrum of F-PETMP(30)/SiO_2(50) and elemental map of control, F, S, Si respectively.

In our previous studies, we have shown that with increasing SiO_2 nanoparticle content, the film exhibited an increase in surface roughness on both micro- and nano-scale. In this work, we used SEM to investigate the surface morphology of sample F-PETMP(30)/SiO_2(50) spray deposited on a glass slide substrate. As shown in Figure 3.3a, the entire surface exhibited a very similar morphology to our earlier work,[25-26] with randomly distributed micrometer and submicrometer agglomerations observed on the surface that can be attributed to the spray deposition process. The higher magnification images clearly show that the micrometer and submicrometer scale aggregates are superimposed with a nanometer-scale roughness that arises from the fumed silica

aggregates. The combination of micro- and submicrometer-sized particles provides the surface with a porous, hierarchically structured morphology.

Energy dispersive spectroscopy (EDS) analysis was used to explore the surface elemental composition of the F-PETMP(30)/SiO_2(50) sample. As shown in Figure 3.3b, it is clear that the surfaces were mainly composed of F, S, Si, C and O elements. The fluorine content of the cured film obtained from EDS was 8.78 ± 0.13 wt.%, while the content calculated from the bulk resin composition for F-PETMP(30)/SiO_2(50) was 5.33 wt.%. The higher F content result indicates the self-migration of fluorine-carbon chain from the bulk to the surface, which provides the basis for the superoleophobicity of the surface. The presence of sulfur and silicon in the EDS originate from the trifunctional thiol and fumed silica nanoparticles, respectively. Further, EDS elemental mapping of F, S and Si indicates all elements are equally distributed across the surface of the coating.

3.3.3.2 Wetting property of the Textured Film.

Figure 3.4a and 3.4b show the static WCA and OCA, respectively, as a function of OH-SiO_2 nanoparticle and F-PETMP loading levels. The wetting data is also summarized in Table 3.1. In these experiments, OH-SiO_2 NP content was adjusted from 30 wt.% to 60 wt.% of the resin, while F-PETMP concentration was varied from 20 wt.% to 50 wt.% of the acrylate resin. Here, it is necessary to mention here that the water contact angle on these surfaces changed with time, thus, the WCA was recorded 1 minute after placing the droplet in contact with the surface when the CA didn't change. The textured surface fabricated with F-PETMP(0)/SiO_2(30), with NP content changed from 30 wt.% to 60 wt.% exhibited very low contact angles (< 5°) for both water and oil – behavior that is associated with a surface that is demonstrates both superhydrophilic and

superoleophilic wetting behavior. The F-PETMP(20)/SiO_2(30) surface showed a 18.7±0.4° WCA, which decreased to 0° with further additions of OH-SiO_2 due to the

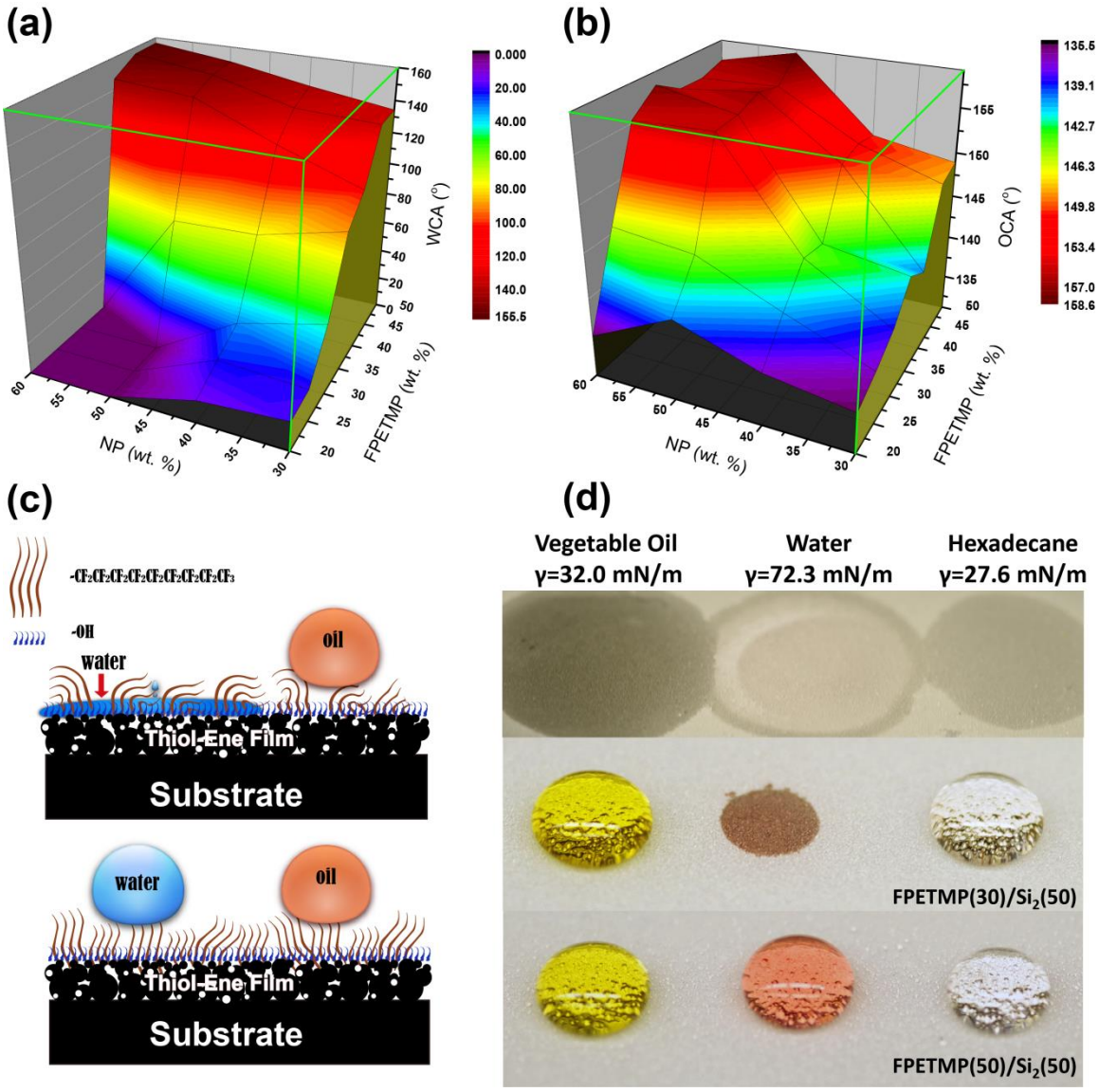

Figure 3.4 Variation of static water and oil contact angle as a function of OH-SiO2 nanoparticle loading level and F-PETMP content.

Variation of (a) the static water contact angle (WCA), (b) the static oil contact angle (OCA) as a function of OH-SiO2 nanoparticle loading level for samples formulated with F-PETMP; (c) illustrated configuration of the evolution of water and oil wetting property on the coated surface (d) Photo of vegetable oil, hexadecane and water droplet on the surface of samples F-PETMP(0)/SiO2(50), F-PETMP(30)/SiO2(50), and F-PETMP(50)/SiO2(50).

hydrophilic contribution of hydroxyl functional groups on the silica. The PETMP(20)/SiO_2(30) surface exhibited a sharp OCA increase to 135.5±1.6°, which further increased to 140.1±2° at the 50 wt.% OH-SiO_2 loading level. Increasing the F-PETMP concentration to 30 wt.%, the F-PETMP(30)/SiO_2(30) showed similar trends

Table 3.1

Summary of Contact Angle Data for Sprayed F-PETMP/SiO_2 Thiol-Acrylate Thin Films

SiO_2 (%) (y)	WCA (°)	WSA (°)	OCA (°)	OSA (°)
F-PETMP(20)/SiO_2(y)				
30	18.7±0.4	-	135.5±1.6	-
40	14.5±0.8	-	136.9±1.9	-
50	0	-	140.1±2	-
60	0	-	135.7±1.1	-
F-PETMP(30)/SiO_2(y)				
30	45.7±1.1	-	138.7±1.7	-
40	32.1±0.5	-	144.2±2.1	-
50	0	-	155.6±1	10±1
60	0	-	155.3±0.9	12±1
F-PETMP(40)/SiO_2(y)				
30	103.6±0.7	-	140.2±0.6	-
40	121.9±1.1	-	150.5±1.5	-
50	142.8±0.9	-	156.1±0.9	7±2
60	146.7±1.3	-	155.9±0.8	7±1
F-PETMP(50)/SiO_2(y)				
30	134.3±0.6	-	148.9±1.4	-
40	141.8±1.2	-	150.5±0.7	12±2
50	150.6±0.8	5±1	158.6±0.8	7±1
60	156.6±0.9	5±1	156.7±1	8±1

with respected to both WCA and OCA as previously described. Notably, the F-PETMP(30)/SiO_2(50) surface showed a minimum WCA value of 0°, a maximum OCA value of 155.6±1°, and an oil sliding angle (OSA) = 10±1° – results that indicate the desired superhydrophilic/superoleophobic wetting behavior. Additional increases in the F-PETMP content up to 50 wt.% resulted in both WCA and OCA values of 150.6±0.8°

and 158.6±0.8°, respectively. Likewise, the water sliding angle (WSA) and OSA values were 5±1° and 7±1°, respectively. These results indicate that the F-PETMP(40)/SiO_2(50) and F-PETMP(50)/SiO_2(50) exhibit superamphiphobic wetting behavior – properties that are undesirable for the targeted approach of oil-water separations. Creating a detailed wetting map enabled the identification of a specific formulation that balances the contributions from the high surface energy hydroxyl and carboxylic acid functional groups derived from the silica and acrylate resin with the low surface energy fluorocarbon groups derived from the multifunctional thiol to yield the atypical superhydrophilic/superoleophobic wetting state. Specifically, for the F-PETMP(30)/SiO_2(50) formulation, we postulate that the composition of the surface allows rearrangement of the interface in response to contact with water exposing a great fraction of COOH groups resulting in a fully wetted interface. Similarly, the long fluorocarbon chains are preferentially presented at the interface in response to contact with a low surface tension liquid resulting in a non-wetted interface. Figure 3.4d shows photographs of droplets of vegetable oil, water, and hexadecane on the surface of sample F-PETMP(0)/SiO_2(0), F-PETMP(30)/SiO_2(50) and F-PETMP(50)/SiO_2(50). The polar water and non-polar oil droplets completely wet the superhydrophilic/superoleophilic F-PETMP(0)/SiO_2(0) surface, show opposite wetting behavior on superhydrophobic/superoleophobic F-PETMP(50)/SiO_2(50) surface. On the F-PETMP(30)/SiO_2(50) sample, water completely wets the surface while vegetable oil and hexadecane exists in a non-wetting state as indicated by the observed air bubbles trapped under the drops. Again, this simple demonstration illustrates the desired superhydrophilic/superoleophobic wetting behavior for oil/water separations.

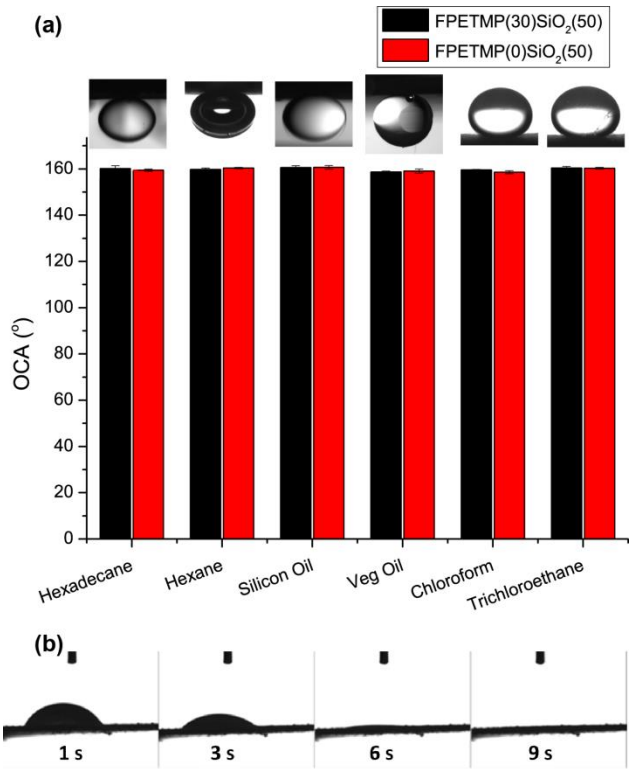

Figure 3.5 Static contact angle of a series of typical oil droplets on the coated membrane in aqueous media.

(a) the contact angle of a series of typical oil droplets on the coated membrane in aqueous media. The photos above the columns are representative photographs of oil droplets (4 μl) on the membrane surface in water. (b) A series of photos of a water droplet contacting on the cured film in air shown that the film can be easily wetted by water.

To further evaluate the wetting behavior of the superhydrophilic/superoleophobic sample F-PETMP(30)/SiO_2(50), we investigated the oleophobicity under aqueous conditions with different type of oils. For comparison, a superhydrophilic/superoleophilic F-PETMP(0)/SiO_2(50) sample was also investigate. Contact angle measurements were conducted under water using a series of low surface tension liquid probes, including hexadecane, hexane, silicon oil, vegetable oil, chloroform, and trichloroethane. As shown in Figure 3.5, the spray coated films on glass slide substrate exhibited underwater OCAs larger than 150° for all of the oils without any exception, thus confirming the underwater superoleophobicity of the F-

PETMP(30)/SiO_2(50) and signifying good potential for oil/water separation. The inset photos on the top show oil droplets on the surface immersed in water, as can be seen, that the oil droplets form spherical shapes on the surface indicate good oleophobicity. Furthermore, these oil droplets had very low sliding angle (< 1°) in water environment, which demonstrates the coated film had very low adhesion superoelophobicity underwater. Figure 3.5b displays a series of photos of a water droplet making contact with the sample F-PETMP(30)/SiO_2(50) spray coated on nylon membrane substrate, and the result shows that the coated membrane was quickly wetted in 9 seconds by the water droplet indicating the potential application of the membrane on oil/water separation.

3.3.4 Oil/Water Separation.

The superhydrophilic/superoleophobic F-PETMP(30)/SiO_2(50) resin was selected for the fabrication of oil/water separation membranes. To compare the separation efficiency of our membranes with work that pioneered separations using superhydrophilic/superoleophilic coatings, the F-PETMP(0)SiO_2(50) was also selected for fabrication of separation membranes. Based on literature, we assumed that substrate porosity or mesh size would also influence the separation performance, thus, F-PETMP(30)/SiO_2(50) and F-PETMP(0)/ SiO_2(50) coatings were prepared on a series of substrates, including stainless steel mesh (with 200 mesh size), cotton cloth, and nylon filter membranes (with 0.8 and 0.45 μm pore size) to evaluate oil/water separation efficiency. The coatings on porous substrates were fabricated via spray deposition as previously described. The surface morphology of the F-PETMP(30)/SiO_2(50) coating on stainless steel mesh, cotton cloth, and nylon filter membranes were first studied by using SEM and TEM.

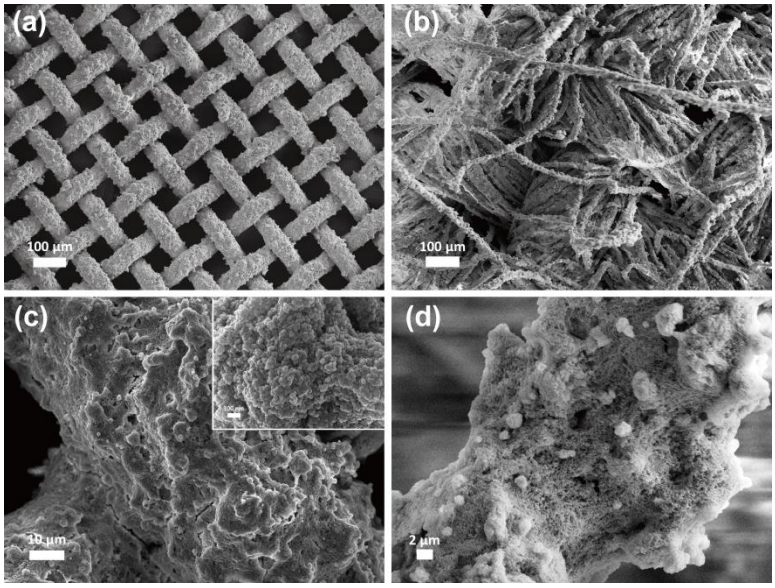

Figure 3.6 SEM micrographs of F-PETMP(30)/SiO_2(50).

a) Large-area view of the F-PETMP(30)/SiO_2(50) spray coated stainless steel mesh; b) enlarge view of a single cross of the F-PETMP(30)/SiO_2(50) spray coated stainless steel wire, the insert is the high magnification image of the surface morphology of the wire with the scale bare as 300 nm; c) Large-area view of the F-PETMP(30)/SiO_2(50) spray coated cotton cloth; (d) enlarge view of a single fiber of the F-PETMP(30)/SiO_2(50) spray coated cotton cloth.

Figure 3.6a shows the SEM image of F-PETMP(30)/SiO_2(50) prepared on a stainless steel mesh substrate. As shown, the coated stainless steel mesh maintained an open pore morphology. The average width of the mesh pores was approximately 50 µm which allows fast passage of liquid through the coated mesh. The enlarged SEM image in Figure 3.6b clearly shows that the mesh wire was evenly wrapped with the hybrid thiol-ene coating with hierarchically structured morphology similar to that previously observed on glass substrates. Figure 3.6c shows the SEM image of F-PETMP(30)/SiO_2(50) spray deposited on cotton cloth substrate. The coated textile exhibited a uniform and continuous surface with an evenly distributed coating. The cotton textile retains a porous structure with a uniform surface coverage on individual fibers, as shown in Figure 3.6d, which is beneficial for the separation application. As a

note, the F-PETMP(30)/SiO_2(50) and F-PETMP(0)/SiO_2(50) coatings displayed similar surface morphologies due to similar silica loading level.

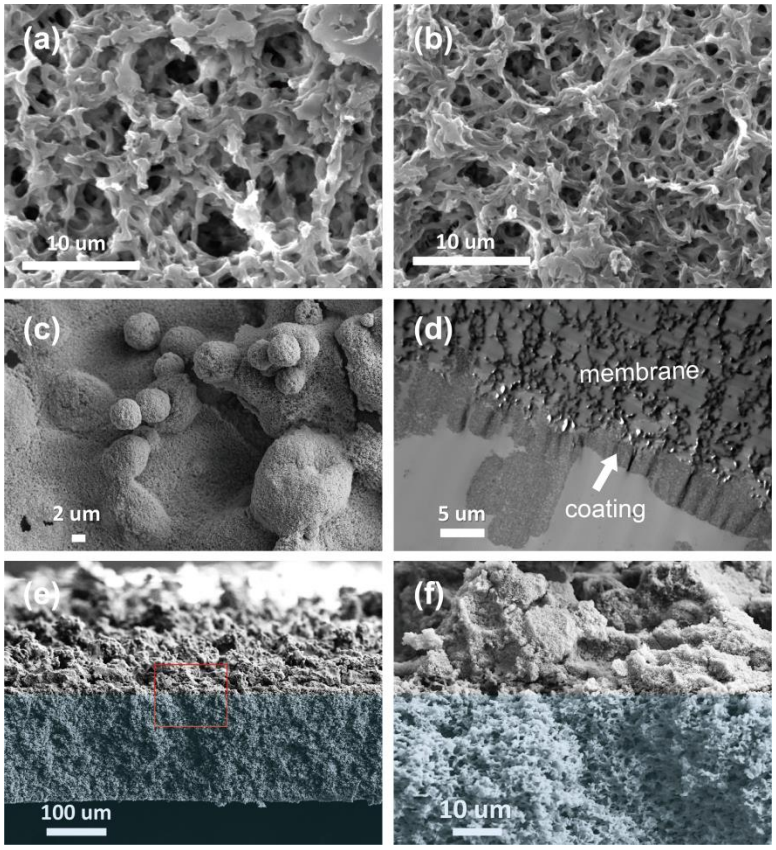

Figure 3.7 Morphology of the nylon membrane and sample PETMP(30)/SiO_2(50) coated film.

(a)SEM micrograph of nylon membrane with 0.8 μm pore size; **(b)** SEM micrograph of nylon membrane with 0.45 μm pore size; (c) Top image of sample F-PETMP(30)/SiO_2(50) on 0.45 μm pore size nylon membrane; (d) TEM image of cross-section view of F-PETMP(30)/SiO_2(50) spray coated nylon membrane; (e) and (f) SEM micrographs of cross-section of the spray coated nylon membrane. The nylon membrane was colored blue for clarity.

Figure 3.7 shows the SEM images for F-PETMP(30)/SiO_2(50) on nylon membrane substrates. Figure 3.7a and 3.7b show the typical surface morphology of the pristine porous nylon membrane with 0.8 μm and 0.45 μm pore size, respectively. As expected, the 0.45 μm membrane exhibits a smaller pore size compared to the 0.8 μm membrane. Figure 3.7c show the top view SEM image of F-PETMP(30)/SiO_2(50) spray

deposited on the 0.45 μm pore size nylon membrane, which exhibits the dual-scale hierarchical structure as discussed previously. The cross-section structure of the coated nylon membrane sample was studied by both TEM (Figure 3.7d) and SEM (Figure 3.7e-f). As shown in the micrographs, the spray coating covers the membrane, adding tortuosity to the liquid pathway, but does not block all the pores of the membrane which should enable the flow of liquid for the separation.

3.3.4.1 Separation of a Surfactant-Free Oil and Water Mixture.

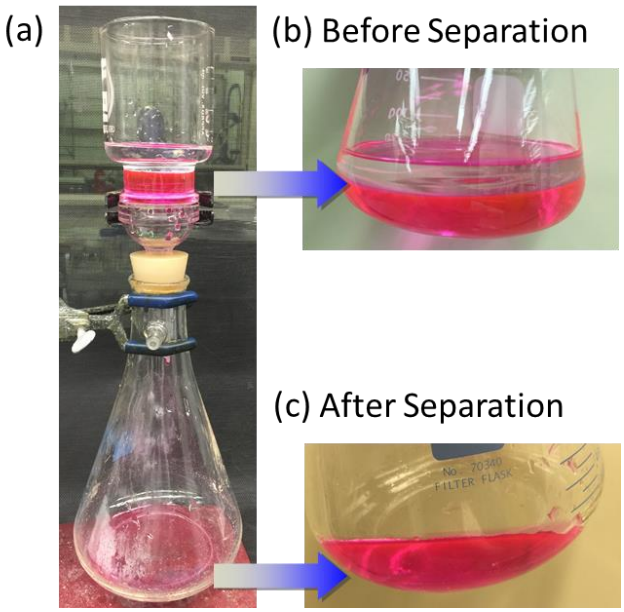

Figure 3.8 Photograph of the separation apparatus.

(a) Photograph of a simple oil/water separation apparatus with F-PETMP(30)/SiO_2(50) on a stainless steel mesh substrate. (b) Hexane and water (dyed pink) mixture before separation (c) water selectively permeated through the membrane without visible hexane in the collected water.

To evaluate the separation capability of the spray coated samples, we first conducted the experiments on a surfactant free hexane and water mixture. The water layer was dyed pink with Sulforhodamine B to improve the visibility of the separation process. The samples were prepared on stainless steel mesh, cotton cloth, and nylon

membranes substrates. To simplify the notation, we will represent the various results as mesh(0), cloth(0), 0.8 membrane(0) and 0.45 membrane(0) for F-PETMP(0)/SiO(50) on each substrate and mesh(30), cloth(30), 0.8 membrane(30) and 0.45 membrane(30) for F-PETMP(30)/SiO_2(50) on different substrates. The oil/ water separation study was carried out using the setup illustrated in Figure 3.8. The spray coated sample was fixed between the upper part and the bottom part of the funnel. Hexane and water were mechanically mixed together then poured into the glass funnel, no external force was applied. For sample F-PETMP(0)/SiO_2(50), the membranes were pre-wetted with water to allow water molecule saturate the film and intrinsically reject oil. .Figure 3.8b-c displays the result of F-PETMP(30)/ SiO_2(50) on a stainless steel mesh substrate. As shown, water passed through the membrane driven by gravity, whereas the hexane was rejected by the membrane and remained in the separation funnel. After separation, no visible hexane droplets were collected in the water. The separation efficiency was calculated by the following equation.

$$R\% = \frac{W_p}{W_o} * 100\% \quad \text{Equation (1)}$$

where W_o and W_p are the weight of water phase before and after separation. The calculated separation efficiencies (shown in Figure 3.9) for all of the samples were higher than 98% indicating a high separation capability for surfactant-free mixtures.

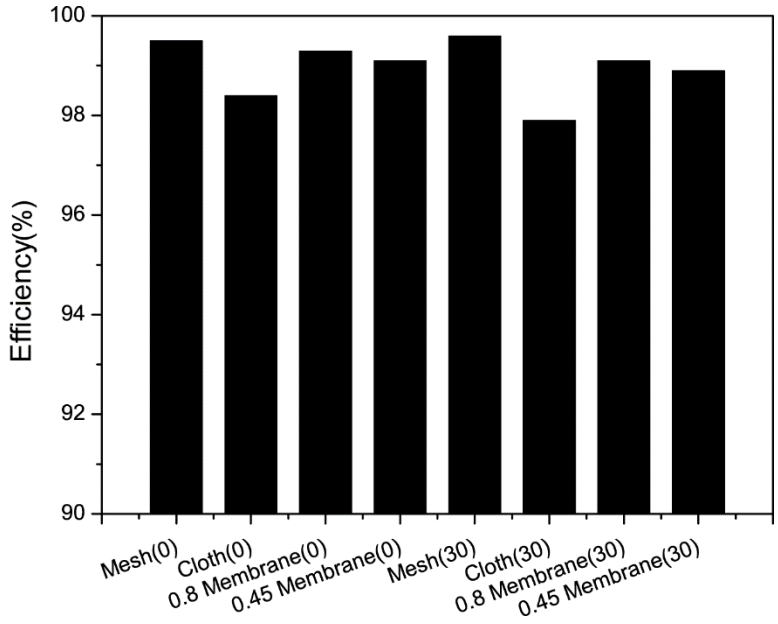

Figure 3.9 Separation efficiency of surfactant free oil/water mixture.

3.3.4.2 Separation of Oil-in-Water Emulsion.

Oil/water emulsions are more commonly encountered in the treatment of wastewater and are more difficult to separate compared to simple oil/water mixtures, where surfactant typically results in the oil being dispersed as small droplets within the aqueous phase. Membranes based on stainless steel mesh and cotton textile substrates were first investigated due to the high flux rate reported by others in literature on similar substrates.[8, 17, 27-28] The separation study was conducted using the same apparatus as illustrated previously (Figure 3.8). The toluene-in-water emulsion using SDS as the surfactant was poured into the funnel and the filtration was driven by gravity. As shown in Figure B2, the filtrate collected from the separations using membranes fabricated on stainless steel mesh and cotton cloth substrates exhibited a turbid appearance similar to the feed emulsion. Dynamic light scattering (DLS) was used to analyze the size and distribution of oil droplets in the emulsion before and after separation. The DLS data in

Figure B2(b) shows that the filtrates after separation contained a high concentration of oil droplets with sizes ranging from nanometers to several micrometers, and other than exhibiting different drop size distributions were similar to the original feed emulsion. The reason for the poor separation performance can be explained by the inability of the steel and cotton textile substrates to reject the emulsified droplets due to the large pore sizes. It should be noted that PETMP(0)/SiO_2(50) and PETMP(30)/SiO_2(50) coatings both provided poor separation performance.

To improve the separation performance, PETMP(0)/SiO_2(50) and PETMP(0)/SiO_2(50) coatings on nylon membrane substrates with 0.8 um and 0.45 um pore size were next investigated. The same separation set up was used; however, 30 KPa pressure was pulled on the receiving bottle. The filtrates obtained following the separation of the emulsion by the coated nylon membranes was analyzed with UV-VIS spectrometry. DLS analysis failed to provide reproducible results at low droplet concentrations. The absorbance peak of toluene at 261 nm was monitored to identify the oil concentration in the filtered emulsions. The water flux was calculated by measuring the time needed to completely pass a certain volume of toluene/water emulsion. The separation efficiency was determined according to a literature method.[29] The oil rejection coefficient R (%) was calculated by the following equation:

$$R\% = \frac{C_0 - C_p}{C_0} * 100\% \quad \text{Equation (2)}$$

where C_0 and C_p are the oil concentration in the original oil/water mixture and the collected water, respectively, which are calculated the change in absorbance of the characteristic toluene peak at 261 nm.

Figure 3.8a shows the UV-vis spectra for the feed emulsion and for the filtrates collected after separation on each of the modified nylon membranes. Using Equation 2, the absorbance values were converted into separation efficiencies (%), as shown in Figure 3.8b. Flux values are also provided in Figure 3.8b. For both F-PETMP(0)/SiO_2(50) and F-PETMP(30)/SiO_2(50) coatings, decreasing the pore size of the membrane resulted in improved efficiency, but at the expense of decreased flux. For each pore size, F-PETMP(30) shows a higher efficiency and lower flux compared to F-PETMP(0); this can be attributed to the fluorinated constituent of the coating which provides and increased rejection rate emulsified oil droplets. The pores in the membrane substrate provide pathways for water permeation. With an external force applied below breakthrough pressure, the larger pore size allows for greater flux and a greater possibility that small emulsified oil droplets pass through the membrane resulting in decreased separation efficiency. The F-PETMP(30)/SiO_2(50) coating on the 0.45 um nylon substrate provide the best separation performance at 95.4% with a flux at 529.31 $Lm^{-2}h^{-1}$. While flux decreased, these values are still higher than conventional ultrafiltration membranes (300 L m^{-2} h^{-1}). [30] Optical microscope was used to confirm the separation efficiencies by imaging the original feed emulsion and the collected filtrate. As shown in Figure 3.8c, micrometer and submicrometer oil droplets were observed in the feed emulsion, while no droplets were observed in the collected filtrate after passing through the F-PETMP(30)/SiO_2(50) modified 0.45 um nylon substrate.

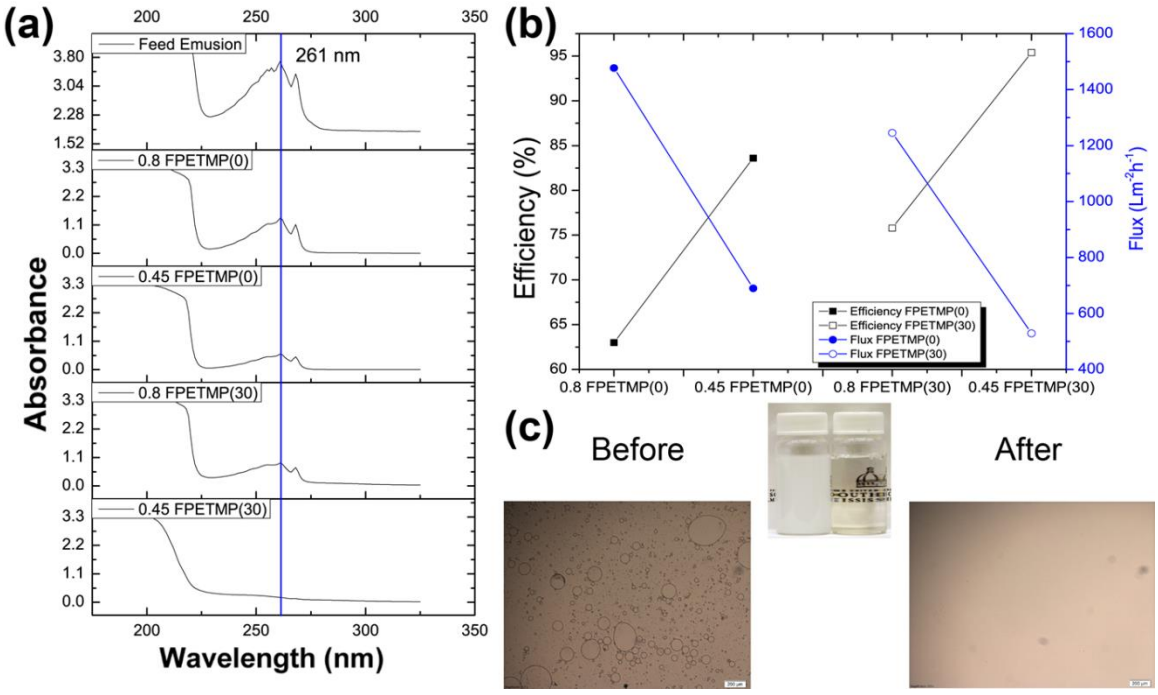

Figure 3.10 Separation results for toluene-in-water emulsion.

(a) UV-VIS spectra of the toluene-in-water emulsion before separation and after separation; (b) separation efficiency and flux of a serial sample in terms of the oil rejection and permeate flux; (c) Photograph and optical images of feed emulsion and filtrate separated by 0.45 F sample.

3.3.4.3 Dye contained Oil/Water emulsion Separation.

The separation of dye containing oily industrial wastewater is extremely important due to the toxicity of dye to environment. However, little work has been reported on the performance of superwetting/antiwetting membranes towards the separation of dye-contaminated oil/water industrial waste streams. To evaluate the separation capability of our underwater and in-air superoleophobic coatings applied to such systems, similar separation experiments, as previously described, were conducted using Nile Red/hexadecane emulsified in water with SDS as feed emulsions. The separated emulsion was analyzed by UV-VIS spectrometry by monitoring the absorbance

peak of Nile Red at 574 nm, and the separation efficiency was calculated based on the absorbance changes before and after separation.

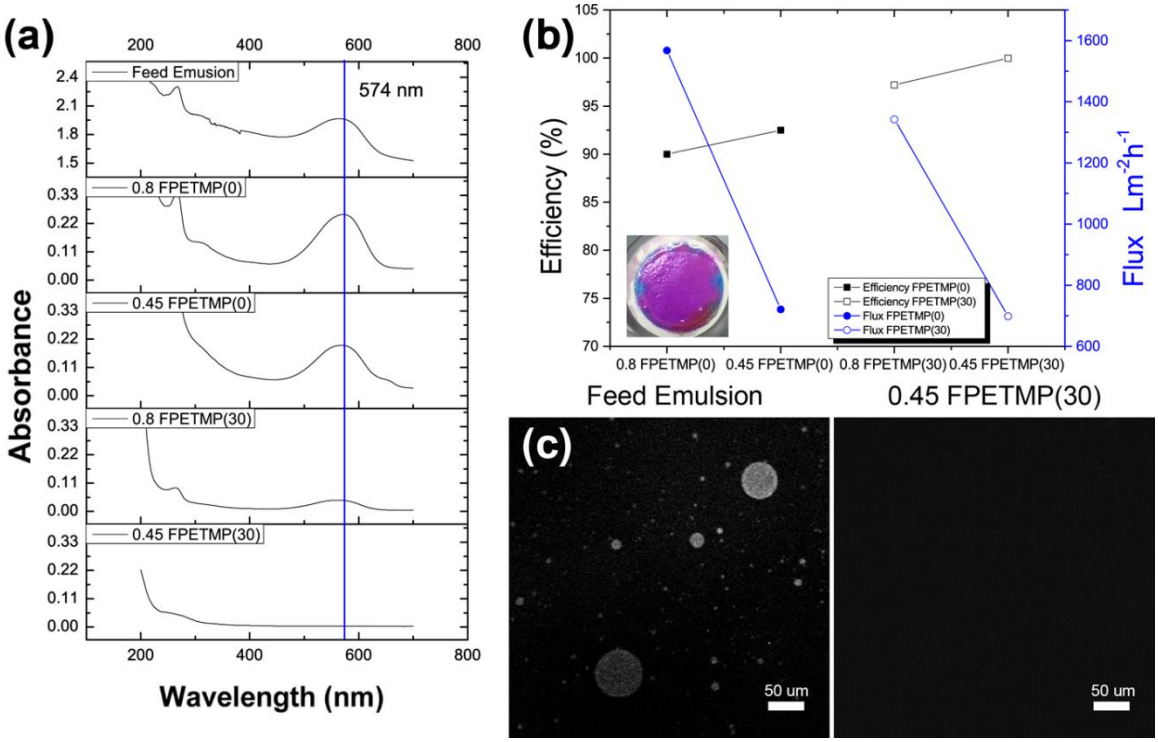

Figure 3.11 Separation results for dye contained oil/water emulsion.

(a) UV-VIS spectra of the hexadecane and Nile Red -in-water emulsion before separation and after separation; (b) separation efficiency of a serial samples in term of the oil rejection; (c) confocal microscope images of feed emulsion and collected water separated by 0.45 F-PETMP(30).

As shown in UV-VIS spectra in Figure 3.9a, the absorbance peak of Nile Red decreased after separation compared with the original feed emulsion. The calculated separation efficiencies showed similar trends as previously described for separation of toluene in that emulsions separated by modified 0.45 μm membranes exhibited higher efficiencies than emulsions separated by modified 0.8 μm membranes. The F-PETMP(30)/SiO_2(50) formulation again had higher oil rejection compared with the non-fluorinated F-PETMP(0)/SiO_2(50). The optical image in Figure 3.9b (inset) shows the material (hexadecane and dye) remaining on the membrane after separation with the 0.45

μm F-PETMP(30) membrane. The F-PETMP(30)/SiO_2(50) on 0.45 μm nylon substrate provided a 99.98% separation efficiency 99.98%. The confocal microscope image in Figure 3.9c shows a broad size distribution of emulsion droplets prior to separation, while after separation an absence of fluorescence indicates a high efficiency of removing oil and dye from the emulsion.

3.4 Conclusions

A unique superhydrophilic/superoleophobic coating has been successfully fabricated via spray deposition of a fluorinated thiol-acrylate resin containing hydrophilic silica nanoparticles. The spray deposition method with inorganic NPs was used to fabricate surfaces with a hierarchically rough morphology. The synergistic contributions from the chemical composition and the textured surface provided coatings that display extreme repellency toward non-polar liquids (i.e. hexadecane, vegetable oil), but strong affinity to water. The performance of these superhydrophilic/superoleophilic and superhydrophilic/superoleophobic coatings as separation membranes were evaluated in the separation of oil/water emulsions and dye containing oil/water emulsions. The results showed that the superhydrophilic/superoleophobic membrane results in >99 % oil rejection when paired with substrates containing 0.45 μm pore sizes. A salient feature of the fabrication process is scalability to large area substrates. These results suggest potential application of these modified membranes in the treatment of oil spills and industrial wastewater streams.

3.5 References

1. Schrope, M., A Scientist at the Centre of the Spill. *Nature* **2010,** *466*, 680-684.
2. Sato, T.; Qadir, M.; Yamamoto, S.; Endo, T.; Zahoor, A., Global, Regional, and Country Level Need for Data on Wastewater Generation, Treatment, and Use. *Agr Water Manage* **2013,** *130*, 1-13.
3. Li, W. W.; Yu, H. Q.; Rittmann, B. E., Reuse Water Pollutants. *Nature* **2015,** *528*, 29-31.
4. Cheryan, M.; Rajagopalan, N., Membrane processing of oily streams. Wastewater treatment and waste reduction. *J Membrane Sci* **1998,** *151* (1), 13-28.
5. Marrot, B.; Barrios-Martinez, A.; Moulin, P.; Roche, N., Industrial Wastewater Treatment in a Membrane Bioreactor: A review. *Environ. Prog.* **2004,** *23* (1), 59-68.
6. Zhu, Y. Z.; Wang, D.; Jiang, L.; Jin, J., Recent Progress in Developing Advanced Membranes for Emulsified Oil/Water Separation. *Npg Asia Mater.* **2014,** *6*.
7. Feng, L.; Zhang, Z.; Mai, Z.; Ma, Y.; Liu, B.; Jiang, L.; Zhu, D., A Super-Hydrophobic and Super-Oleophilic Coating Mesh Film for the Separation of Oil and Water. *Angewandte Chemie* **2004,** *116* (15), 2046-2048.
8. Cheng, Z.; Wang, J.; Lai, H.; Du, Y.; Hou, R.; Li, C.; Zhang, N.; Sun, K., pH-Controllable On-Demand Oil/Water Separation on the Switchable Superhydrophobic/Superhydrophilic and Underwater Low-Adhesive Superoleophobic Copper Mesh Film. *Langmuir* **2015,** *31* (4), 1393-9.
9. Gondal, M. A.; Sadullah, M. S.; Dastageer, M. A.; McKinley, G. H.; Panchanathan, D.; Varanasi, K. K., Study of factors governing oil-water separation process using TiO(2) films prepared by spray deposition of nanoparticle dispersions. *ACS Appl Mater Interfaces* **2014,** *6* (16), 13422-9.
10. Chen, P. C.; Xu, Z. K., Mineral-Coated Polymer Membranes with Superhydrophilicity and Underwater Superoleophobicity for Effective Oil/Water Separation. *Sci. Rep.* **2013,** *3*, 2776.
11. Liu, M. J.; Wang, S. T.; Wei, Z. X.; Song, Y. L.; Jiang, L., Bioinspired Design of a Superoleophobic and Low Adhesive Water/Solid Interface. *Adv. Mater.* **2009,** *21* (6), 665-+.
12. Xue, Z.; Wang, S.; Lin, L.; Chen, L.; Liu, M.; Feng, L.; Jiang, L., A Novel Superhydrophilic and Underwater Superoleophobic Hydrogel-Coated Mesh for Oil/Water Separation. *Adv. Mater.* **2011,** *23* (37), 4270-3.
13. Brown, P. S.; Bhushan, B., Mechanically Durable, Superoleophobic Coatings Prepared by Layer-by-Layer Technique for Anti-Smudge and Oil-Water Separation. *Sci. Rep.* **2015,** *5*, 8701.
14. Kota, A. K.; Kwon, G.; Choi, W.; Mabry, J. M.; Tuteja, A., Hygro-Responsive Membranes for Effective Oil-Water Separation. *Nat. Commun.* **2012,** *3*, 1025.
15. Xu, Z.; Zhao, Y.; Wang, H.; Wang, X.; Lin, T., A Superamphiphobic Coating with an Ammonia-Triggered Transition to Superhydrophilic and Superoleophobic for Oil-Water Separation. *Angew. Chem. Int. Ed. Engl.* **2015,** *54* (15), 4527-30.
16. Yoon, H.; Na, S. H.; Choi, J. Y.; Latthe, S. S.; Swihart, M. T.; Al-Deyab, S. S.; Yoon, S. S., Gravity-Driven Hybrid Membrane for Oleophobic-Superhydrophilic Oil-Water Separation and Water Purification by Graphene. *Langmuir* **2014,** *30* (39), 11761-9.
17. Yuan, T.; Meng, J.; Hao, T.; Wang, Z.; Zhang, Y., A Scalable Method toward Superhydrophilic and Underwater Superoleophobic PVDF Membranes for Effective Oil/Water Emulsion Separation. *ACS Appl. Mater. Interfaces* **2015,** *7* (27), 14896-904.
18. Zhang, W.; Zhu, Y.; Liu, X.; Wang, D.; Li, J.; Jiang, L.; Jin, J., Salt-Induced Fabrication of Fuperhydrophilic and Underwater Superoleophobic PAA-g-PVDF Membranes for Effective Separation of Oil-in-Water Emulsions. *Angew. Chem. Int. Ed. Engl.* **2014,** *53* (3), 856-60.

19. Zhu, Y. Z.; Zhang, F.; Wang, D.; Pei, X. F.; Zhang, W. B.; Jin, J., A novel zwitterionic polyelectrolyte-grafted PVDF membrane for thoroughly separating oil from water with ultrahigh efficiency. *J Mater Chem A* **2013,** *1* (18), 5758-5765.
20. Yang, J.; Zhang, Z. Z.; Xu, X. H.; Zhu, X. T.; Men, X. H.; Zhou, X. Y., Superhydrophilic-superoleophobic coatings. *J Mater Chem* **2012,** *22* (7), 2834-2837.
21. Brown, P. S.; Bhushan, B., Bioinspired, Roughness-Induced, Water and Oil Super-philic and Super-phobic Coatings Prepared by Adaptable Layer-by-Layer Technique. *Sci. Rep.* **2015,** *5*, 14030.
22. Sparks, B. J.; Hoff, E. F. T.; Xiong, L.; Goetz, J. T.; Patton, D. L., Superhydrophobic Hybrid Inorganic-Organic Thiol-ene Surfaces Fabricated via Spray-Deposition and Photopolymerization. *ACS Appl. Mater. Interfaces* **2013,** *5* (5), 1811-1817.
23. Xiong, L.; Kendrick, L. L.; Heusser, H.; Webb, J. C.; Sparks, B. J.; Goetz, J. T.; Guo, W.; Stafford, C. M.; Blanton, M. D.; Nazarenko, S.; Patton, D. L., Spray-Deposition and Photopolymerization of Organic-Inorganic Thiol-ene Resins for Fabrication of Superamphiphobic Surfaces. *ACS Appl. Mater. Interfaces* **2014,** *6* (13), 10763-10774.
24. Shin, J.; Nazarenko, S.; Hoyle, C. E., Effects of Chemical Modification of Thiol-Ene Networks on Enthalpy Relaxation. *Macromolecules* **2009,** *42* (17), 6549-6557.
25. Xiong, L.; Kendrick, L. L.; Heusser, H.; Webb, J. C.; Sparks, B. J.; Goetz, J. T.; Guo, W.; Stafford, C. M.; Blanton, M. D.; Nazarenko, S.; Patton, D. L., Spray-Deposition and Photopolymerization of Organic–Inorganic Thiol–ene Resins for Fabrication of Superamphiphobic Surfaces. *ACS Applied Materials & Interfaces* **2014,** *6* (13), 10763-10774.
26. Sparks, B. J.; Hoff, E. F. T.; Xiong, L.; Goetz, J. T.; Patton, D. L., Superhydrophobic Hybrid Inorganic–Organic Thiol-ene Surfaces Fabricated via Spray-Deposition and Photopolymerization. *ACS Applied Materials & Interfaces* **2013,** *5* (5), 1811-1817.
27. Liu, N.; Cao, Y.; Lin, X.; Chen, Y.; Feng, L.; Wei, Y., A Facile Solvent-Manipulated Mesh for Reversible Oil/Water Separation. *ACS Appl. Mater. Interfaces* **2014,** *6* (15), 12821-6.
28. Padaki, M.; Murali, R. S.; Abdullah, M. S.; Misdan, N.; Moslehyani, A.; Kassim, M. A.; Hilal, N.; Ismail, A. F., Membrane technology enhancement in oil-water separation. A review. *Desalination* **2015,** *357*, 197-207.
29. Wang, G.; He, Y.; Wang, H.; Zhang, L. Y.; Yu, Q. Y.; Peng, S. S.; Wu, X. D.; Ren, T. H.; Zeng, Z. X.; Xue, Q. J., A cellulose sponge with robust superhydrophilicity and underwater superoleophobicity for highly effective oil/water separation. *Green Chem* **2015,** *17* (5), 3093-3099.
30. Chen, P. C.; Xu, Z. K., Mineral-coated polymer membranes with superhydrophilicity and underwater superoleophobicity for effective oil/water separation. *Sci Rep* **2013,** *3*, 2776.

3.6 Appendix - Superhydrophilic/Superoleophobic Surface Via Spray Deposition and Thiol-Acrylate Photopolymerization for Oil/Water Separation

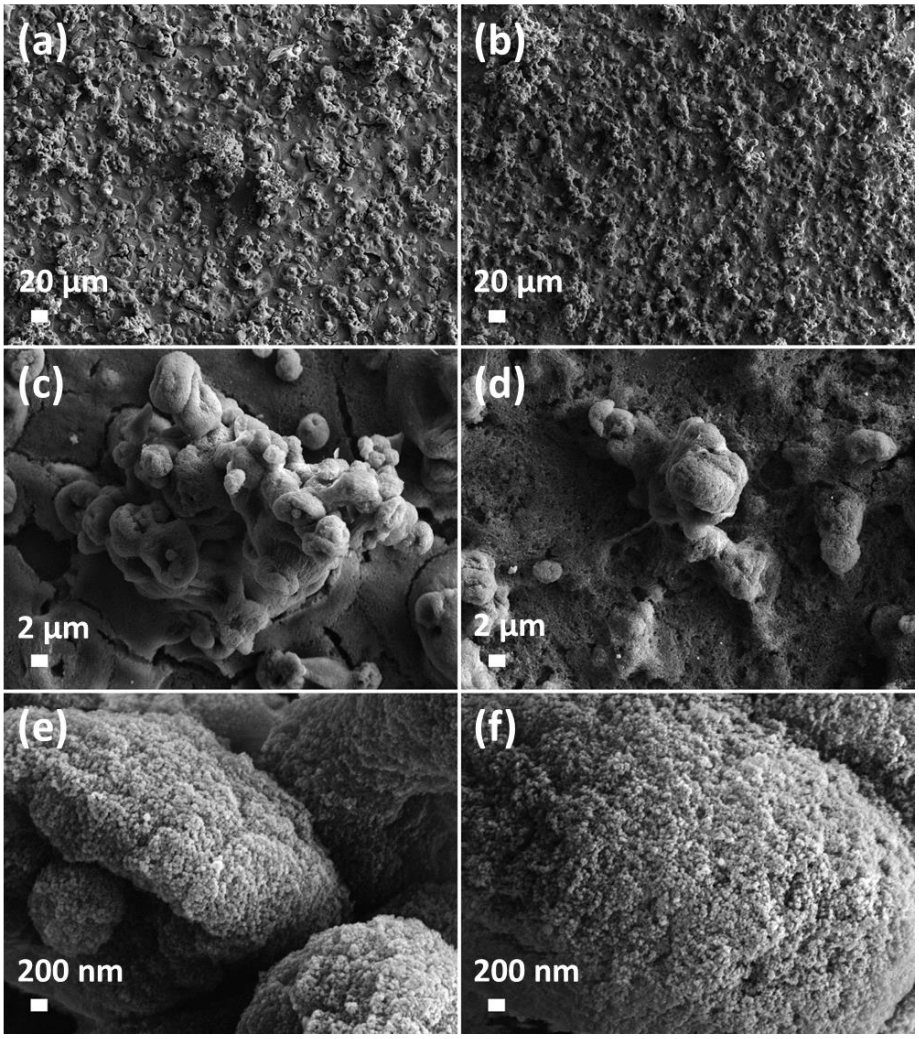

Figure A.5 SEM micrographs of FPETMP(0)/SiO_2(50) (a,c,e) and FPETMP(30)/SiO_2(50) (b,d,f) at (a,b) 200X, (c,d) 2000X, and (e,f) 20,000X magnification.

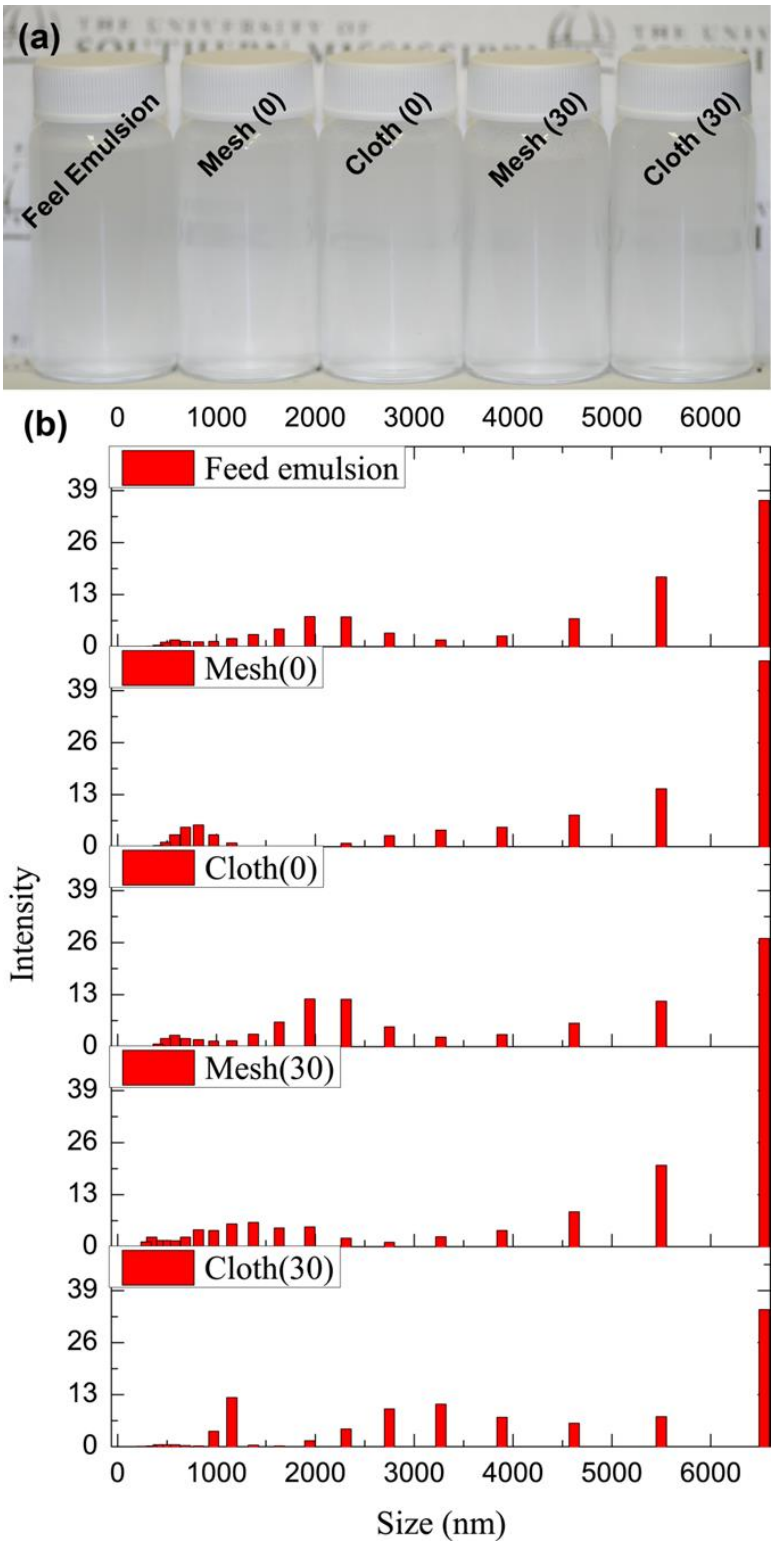

Figure A.6 (a) Digital image of the separation results. (b) Dynamic light scattering (DSL) spectra of the feed emulsion, filtrate separated by mesh and cloth.

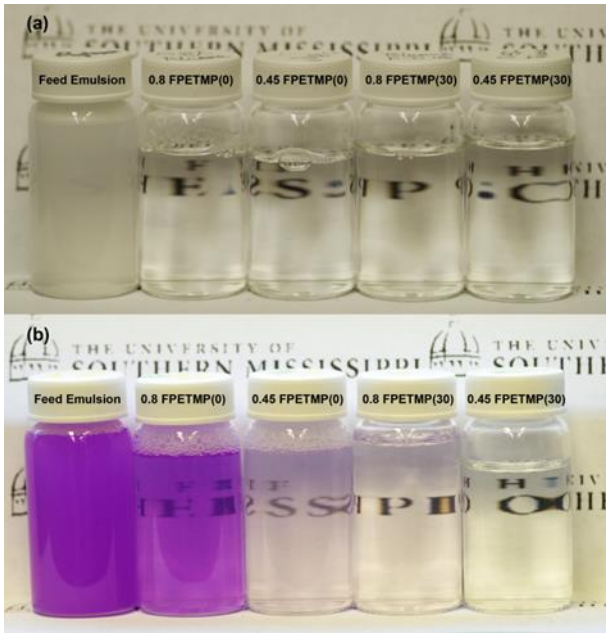

Figure A.7 Optical image of separation results (a) oil/water emulsion mixture, (b) dye contained oil/water emulsion mixture.

CHAPTER IV – THIOL-ENE SUPERHYDROPHOBIC COATING WITH ENHANCED HIERARCHICAL MORPHOLOGY BY POROGEN LEACHING TECHNIQUE

4.1 Introduction

Bioinspired superhydrophobic surfaces with a static water contact angle higher than 150° and a contact angle hysteresis lower than 10° have attracted tremendous attention in past decades within industry and academia due to many promising practical applications such as self-cleaning, anti-fouling, anti-icing, and anti-corrosion coatings. It has been well established that the superhydrophobic wetting state is governed by two factors: surface chemical composition and surface roughness.[1] Decreasing the surface energy by eliminating high surface energy moieties and increasing the surface roughness by introducing a multi-scale hierarchical topography provides a facile route to achieve superhydrophobicity. Many physical and chemical methods have been reported to successfully create superhydrophobic surfaces with a multi-scale hierarchical surface structure, including surface templating,[2-3] etching,[4-5] electrospinning,[6-7] sol-gel,[8-9] vapor deposition[10-11] and spray deposition.[12-13] Among these approaches, spray deposition is one of the most advantageous methods because of its simplicity, facile processing, economy of the apparatus and raw materials, and the ability to scale up from bench to pilot plant. Spray deposition is an atomization process that enables the facile deposition of low surface tension polymeric resins containing inorganic nano-sized additives. The atomization and evaporation process creates a micrometer-scale corpuscular morphology overlaid by a nano-scale roughness that arises from additives with high specific surface area such as SiO_2,[13-14] TiO_2[15-16] and CNT.[12, 17] This dual scale roughness at the polymer-

air interfaces effectively traps air pockets between water droplets and the solid surface to endow the surface with superhydrophobicity. The incorporation of high loading levels of the nano-scale additives, however, yields coatings with poor mechanical stability – a primary reason superhydrophobic technologies have been limited in practical applications. Additionally, high loading levels of nano-additives drastically increase the viscosity of the polymer precursor solution leading to challenges with nanoparticle dispersion and difficulties with the spray deposition process (low flow, clogged spray nozzles, etc.). Approaches that reduce the nanoparticle loading level in the resin are needed to improve the mechanical robustness of the coatings and to address the processing challenges.

The porogen leaching technique has been widely used to fabricate mechanically robust, highly porous materials with large surface/volume ratios across many areas of interest, including tissue engineering,[18-21] separation membranes,[22] and antireflection coatings.[23] Various methodologies directed at preparing porous polymers have been reported in recent years, including direct and indirect templating, block copolymer self-assembly, and direct synthesis methodologies.[24-25] The indirect methodology typically involves processing (e.g. molding, casting, etc.) a mixture of polymer containing a well-dispersed sacrificial template as the porogen. Common materials employed as porogens include immiscible solvents, salts, particles, and polymers, which can be extracted from the matrix after film formation using either evaporation or solvents selective for the dissolution of the porogen. The size, shape, structure, and distribution of the pores can be controlled by tuning the properties of the porogen, the interactions between the porogen and matrix, and the weight or volume fraction of the porogen. Recently, Levkin and coworkers explored the porogen approach for the fabrication of superhydrophobic

surfaces. The method involved in situ polymerization of common dimethacrylate monomers in the presence of a porogenic solvents (e.g. decanol and cyclohexanol). The use of porogen solvents in the monomer resin resulted in polymerization induced phase separation, which upon removal of the porogen solvent, afforded highly porous surfaces with a combination of micro- and nanoscale roughness that exhibited superhydrophobic wetting. Liu and coworkers reported a similar route to superhydrophobic surfaces using co-porogenic solvents (1,4-butanediol and N-methyl-2-pyrrolidone) and polymerization induced phase separation.[31] The surface morphology and wetting properties of the molded films were tuned by controlling the co-porogen ratio in the dimethacrylate monomer resin. While the use of porogenic solvents provides a facile route to superhydrophobic surfaces, film processing has been limited to molding due to the necessity to carefully control or prevent evaporation of the porogen constituent prior to polymerization.

Herein, we present a facile process to produce superhydrophobic surfaces using poly(dimethylsiloxane) (PDMS) as a polymeric porogen for photo-curable thiol-ene resins. Removal of the PDMS with a simple solvent wash provides multi-scale hierarchically structured surfaces that exhibit static water contact angles greater than 150°. Importantly, the superhydrophobic wetting state is achieved with resins containing 50% less silica nanoparticles relative our previously reported work.[29-30]

4.2 Experimental Section

4.2.1 Materials.

All reagents were obtained at the highest purity available and used without further purification unless otherwise specified. 2,4,6,8-tetramethyl-2,4,6,8-

tetravinylcyclotetrasiloxane (TMTVSi), 1,3,5-triallyl-1,3,5-triazine-2,4,6 (1H, 3H, 5H) trione (TTT), 2,2-dimethoxy-2-phenylacetophenone (DMPA), poly(dimethylsiloxane) (PDMS) and acetone were obtained from Sigma-Aldrich, glycol dimercaptoacetate (GDMP) was obtained from Bruno Bock. Aerosil R972, hydrophobic fumed silica with trimethylsilyl surface functionalization and an average primary particle size of 16 nm was kindly provided by Evonik Industries.

4.2.2 Characterization.

Contact angle measurements were performed using a Rame-Hart 200-00 Std.-Tilting B. goniometer. Static contact angles were measured using 6 μL water droplets. ImageJ Drop Analysis was used to analyze the droplets. Scanning electron microscopy (SEM) images were obtained using a Zeiss Sigma VP FEG-SEM at 10 kV in high vacuum mode. All reactions were performed under ambient conditions.

4.3 Results and Discussion

4.3.1 Film Fabrication and Initial Assessment of the Wetting Behavior.

When developing the appropriate resin for the porogen approach to superhydrophobic surfaces, we considered the following criteria as key requirements for the choice of porogen material. First, the porogen has to be inert to the photopolymerization process and should not undergo reaction with the polymer network. Second, the porogen must exhibit low volatility to avoid evaporation during or after the spray deposition process. Finally, and perhaps most importantly, the porogen must be extractable by a selective solvent that does not swell the cured polymer film. In our case, methyl-terminated polydimethylsiloxane was chosen as a porogen that met the aforementioned criteria, exhibited good affinity for the trimethylsilyl-terminated SiO_2

nanoparticles, and displayed immiscibility with the resin in the absence of solvent and/or upon polymerization. PDMS samples with various molecular weights (700, 7000, 14,000, and 140,000 g/mol) were employed as porogens. For thiol-ene resins, two multifunctional enes, 2,4,6,8-tetramethyl-2,4,6,8-tetravinylcyclotetrasiloxane (TMTVSi) and 1,3,5-triallyl-1,3,5-triazine-2,4,6 (1H, 3H, 5H) trione (TTT), were used to study the effect of thiol-ene resin on morphology and wettability. To simplify the notation for each resin system, formulations in this chapter are abbreviated as PDMS-M(x)/SiO_2(y), where M*1000 represents the molecular weight of the PDMS, x represents the wt % PDMS and y represents the wt % SiO_2, respectively.

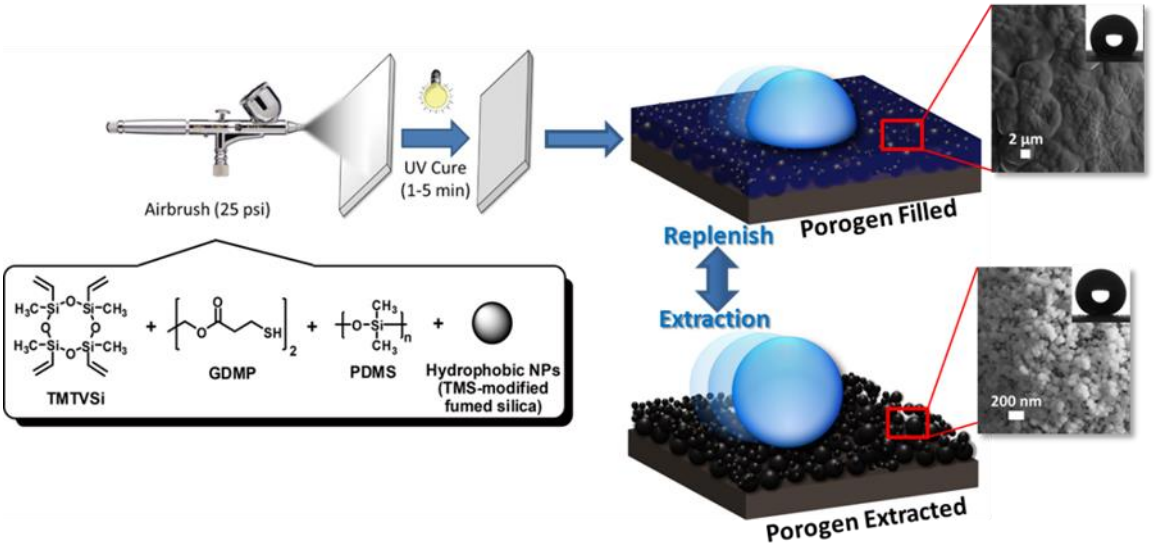

Scheme 4.1 Schematic of the spray deposition and porogen leaching process via thiol-ene photopolymerization

As shown in Scheme 4.1, superhydrophobic coatings were prepared by a sequential spray-cure-extraction process. An acetone-based suspension containing 2,4,6,8-tetramethyl-2,4,6,8-tetravinylcyclotetrasiloxane (TMTVSi), glycol dimercaptoacetate (GDMP), PDMS, hydrophobic trimethylsilyl-modified SiO_2

nanoparticles, and 2,2-dimethoxy-2-phenylacetophenone (DMPA, photoinitiator) was sprayed onto clean glass slides. The acetone solvent rapidly volatilizes during the spray deposition process. The samples were then exposed to UV light (λ_{max} = 365 nm) at an intensity of 25 mW/cm2 for 3 min to induce photopolymerization. After photopolymerization, the films were washed briefly with hexane to extract the PDMS porogen from the surface.

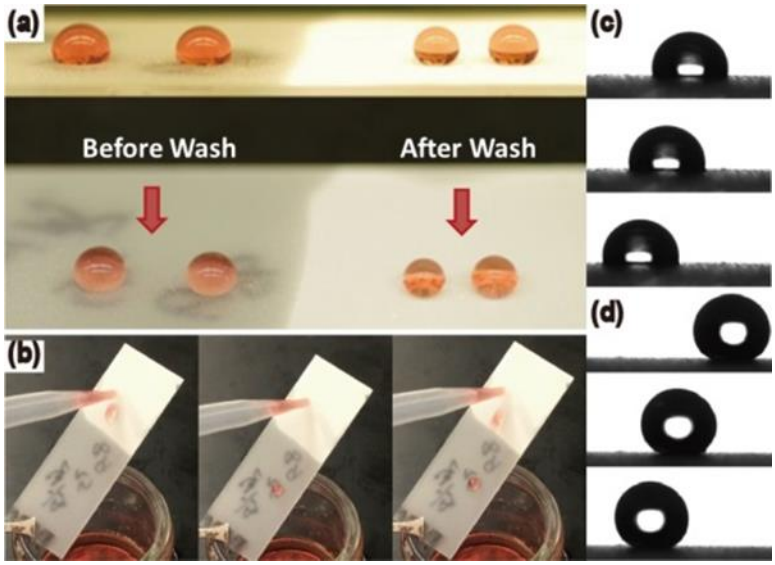

Figure 4.1 Wetting behavior of TMTVSi/GDMP PDMS(50)/SiO_2(15) before and after leaching process.

(a) Digital images of side and top view of TMTVSi/GDMP PDMS(50)/SiO_2(15) before (left side) and after (right side) leaching process, (b), (c), and (d) Video snapshot images of water move differently on left side and right side of sample PDMS(50)/SiO_2(15)

A qualitative assessment of the wetting properties of the TMTVSi/GDMP PDMS-M(x)/SiO_2(y) film before and after extraction is shown in Figure 4.1. As shown in Figure 4.1a, the film prior extraction was semi-transparent, while the film after wash was opaque. The difference in transparency is due to light scattering by the micron and submicron voids that result from PDMS extraction. The surface displayed a slippery hydrophobic wetting state before PDMS extraction and transitioned to a superhydrophobic wetting

state after extraction. The difference in wetting states of the non-extracted and extracted surfaces are more easily observed in digital image snapshots shown in Figure 4.1b-c. On a tilted sample, water droplets rapidly slide on the side of the extracted film showing no sign of adhesion to the substrate, while the water droplets slide relatively slow on the film prior to extraction. Insight into the surface morphology and a more qualitative assessment of the wetting behaviors before and after extraction are described in the following sections.

4.3.2 Influence of Thiol-ene Resin Composition on Surface Morphology and Wetting.

TTT, a multifunctional alkene widely used in thiol-ene chemistries, was compared with TMTVSi in the thiol-ene formulations. TMTVSi has a structure similar to that of the PDMS and is expected to be more compatible and miscible with the PDMS porogen resulting in a more homogeneous distribution of the porogen throughout the film following photopolymerization. Following photopolymerization, the films were characterized by SEM and WCA. Figures 4.2a-c show the SEM images at different magnifications of the surface prepared from the PDMS-7(40)/SiO_2(15) TTT-GDMP formulation after the extraction process. As shown in Figure 4.2a, randomly distributed resin aggregates with micrometer scale pores were observed on the surface. The aggregations are the result of the spray process and the pores arise from the removal of the porogen. At higher magnification (Figure 4.2b and 4.2c), a fairly smooth surface morphology without significant porosity or roughness on the nanometer scales was observed. The TTT-GDMP PDMS-7(40)/SiO_2(15) coatings exhibited a water contact angle of 133.4±1.2° and the water droplets were strongly pinned on the surface even when the substrate was tilted upside down. The failure to achieve the superhydrophobic

wetting state can be attributed to the absence of a hierarchical roughness – particularly at the nanometer scale. Figures 4.2d-f show the SEM images of sample PDMS-7(40)/SiO_2(15) TMTVSi-GDMP based resin after PDMS extraction.

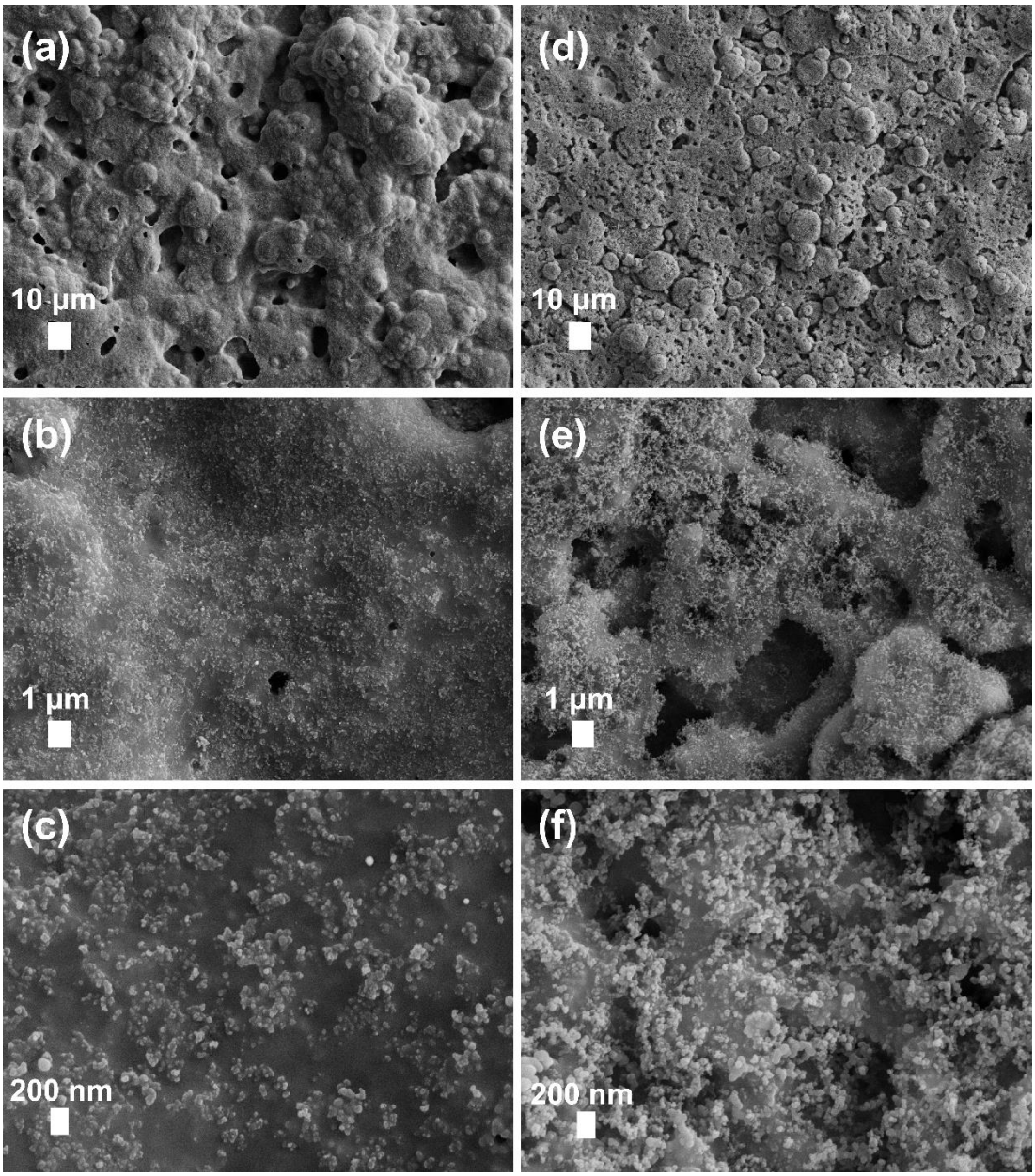

Figure 4.2 Scanning electron micrographs of samples PDMS-7(40)/SiO_2(15).

(a, b, c) with resin TTT-GDMP and (d, e, f) TMTVSiat 500x, 5,000x and 20,000x magnification.

Compared to the TTT-GDMP resin, the PDMS-7(40)/SiO_2(15) TMTVSi-GDMP surface exhibited a highly porous morphology at both micrometer and submicrometer size scales. At higher magnification (Figure 4.2e and 4.2f), a porous surface structure with microscale connectivity of the pores was observed. These features were overlaid with a nanometer scale roughness likely arising from a combination of the PDMS extraction and the presence of silica nanoparticles at the interface. The wide distribution of pores after extraction indicates that PDMS forms well-distributed microphase domains after solvent evaporation and during the UV-polymerization process. The similar chemical structures of TMTVSi, PDMS, and TMS-terminated SiO_2 nanoparticles yield similar affinities between NPs/PDMS and NPs/polymer resulting in the enrichment of NPs at the interface. The combination of micrometer and nanometer scale features resulted in a hierarchical structure that allows the surface to trap air between the solid substrate and liquid droplet giving rise to superhydrophobicity, as indicated by the observed water contact angle at 162.7±0.6° and low contact angle hysteresis at 1°±0.5.

4.3.3 Influence of PDMS Porogen Concentration and Molecular Weight on Surface Morphology and Wetting.

Given the outcome of the comparison of TTT versus TMTVSi, we focused only on the TMTVSi/GDMP resin from this point forward. To investigate the influence of the porogen concentration, samples were fabricated containing different concentrations of the 0.7K PDMS. The surface morphology of the cured coatings was investigated by SEM before and after PDMS extraction. Figures 4.3a-d show the SEM images (5000x magnification) of surfaces fabricated with 0 wt.%, 10 wt.%, 20 wt.%, and 40 wt% PDMS-0.7, respectively, before extraction of the porogen. Samples prepared without any

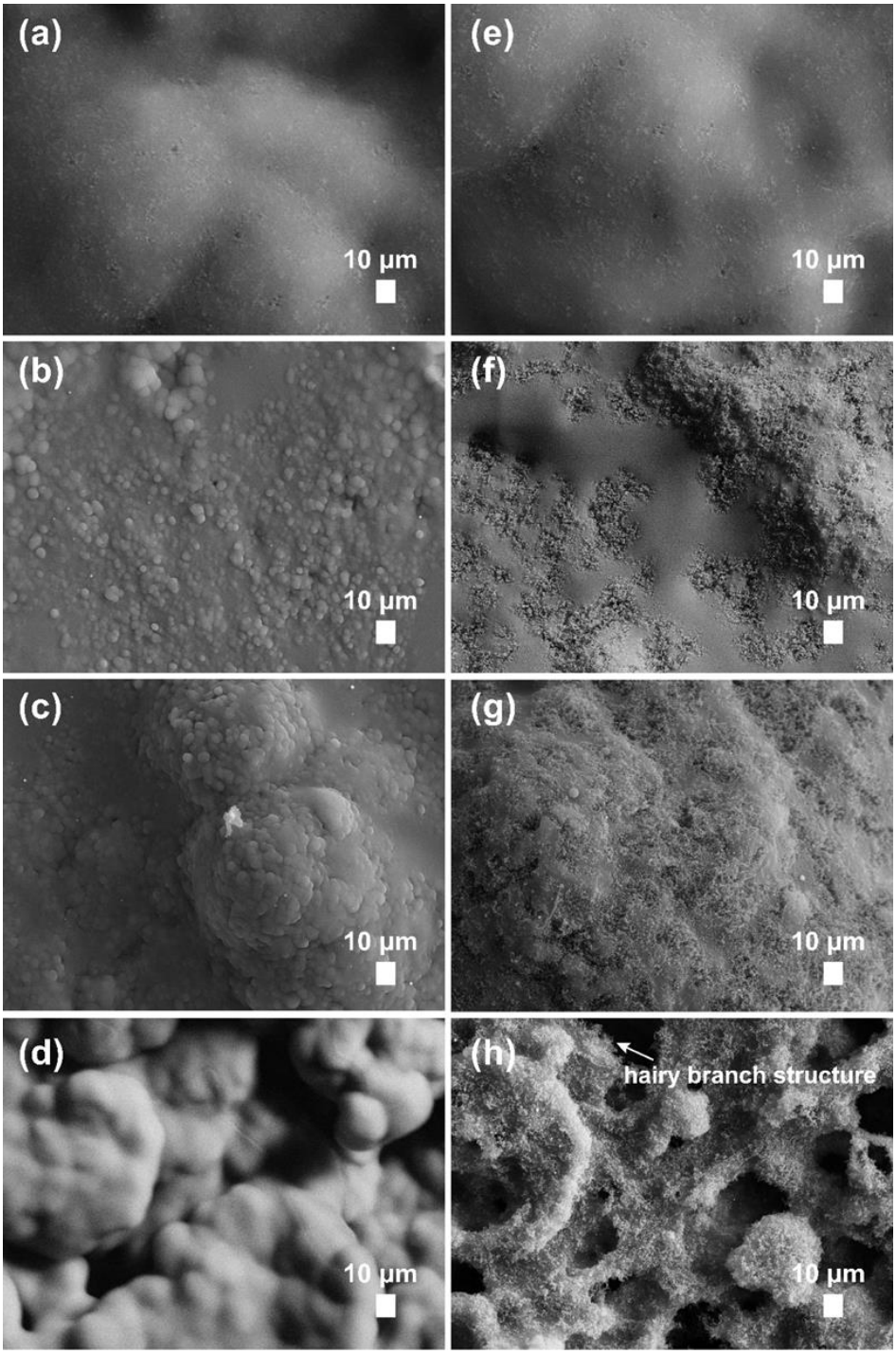

Figure 4.3 SEM images of surfaces fabricated with various amount of PDMS before and after extraction.

(a,e) 0 wt.%, (b,d) 10 wt.%, (c,f) 20 wt.%, and (e,g) 40 wt% PDMS-0.7, respectively. (a,b,c,d) represented the surfaces PDMS-0.7(0)/SiO_2(15), PDMS-0.7(10)/SiO_2(15), PDMS-0.7(20)/SiO_2(15), and PDMS-0.7(40)/SiO_2(15) before and (e,f,g,h) after extraction of the porogen.

PDMS in the resin exhibited a smooth surface morphology without any distinguishable features on the micrometer scale (Figure 4.3a). With each increase in the PDMS-0.7 concentration, the surface morphology transitioned to a rougher morphology with nodules exposed at the interface on the micrometer scale. The sample containing 40% PDMS-0.7 displayed the most complex surface, as shown in Figure 4.3d.

Figures 4.3e-h show the SEM images of surfaces fabricated with 0 wt.%, 10 wt.%, 20 wt.%, and 40 wt% PDMS-0.7, respectively, after extraction of the porogen with hexane. Upon removal of the porogen, the space previously occupied by PDMS results in the creation of the porous structure. As shown in Figure 4.3e, extraction of the coating without PDMS resulted in no change in morphology as expected. The SEM image of the sample prepared with 10 wt.% PDMS (Figure 4.3f) showed the surface was flat and partially covered with nanometer features after extraction. An additional increase in PDMS content to 20 wt.% provided a surface (Figure 4.3g) predominately covered with a nanoscale porosity and roughness owing to the combination of pore generation and nanoparticle aggregation. At 40% PDMS (Figure 4.3h), the extracted surface exhibited deep micrometer sized pores with nanometer surface features dispersed both on the surface and inside the pores. The cross-sectional morphology of the PDMS-0.7(40)/SiO_2(15) TMTVSi/GDMP sample was also investigated by SEM, as presented in Figure 4.4. From Figure 4.4a, it can be clearly seen that the porogen resulted in the formation of an interconnected porous structure throughout the thickness of the polymer resin. The enlarged images showed that the nanoparticles preferentially aggregated on the surface and formed hairy branch like feature (Figure 4.4c) resulting in a nanoscale roughness. From these results, it can be concluded that the PDMS porogen loading level

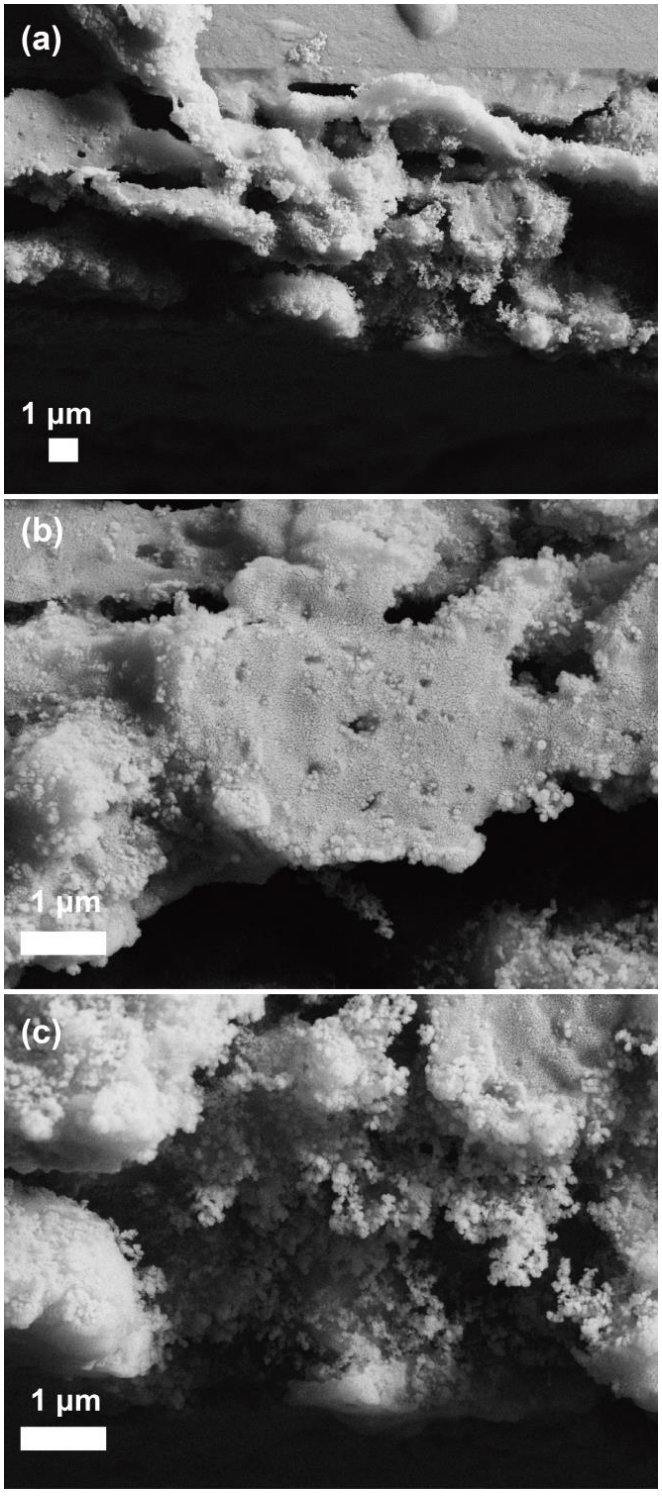

Figure 4.4 SEM images of sample PDMS-0.7(40)/SiO_2(15).

(a) cross-section, (b) zoomed in area of bulk resin with sparsely distributed NPs (c) zoomed in area of interface with nano hairy branched features.

has a strong impact on the development of the morphology after extraction. At low concentration, we postulate that the main effect of PDMS is to interact with TMS-modified nanoparticles and the favorable interaction drives the NPs to migrate from the bulk to the interface enabling the formation of nanoscale roughness after PDMS extraction. The partial coverage of nanoscale features on the surface is due to the insufficient PDMS content. As porogen concentration is increased, PDMS covers the entire surface and yields a nanoparticle covered surface after extraction. Further increasing porogen content, the excess PDMS undergoes phase separation from the thiol-ene polymer resin creating micrometer and submicrometer scale porous structures with nanoparticles superimposed on the surface.

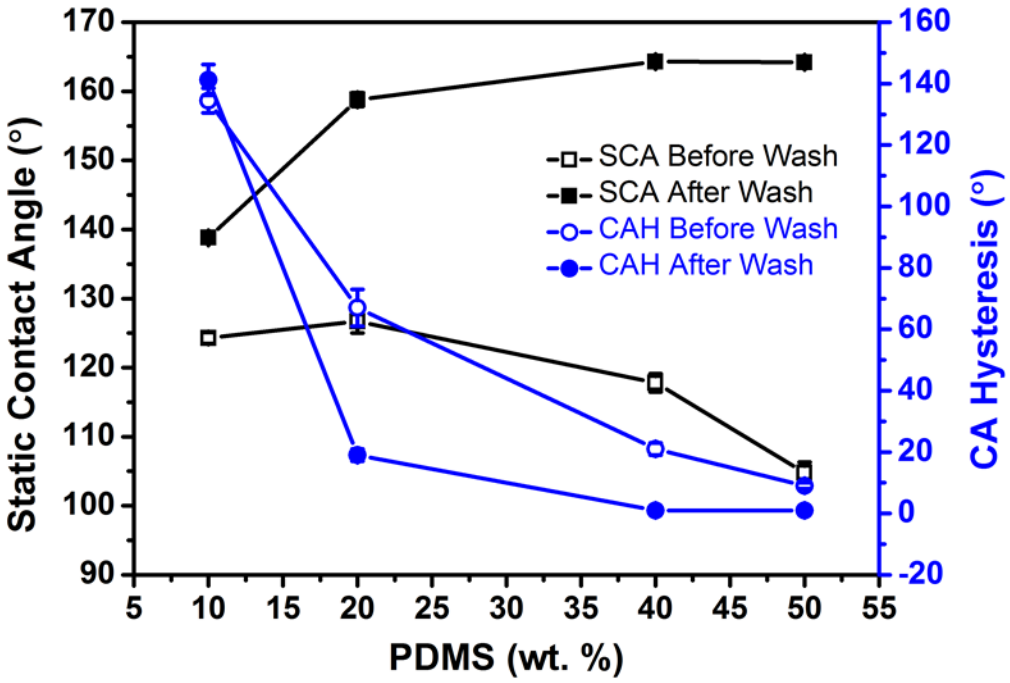

Figure 4.5 Variation of static contact angle (SCA) and contact angle hysteresis (CAH) as a function of PDMS concentration.

To study the effect of porogen concentration on the wetting behavior, the static contact angle (SCA) and contact angle hysteresis (CAH) were measured with DI water. Figure 4.5 shows the static and dynamic contact angle measurements of surfaces as a function of PDMS concentration before and after extraction with hexane. Before extraction, the SCA of the films steadily decreased from 124.3±0.8° to 104.8±1.5° with increasing the PDMS content from 10 wt% to 50 wt% as shown by black line with open squares. The CAH exhibited a similar trend decreasing from 134.5±4° to 9±1° with increasing PDMS content, as shown by the blue line with open circles. The reduction of both WCA and CAH can be attributed to the smoother surface generated with higher PDMS loadings – a result support by the previously discussed SEM study (Figure 4.3). At 10 wt% PDMS concentration, the surface was partially covered by PDMS and resulted in water droplet pinning and a high CAH value. The presence of higher content of PDMS, which is immiscible with water, at the solid-liquid interface provides the coating with a similar wetting behavior as previously reported for lubricant infused porous surfaces (LIPS).[29] With increasing the PDMS amount, the solid surface was dominated by the presence of a smooth and stable PDMS lubricant layer at the interface which nearly eliminated the pinning of the droplets and greatly reduced the CAH. The contact angle results for the films after PDMS extraction process are shown as closed symbols in Figure 4.5. Samples prepared with 10 wt.% PDMS showed an increased SCA (relative to the sample prior to extraction) at 138.8±0.8° and high CAH of 141.2±5° after extraction of the porogen. The increased hydrophobicity is due to the nanometer-sized roughness that partially covered the surface owing to segregation of the nanoparticles to the PDMS/polymer interface. With 20 wt% PDMS, the uniformly distributed nanometer

roughness endows the surface with a WCA of 158.8±1°, but the absence of microscale features renders the surface with relatively high CAH (19±2°). Superhydrophobicity was achieved with the 40 wt.% PDMS loading level (SCA=164.3±0.4°, CAH= 1±0.5°), which reflects the dual scale hierarchical features previously confirmed by SEM. The contact angle study demonstrated the advantage of combining the porogen leaching technique with spray deposition for the preparation of superhydrophobic coatings in terms of building sufficient surface roughness while significantly reducing the nanoparticle concentration from 30 wt% in our previously reported work[27-28] to 15 wt% in the current work.

Having investigated the mechanism of dual scale roughness formation, the influence of PDMS molecular weight on pores dimension, distribution, and surface wetting properties were studied. Previous work in porous materials has demonstrated that the average molecular weight of polymeric porogens play an important role in the generation of the porous structure.[30-32] PDMS is available in a wide range of well-defined molecular weights. PDMS with very low molecular weight (~300 g/mol) are volatile, and PDMS with high molecular weight (>140,000 g/mol) exhibits high viscosity which will affect its compatibility with the thiol-ene resin. With these considerations, PDMS porogens with weight average molecular weights of 0.7, 14 and 140 kg mol^{-1} were selected for the following investigation and were labeled as PDMS-0.7, PDMS-14, and PDMS-140, respectively.

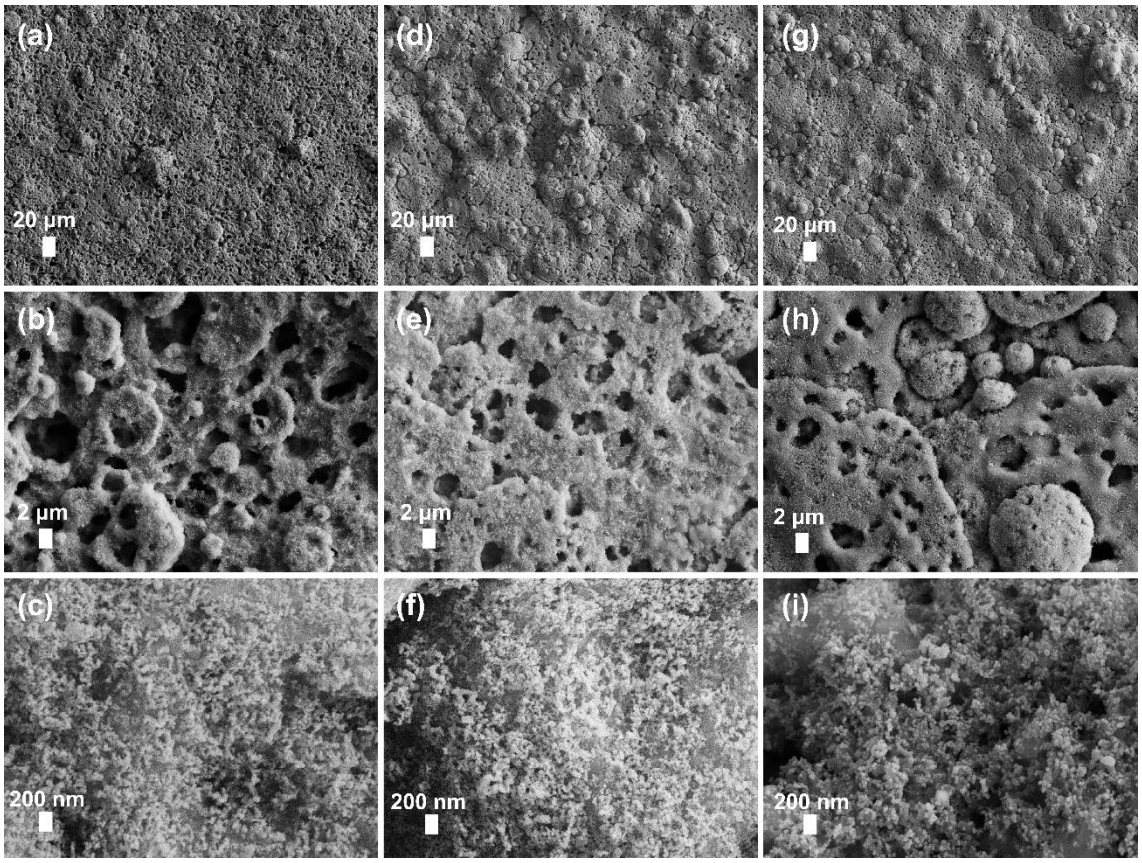

Figure 4.6 SEM images of samples after PDMS extraction at low and high magnifications.

(a-c) PDMS-0.7/SiO_2(15), (d-f) PDMS PDMS-14/SiO_2(15), and (g-1) PDMS-140/SiO_2(15)

As shown by the SEM images obtained at 200x magnification (Figure 4.6a, 4.6d, and 4.6g), the samples prepared with various molecular weight PDMS exhibit similar morphologies arising from the spray deposition process, with spherical aggregations that range from 10 to 20 µm. The effect of PDMS molecular weight on surface morphology and porous structure are more clearly observed at 2000x (Figure 4.6b, 4.6e, and 4.6h). As shown, the molecular weight of the PDMS minimally influences the surface morphology after extraction. Within the scope of SEM images, a large difference in the number of pores was not observed. Likewise, the SEM images obtained at 20000x magnification (Figure 4.6c, 4.6f, and 4.6i) showed that coatings prepared with different

molecular weight PDMS as porogens, the surfaces exhibited similar nanoscale morphology and roughness after extraction, which can be mainly attributed to the surface segregation of silica NPs to the surface. The dual scale roughness provides surfaces with high contact angle for all three samples with PDMS-0.7, PDMS-14, and PDMS-140 resulting in SCAs of 163.4±0.3°, 162.4±0.6°, and 162.1±0.3°, respectively, as shown in Figure 4.7. The minor differences in microscale morphological features observed in the SEM arising from the various PDMS porogens primarily influence the contact angle hysteresis with PDMS-0.7, PDMS-14, and PDMS-140 resulting in CAHs of 1±0.5°, 3±1°, and 7±1°, respectively.

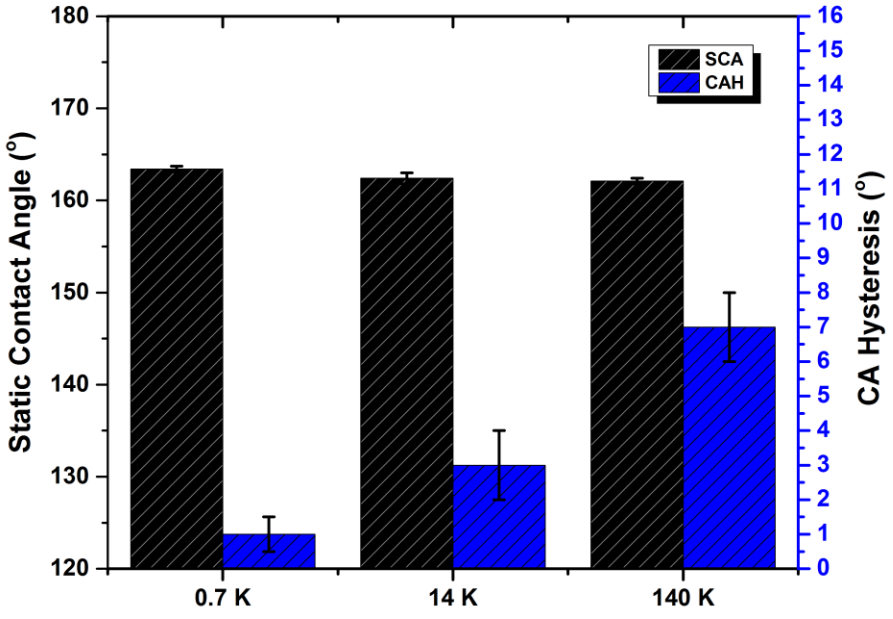

Figure 4.7 Variation of static contact angle and contact angle hysteresis as a function of Mw change.

4.3.4 Reversible Wetting by Porogen Extraction and Replenishment Process.

While the porogen leaching process typically involves a complex and time-consuming extraction process, the method presented herein using hexane to extract PDMS from the surface is an exceedingly fast and straightforward process. Upon washing the surface with hexane using a simple rinse bottle, the surface color changes from semitransparent to opaque white within a few seconds with a corresponding change in wettability from slippery hydrophobicity to superhydrophobicity. Interestingly, the wetting properties of the porous surfaces are reversible from superhydrophobic to slippery hydrophobic simply by spraying the surface with a PDMS solution (50 wt.% in hexane). The porous structure formed during the film fabrication and extraction process is capable of being refilled by capillary action upon exposure to a PDMS solutions, where the porous structure again locks in the liquid lubricant. To investigate the reversibility of the wetting process, we conducted the repeated cycles of extraction and PDMS replenishment by washing with hexane followed by spraying the coating with a PDMS solution. Figure 4.8 shows the wetting behavior for up to 10 extraction and replenish cycles. As shown, the contact angle of the surface increased to 163.5°±0.8° after each hexane extraction and decreased to 111.4°±2.6° when replenished with PDMS. These result indicate the surface has very good reversibility between the wetting states of slippery hydrophobic and superhydrophobic.

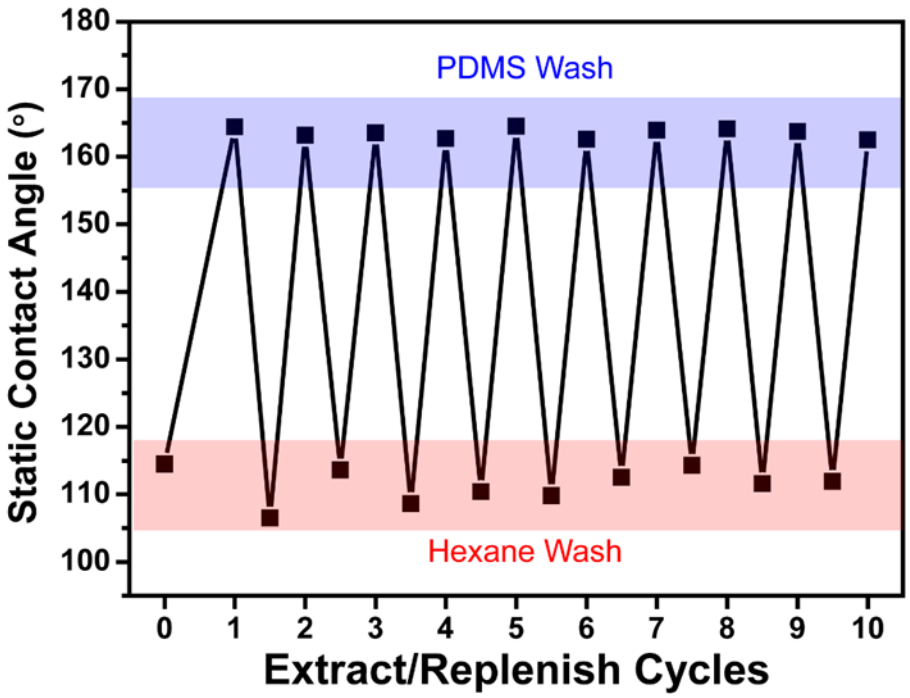

Figure 4.8 Reversibility of water contact angles on the as-prepared coating.

4.4 Conclusions

In summary, we have demonstrated a facile strategy to fabricate superhydrophobic coatings exhibiting multiscale roughness with 50% less nanoparticle loading using a spray deposition and porogen leaching approach. The selection of PDMS as porogen and silicone-containing resin enables surface segregation of the nanoparticles at the porogen/polymer interface providing the surface with nanometer roughness upon removal of the porogen. The porogen concentration was found to have a significant impact on the formation of the porous structure at the micrometer and submicrometer scales. The porogen molecular weight was found to minimally influence the pore size or overall surface morphology. The wettability of the surface was demonstrated to be reversible between a lubricant-infused slippery hydrophobic and porous superhydrophobic surface. The switchable wettability by extracting and replenishing of

the porogen may invoke interest in the application of self-cleaning coatings, architecture preservation materials, and fluid transportation devices.

4.5 References

1. Barthlott, W.; Neinhuis, C., Purity of the Sacred Lotus, or Escape from Contamination in Biological Surfaces. *Planta* **1997,** *202*, 1-8.
2. F., L.; Y., Z.; J., X.; Y., Z.; N., W.; F., X.; L., J., Petal Effect: A Superhydrophobic State with High Adhesive Force. *Langmuir* **2008,** *24*, 6.
3. Zhao, W.; Wang, L.; Xue, Q., Fabrication of Low and High Adhesion Hydrophobic Au Surfaces with Micro/Nano-Biomimetic Structures. *The Journal of Physical Chemistry C* **2010,** *114*, 11509-11514.
4. Kondrashov, V.; Ruhe, J., Microcones and Nanograss: Toward Mechanically Robust Superhydrophobic Surfaces. *Langmuir* **2014,** *30*, 4342-50.
5. Peng, S.; Yang, X.; Tian, D.; Deng, W., Chemically Stable and Mechanically Durable Superamphiphobic Aluminum Surface with a Micro/Nanoscale Binary Structure. *ACS Appl Mater Interfaces* **2014,** *6*, 15188-97.
6. Jiang, L.; Zhao, Y.; Zhai, J., A Lotus-Leaf-Like Superhydrophobic Surface: A Porous Microsphere/Nanofiber Composite Film Prepared by Electrohydrodynamics. *Angew Chem Int Ed Engl* **2004,** *43*, 4338-41.
7. Pan, S.; Kota, A. K.; Mabry, J. M.; Tuteja, A., Superomniphobic Surfaces for Effective Chemical Shielding. *J Am Chem Soc* **2013,** *135*, 578-81.
8. Liu, Y.; Chen, X.; Xin, J. H., Super-Hydrophobic Surfaces from a Simple Coating Method: A Bionic Nanoengineering Approach. *Nanotechnology* **2006,** *17*, 3259-3263.
9. Lakshmi, R. V.; Bharathidasan, T.; Basu, B. J., Superhydrophobic Sol–Gel Nanocomposite Coatings with Enhanced Hardness. *Applied Surface Science* **2011,** *257*, 10421-10426.
10. Lau., K. K. S.; José, B.; Teo., K. B. K.; Chhowalla, Superhydrophobic Carbon Nanotube Forests. *Nano Letters* **2003,** *3*, 5.
11. Deng, X.; Mammen, L.; Zhao, Y.; Lellig, P.; Mullen, K.; Li, C.; Butt, H. J.; Vollmer, D., Transparent, Thermally Stable and Mechanically Robust Superhydrophobic Surfaces Made from Porous Silica Capsules. *Adv Mater* **2011,** *23*, 2962-5.
12. Hsu, C. P.; Chang, L. Y.; Chiu, C. W.; Lee, P. T.; Lin, J. J., Facile Fabrication of Robust Superhydrophobic Epoxy Film with Polyamine Dispersed Carbon Nanotubes. *ACS Appl Mater Interfaces* **2013,** *5*, 538-45.
13. Ge, D.; Yang, L.; Zhang, Y.; Rahmawan, Y.; Yang, S., Transparent and Superamphiphobic Surfaces from One-Step Spray Coating of Stringed Silica Nanoparticle/Sol Solutions. *Particle & Particle Systems Characterization* **2014,** *31*, 763-770.
14. Gampos, R.; Guenthner, A. J.; Meuler, A. J.; Tuteja, A.; Cohen, R. E.; McKinley, G. H.; Haddad, T. S.; Mabry, J. M., Superoleophobic Surfaces through Control of Sprayed-on Stochastic Topography. *Langmuir* **2012,** *28*, 9834-41.
15. Xu, Q. F.; Liu, Y.; Lin, F. J.; Mondal, B.; Lyons, A. M., Superhydrophobic Tio2-Polymer Nanocomposite Surface with Uv-Induced Reversible Wettability and Self-Cleaning Properties. *ACS Appl Mater Interfaces* **2013,** *5*, 8915-24.
16. Ganesh, V. A.; Dinachali, S. S.; Nair, A. S.; Ramakrishna, S., Robust Superamphiphobic Film from Electrospun Tio2 Nanostructures. *ACS Appl Mater Interfaces* **2013,** *5*, 1527-32.
17. Jung, Y. C.; Bhushan, B., Mechanically Durable Carbon Nanotube−Composite Hierarchical Structures with Superhydrophobicity, Self-Cleaning, and Low-Drag. *ACS Nano* **2009,** *3*, 4155-4163.
18. Liu, X.; Smith, L. A.; Hu, J.; Ma, P. X., Biomimetic Nanofibrous Gelatin/Apatite Composite Scaffolds for Bone Tissue Engineering. *Biomaterials* **2009,** *30*, 2252-8.

19. Liu, X.; Ma, P. X., Phase Separation, Pore Structure, and Properties of Nanofibrous Gelatin Scaffolds. *Biomaterials* **2009,** *30*, 4094-103.
20. Chung, H. J.; Park, T. G., Surface Engineered and Drug Releasing Pre-Fabricated Scaffolds for Tissue Engineering. *Adv Drug Deliv Rev* **2007,** *59*, 249-62.
21. Bencherif, S. A.; Braschler, T. M.; Renaud, P., Advances in the Design of Macroporous Polymer Scaffolds for Potential Applications in Dentistry. *J Periodontal Implant Sci* **2013,** *43*, 251-61.
22. Jackson, E. A.; Hillmyer, M. A., Nanoporous Membranes Derived from Block Copolymers: From Drug Delivery to Water Filtration. *ACS Nano* **2010,** *4*, 3548-3553.
23. Joo, W.; Park, M. S.; Kim, J. K., Block Copolymer Film with Sponge-Like Nanoporous Structure for Antireflection Coating. *Langmuir* **2006,** *22*, 7960-7963.
24. Wu, D.; Xu, F.; Sun, B.; Fu, R.; He, H.; Matyjaszewski, K., Design and Preparation of Porous Polymers. *Chem Rev* **2012,** *112*, 3959-4015.
25. Gokmen, M. T.; Du Prez, F. E., Porous Polymer Particles—a Comprehensive Guide to Synthesis, Characterization, Functionalization and Applications. *Progress in Polymer Science* **2012,** *37*, 365-405.
26. Liu, J.; Xiao, X.; Shi, Y.; Wan, C., Fabrication of a Superhydrophobic Surface from Porous Polymer Using Phase Separation. *Applied Surface Science* **2014,** *297*, 33-39.
27. Xiong, L.; Kendrick, L. L.; Heusser, H.; Webb, J. C.; Sparks, B. J.; Goetz, J. T.; Guo, W.; Stafford, C. M.; Blanton, M. D.; Nazarenko, S.; Patton, D. L., Spray-Deposition and Photopolymerization of Organic–Inorganic Thiol–Ene Resins for Fabrication of Superamphiphobic Surfaces. *ACS Applied Materials & Interfaces* **2014,** *6*, 10763-10774.
28. Sparks, B. J.; Hoff, E. F. T.; Xiong, L.; Goetz, J. T.; Patton, D. L., Superhydrophobic Hybrid Inorganic–Organic Thiol-Ene Surfaces Fabricated Via Spray-Deposition and Photopolymerization. *ACS Applied Materials & Interfaces* **2013,** *5*, 1811-1817.
29. Wong, T. S.; Kang, S. H.; Tang, S. K.; Smythe, E. J.; Hatton, B. D.; Grinthal, A.; Aizenberg, J., Bioinspired Self-Repairing Slippery Surfaces with Pressure-Stable Omniphobicity. *Nature* **2011,** *477*, 443-7.
30. Columbus, S.; Krishnan, L. K.; Kalliyana Krishnan, V., Relating Pore Size Variation of Poly (Varepsilon-Caprolactone) Scaffolds to Molecular Weight of Porogen and Evaluation of Scaffold Properties after Degradation. *J Biomed Mater Res B Appl Biomater* **2014,** *102*, 789-96.
31. Macintyre, F. S.; Sherrington, D. C., Control of Porous Morphology in Suspension Polymerized Poly(Divinylbenzene) Resins Using Oligomeric Porogens. *Macromolecules* **2004,** *37*, 8.
32. Wang, Q. C.; Švec, F.; Fréchet, J. M. J., Fine Control of the Porous Structure and Chromatographic Properties of Monodisperse Macroporous Poly(Styrene-Co-Divinylbenzene) Beads Prepared Using Polymer Porogens. *Journal of Polymer Science Part A: Polymer Chemistry* **1994,** *32*, 2577-2588.

CHAPTER V – CONCLUSION

Three different coating systems, with focus on expanding the wetting property range and improving the mechanical property of superhydrophobic coating, have been developed by spray deposition of organic-inorganic hybrid resins.

In the first study, through the use of low surface energy fluorine functioned PETMP, a superamphiphobic coating, extending the extreme anti-wetting property from water to low surface tension oil, had been fabricated. The effect of the fluorocarbon chain length on the oleophobicity was investigated. Formulation containing the longer fluorocarbon chain provided the better anti-wetting performance. The F_9PETMP(30)/SiO_2(30) coatings displayed a robust response in terms of maintaining superhydrophobicity following multiple mechanical abrasion cycles; however, the superoleophobic wetting properties degraded rather quickly following mechanical damage to the surface. The mechanical durability remains a challenge.

In the second study, a membrane with unique superoleophobicity and superhydrophilicity was fabricated. The synergistic contributions from the chemical composition and the textured surface provided coatings that display extreme repellency toward non-polar liquids (i.e. hexadecane, vegetable oil), but strong affinity to water. The performances of this superhydrophilic/superoleophobic coating on oil/water emulsion and dye contained emulsion separation were studied. The results showed that the fluorine compound provided the membrane with high oil and dye rejection ratios indicating its potential application in wastewater treatment.

In the final study, a novel method on the preparation of superhydrophobic surfaces with 50 wt.% less NPs content was presented. A porogenic material was

incorporated into the resin to form microphase separation during the UV polymerization. In the following solvent leaching process, the liquid porogen was dissolved and resulted in microscale porous features. The aggregations of NPs preferably presented at the porogen/resin interface and were exposed out after the leaching process thus providing the film with nanoscale roughness. The combined micro-and nano-roughness proved the film with superhydrophobicity exhibiting multiscale roughness.